ISRAPS
Bulletin

TSRP-2022
SPECIAL ISSUE

ISRAPS

Guest Editor
Atanu Barik

Message from the President and Secretary, ISRAPS

Dear ISRAPS members,

On behalf of ISRAPS executive council, we wish you all a very happy new year 2022 and take this opportunity to acknowledge the contribution of all the members who have actively participated in organizing various activities of ISRAPS.

Though in the prevailing pandemic situation we could not meet each other in person, we have tried our best to preserve the tradition of ISRAPS by arranging discussion meetings and symposia through virtual (online) mode. We have successfully organized ISRAPS discussion meeting on "Gas-Phase Kinetics & Dynamics" on April 10, 2021. On this occasion, we felicitated Prof. S. Wategaonkar, Ex-Vice President of ISRAPS for his active contribution towards the growth of ISRAPS. Another event was the National Symposium on Radiation and Photochemistry (NSRP-2021), which was held virtually from IIT Gandhinagar during June 25-26, 2021. The online symposium was a grand success in terms of the sharing of knowledge in the advanced areas of radiation and photochemistry. All the young researchers were quite excited to share their research work in flash presentation mode. The EC thanks all the participants, especially, Prof. S. Kanvah from IIT Gandhinagar, for contributing to the success of NSRP-2021.

One of the important events of ISRAPS, Trombay Symposium on Radiation & Photochemistry (TSRP-2022) is being organized virtually from Training School Hostel, Bhabha Atomic Research Centre, Mumbai during January 12-15, 2022. On this occasion, ISRAPS has brought out an ISRAPS bulletin (TSRP-2022 special issue). It is the collection of articles about the recent developments in the field of radiation and photochemistry from the eminent scientists invited in TSRP-2022. The executive council of ISRAPS takes this opportunity to thank all the contributors for making this special issue very informative.

Finally, we would like to thank Dr Atanu Barik, the Guest Editor of this special issue for his efforts to bring out a scientifically rich bulletin containing eleven articles of varied interests in the field of advanced techniques in radiation and photochemistry.

Once again, we wish to express our sincere gratitude to all the life members for their constant support and encouragement and look forward to your valuable suggestions and active participation in the forthcoming events of ISRAPS.

<div align="center">

Dr. Awadhesh Kumar
President

Dr. (Mrs.) J. Mohanty
Secretary

</div>

ISRAPS

INDIAN SOCIETY FOR RADIATION AND PHOTOCHEMICAL SCIENCES (ISRAPS)

EXECUTIVE COUNCIL (2021-2023)

President
Dr. Awadhesh Kumar

Vice-Presidents
Prof. C. T. Aravindakumar
Prof. A. S. Kumbhar

Secretary
Dr. (Mrs.) J. Mohanty

Jt. Secretary
Dr. P. Mathi

Treasurer
Dr. Atanu Barik

Executive Members

Dr. N. Choudhury	Dr. G. R. Dey	Prof. K. R. Genwa
Prof. S. K. Gundimeda	Dr. Virendra Kumar	Dr. M. Kumbhakar
Dr. M. C. Rath	Dr. (Mrs.) S. Sen Gupta	Dr. P. Sharma
Dr. V. S. Tripathi	Dr. P. D. Naik	Dr. A. C. Bhasikuttan

Co-opted Members

Prof. Santosh Chidangil	Prof. Anindya Datta	Dr. S. Dutta Choudhury
Prof. J. P. Mittal	Dr. D. B. Naik	Dr. C. N. Patra
Dr. R. Puspalata	Dr. S. K. Sarkar	Prof. K. K. Sharma
Prof. A. K. Singh	Dr. Avesh K. Tyagi	Prof. S. Wategaonkar

Web Master
Dr. Abhishek Das

Contact details:
C/o Radiation & Photochemistry Division
Bhabha Atomic Research Centre, Mumbai-400085
E-mail: israps.secretary@gmail.com
Telephone:(022)- 25593771/25592668/25590302

ISRAPS Bulletin

A Publication of
Indian Society for Radiation and Photochemical Sciences

Editor's Desk...

It is a great privilege to edit this TSRP-2022 Special issue of ISRAPS Bulletin on the auspicious occasion of the Trombay Symposium on Radiation & Photochemistry (TSRP-2022) organised by Radiation & Photochemistry Division, Bhabha Atomic Research Centre (BARC) and Indian Society for Radiation and Photochemical Sciences (ISRAPS) through virtual mode.

It is our rich tradition that on every occasion of TSRP we come out with a special issue, containing articles on various contemporary research areas in the field of radiation and photochemical sciences, by eminent scientists. The present issue encompasses articles in thrust areas such as spodium bonding with respect to protein structure and enzyme activity, use of carbon quantum dots for their luminescent properties as well their biosensing applications, reshaping of triangular shaped silver nanoparticle under laser radiation and their possible application for the development of random laser, and formation of molecular self-assembly from thiophene based compound in tetrahydrofuran-water mixture, as observed by fluorescence correlation spectroscopy and TEM.

In addition, there are articles on detection of environment polluting pigments by fluorescence method, use of radiation induced noble metal nano particle immobilised with enzymes for pollutant degradation, and design strategy of fluorophore for subcellular imaging. Next couple of articles, highlight the hydrogen bond dynamics in alcohol and alcohol based deep eutectic solvents by two-dimensional infrared spectroscopy, and molecular clusters in gas phase to understand catalytic, atmospheric and biological processes. The last article highlights the release of hydrogen from the water molecule entrapped in carbon nanotubes, using quantum mechanical studies.

On behalf of ISRAPS, I sincerely acknowledge the active cooperation from all the contributing authors of this issue. I personally thank ISRAPS for entrusting the editorial responsibility on me.

Dr. Atanu Barik obtained M. Sc. degree in Chemistry from Burdwan University (West Bengal) in 1999. After graduating from BARC Training School in 2000, he joined Radiation & Photochemistry Division, BARC. He has obtained Ph. D. degree in Chemistry from University of Mumbai in the year 2006. During the year 2007-2008 he was post-doctoral fellow at Laboratoire de Radiolyse, CEA Saclay, France. He was the recipient of DAE young scientist award and group achievement award in the year 2009 and 2017 respectively. Since the year 2019, he is also associated with Homi Bhabha National Institute, Mumbai as an Assistant Professor. His current research activities focus on free radical chemistry and excited state properties of molecules employing photochemical and radiation chemical techniques. So far, he has published more than 50 research articles in international journals. He has successfully guided one Ph.D. student and five M.Sc. project students.

Contents

Recent Advances in Spodium Bonding: Inorganic Crystals to Biological Systems

Akshay Kumar Sahu[1,2], **Shivam Mahapatra**[1,2], **and Himansu S. Biswal**[1,2]*

[1] *School of Chemical Sciences, National Institute of Science Education and Research (NISER), PO-Bhimpur-Padanpur, Via-Jatni, District- Khurda, PIN - 752050, Bhubaneswar, India*
[2] *Homi Bhabha National Institute, Training School Complex, Anushakti Nagar, Mumbai 400094, India*

Abstract

The name spodium bonds (Sp-bonds) was coined in 2020 for referring to the net attractive interaction between the complexes formed by Group 12 elements with oxidation state +2 and any electron-rich species. Although the reports about spodium bonds are limited in number, the significance of such noncovalent interactions cannot be ignored. Sp-bonds have been shown to participate in the structural flexibility of systems as well as their functionality. Considering the biological implications of zinc ions, we explored the presence and effect of Sp-bonds in Zn-proteins. Using a detailed PDB analysis and systematic ab initio calculations, we showed that spodium bonds in tetrahedral Zn sites are abundant and might also serve as a determining factor in protein structure and enzyme inhibition.

1. Introduction

Since the day hydrogen bonding was first discovered, noncovalent interactions (NCIs) have attracted the attention of researchers across the globe. With more extensive research being done, new interesting facts about the NCIs are coming up to the surface, from their presence in biomolecules and inorganic crystals to their applications in catalysis, molecular recognition, molecular stabilization, and many more.[1-3] The last decade has observed a significant growth in this field and has led to the discovery of various new NCIs such as halogen bond,[4] chalcogen bond,[5] pnictogen bond,[6] tetrel bond,[7] and triel bond,[8] etc. most of which occur due to the sigma (σ) hole. The anisotropy of the charge distribution over the atom leads to the formation of the positive electrostatic potential region, known as σ-hole, along with the covalent bond to the atom.[9] This positive region or sigma-hole interacts with any electron-rich atom to form the σ-hole complex, and the interaction is known as σ-hole interaction. The specific name of this interaction depends on the σ-hole forming atom. When the Group-12 elements are involved in such noncovalent interactions, these are termed as spodium bonds

(Sp-bonds) by Frontera and co-workers.[10] One of the first experimental reports discussing spodium bonds in a dichloro-bis(thiosemicarbazide)-mercury(II) complex was published recently. This work showed that the electron donor was located opposite to the polarized Hg-Cl bond at a distance greater than the sum of covalent radii and smaller than the sum of van der Waals radii of the two species. It also established high directional spodium bonds.[11] Following these reports, an organized search for spodium bonds in the CSD Database was performed by Frontera and co-workers. Based on experimental evidence obtained from the CSD analysis and results from ab initio calculations followed by QTAIM/NCI Plot/NBO analyses, the group established the presence of such noncovalent interactions in inorganic crystals, which can play a crucial role in the crystal packing of tetrahedral complexes of Group 12 elements with oxidation state +2.[12]

In our work, we focused on tetrahedral sites of Zn^{2+} ions in biological systems since Zn is the second most abundant transition metal present inside the human body. Zn^{2+} ion is an essential cofactor in the case of several

metabolic enzymes and regulatory proteins.[13-15] The metal ion has shown catalytic activity in the deprotonation of Zn-coordinated water in human carbonic anhydrase II (HCA2)[16] or in the stabilization of negatively charged species, such as in carboxypeptidase A.[17] In Zn-finger proteins, Zn^{2+} ions have even played a fundamental role in the protein structure and folding.[18] Moreover, it was observed that the alcohol dehydrogenase (ADH) completely loses its catalytic activity upon removing zinc ions from its active site.[19,20] We started our work by looking for the presence of σ-holes in biological systems by performing molecular electrostatic potential (MEP) surface analysis, shown in Figure 1. In order to emphasize the significance of this interaction and its pivotal role in biological systems, we selected two examples, one involving metallo-β-lactamases (MBLs) and the other encompassing the structure and activation mechanism of metallopeptidases (MPs).[21]

2. Methods

The analysis was done in two parts:

2.1. PDB analysis: The criteria used to download the PDB[22] files from the RCSB website (October 2020 release) was that a PDB file must contain a Zn atom with a resolution better than 2 Å. We found 6911 PDB files which were further used for the analysis of the Sp-bonds. The home-written python script was used for the batch processing of PDB files. The following structural parameters were used for the analysis:

To maintain the tetrahedral geometry, four Y atoms bonded with Zn were searched with distance $d_{Zn-Y} < 2.5$ Å, where Y was any combination with N, O, and S.

The distance between Zn and A was 2.5 Å $\leqslant d_{Zn---A} < 5$ Å, where A was an electron-rich atom, which in our case was O, N, and S. To avoid the possibility of the coordinate bond, the distance between Zn and A was taken greater than 2.5 Å which is greater than the sum of their covalent radii. The covalent radii of Zn, O, N, and S are 1.22, 0.66, 0.71, and 1.05 Å, respectively.[23]

The angle θ (∠Y-Zn---A) was restricted with the condition, $140° \leqslant θ \leqslant 180°$ to take only highly directional cases into consideration.

The stride software[24] was used to determine the secondary structure of the protein structures.

2.2. Theoretical study: To generate the model system for further study, we selected only those PDB files where the angle θ (∠Y-Zn---A) was in between 160° and 180°. The selection was further limited to the cases with the shortest Zn and A distance, where A was either O or S. Once the PDB files were chosen, we modeled the interaction sites manually by taking the Zn and its coordinating residues and interacting partner (amino acid, ligand, water) and replaced the HIS, ASP/GLU, and CYS residues with
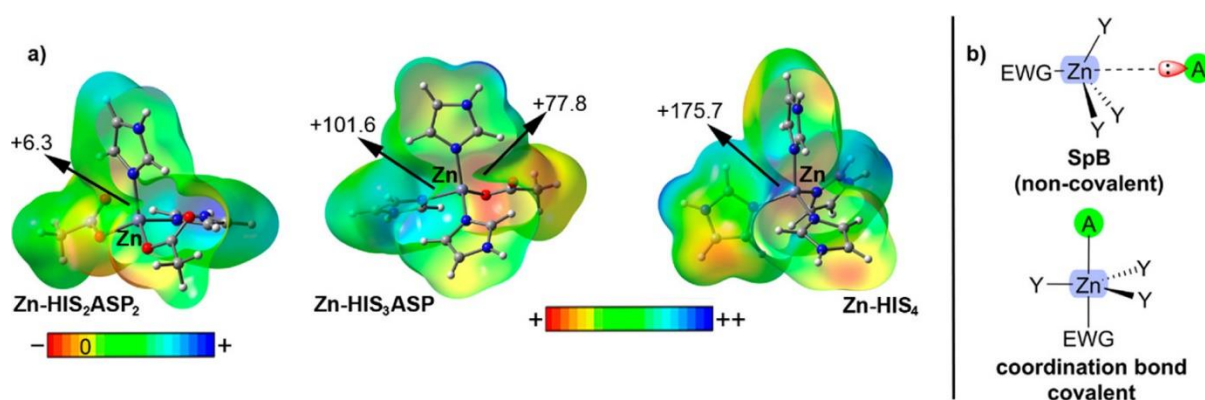

Figure 1: (a) The MEP surfaces of three different Td Zn complexes with different net charges (0, +1, and +2, respectively). (b) Schematic comparison between an Sp-bond and coordinate bond.

Table 1: Classification of contacts between Zn and electron-rich partners (O/N/S).

Donor	Amino acids		Ligands	Water	Total
	Backbone	Side chain			
N	13,779	7210	847		21,836
O	4870	10,994	3374	10,442	29,680
S		624	618		1242

imidazole ring, acetate group, and thiomethyl groups respectively. All the models were created using Accelrys Discovery Studio Visualizer[25] and Gaussian-16.[26]

Only the hydrogen positions of all models were optimized using the BP86[27]-D3[28]/def2-SVP[29] level of theory. The interaction energy of these Sp-bonds ($\Delta E_{complex} = E_{complex} - E_{Zn-center} - E_{electron-rich\ partner}$) was calculated using all these optimized hydrogen models with the RI-MP2[30]/def2-TZVP[29] level of theory using the TURBOMOLE 7.0 program.[31] The energy of the complex, Zn-center, and electron-rich partner were calculated separately using the same level of theory. The Boys-Bernardi counterpoise technique was used to overcome the basis set superposition error (BSSE) in the interaction energy.[32] The wavefunction and MEP of the complexes were calculated using the Gaussian-16 package with B3LYP[27]-D3/def2-TZVP level of theory. Bader's QTAIM method was used for the topological analysis of electron density at followed by NCI plot analysis.[33]

3. Results and discussion

3.1. PDB Survey: From the PDB analysis, we found a total of 52758 distinguished contacts Zn---A of Td Zn with the electron-rich atoms (N, O, and S). From Figure 2 (a), it was observed that approximately 50% of Zn---A contacts could be attributed to GLU, ASP, HIS, and CYS residues, followed by ~25% from other amino acids, ~20% from water molecules, and ~10% from the ligands. So, we can say that the Sp-bonds are widely present in the Zn-dependent proteins, where the interactions were extended between

various electron-rich partners starting from amino acids to water and ligands. A detailed analysis was done in Table 1, wherein in the case of N, most of the interactions were from the backbone N of proteins, which are likely to form very weak Sp-bonds as the electron pair of backbone N is delocalized over the peptide plane. However, in the case of O, most interactions come from the side chain of the proteins. Since S is not present in the backbone of proteins, all the interactions come from either the side chain of proteins or the ligands.

The Zn---O interactions predominate for the ligands over the Zn---N, and Zn---S interactions. The presence of many Zn---O interactions originating from water underlines the significance of buried water in the Zn-active site of proteins. As represented in Figure 2 (b), the statistical analysis, which is a radial distribution plot, shows that most of the Zn---A interactions lie in between 0.4 to 0.8, beyond the sum of their respective van der Waals radius. This strongly supports Alvarez's van der Waals radius, 2.39 Å,[34] 1 Å more than that of Bondi's van der Waals radius, 1.39 Å.[35] This plot also shows the directional nature of the Sp-bonds as most of the interactions are present in between 140º and 170º, as reported in previous CSD analysis.[12] The Ramachandran plot shows that Sp-bonds are formed by the different classes of secondary structures of protein residues, in which right-handed α-helix, β-strand, and collagen triple helix are present predominantly, as shown in Figure 2(c). Here, the highly populated clusters of data points are located near the top-left and middle-left regions. From the plot, we can say that the

left-handed α-helix structure is less abundant than other secondary structures since the middle-right cluster is less populated.

3.2. Energetics calculation

To investigate the directionality and strength of the Sp-bonds, we performed the ab initio analysis, where we were interested in only those structures that show the highly directional Sp-bonds (160º ⩽ ∠Y-Zn---A ⩽ 180º) because in such cases, the interaction between Td Zn and electron-rich partner appears to be stronger than in other cases. Also, to avoid the dominance of electrostatic interactions in Sp-bonds, only those structures were selected where the electron-rich partners were neutral species. Using the criteria mentioned above, we shortlisted a set of 13 PDB structures for the calculations, as shown in Table 2.

Each of the 13 PDB structures shows a

Table 2: List of PDB IDs, ResID, electron-rich atom, and respective binding energies

| PDB ID	ResID	ΔE	ΔE_{BSSE}	d_{Zn---A}	$\angle Y-Zn---A$
2ZNR	LYS404	−11.6	−9.8	4.462	173.7
3F1A	HIS172	−12.8	−11.4	4.206	172.9
5LE1	6UW503	−16.2	−13.3	3.806	177.3
3LQ0	TYR149	−11.1	−8.5	3.011	175.9
5UUD	HOH520	−26.7	−24.1	3.193	177.2
5A0X	HOH2120	−17.6	−15.5	4.037	178
6SJ4	LFK501	−10.8	−6.4	3.628	172.3
4P4F	GLU425	−18.6	−14.5	3.506	173.2
1UXM	LYS136	−21.5	−19.0	3.777	179.2
1F18	LYS136	−11.4	−9.7	4.08	178
2VR7	LYS136	−15.6	−13.7	4.036	175.5
6R6F	HOH651	−9.5	−6.7	4.246	162.6
2O6E	MET117	−13.0	−10.6	3.128	175.2
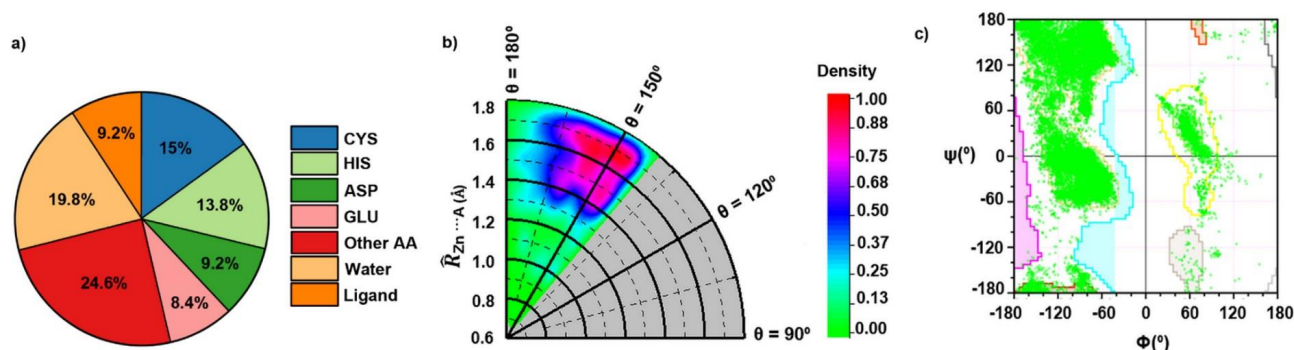
Figure 2: (a) Pie chart distribution of electron-rich residues involved in Sp-bonds. (b) Radial distribution of Sp-bonds in proteins. The plot is between the angle and the normalized distance (R_{Zn---A}), which is calculated by dividing the sum of van der Waals radii of both Zn and A atoms. (c) The Ramachandran plot of combined O/N/S atoms present in the amino acid residue.

unique Zn environment, although the ASP, GLU, and HIS residues, water molecules, and other non-protein ligands are the most common coordinating ligand of the Zn in each case, and the electron-rich partners are MET, TYR, or water molecules, etc. Except for the 4P4F, where the global charge on the Td Zn complex is 0, in all other cases, the charge is +1. From these calculations, we found that in all cases interaction energy of Sp-bonds are attractive in nature, starting from moderate (-8.5 kcal·mol^{-1}) to strong (-24.1 kcal·mol^{-1}). We also observed that Sp-bonds are similar to other noncovalent interactions like H-bonds, or CH−π interactions, etc., formed between Zn-coordinated ligands and electron-rich partners. For example, in the case of 5UUD, where a water molecule is an electron-rich partner, it shows a strong binding energy value. However, the total binding energy has additional contributions from the formation of two strong hydrogen bonds with Zn-coordinated water and the acetate ligand. Furthermore, an H-bond is formed between the O atom of the carbonyl of LYS136 and the CH group of Zn-coordinated HIS in the case of 1F18. These supporting interactions are supposed to act as the molecular anchor for Zn-center and electron-rich partners, which bring both partners to close together before forming the Sp-bonds.

3.3. AIM and NCIplot Analysis

The AIM and NCI plot analysis were done for five structures, including O and S atoms as electron-donating atoms, to gain further information about the Sp-bonds shown in Figure 3. First, 1UXM did not show any bond critical point (BCP) linking Zn and O atoms in AIM analysis. Instead, two BCPs link the carbonyl oxygen of LYS136 to (i) a CH group of a Zn-coordinated imidazole ring and (ii) another Zn-coordinated imidazole ring. However, the presence of the green color isosurface in between the space of Zn and O atoms from NCI plot analysis shows the existence of Sp-bonds.

In the case of 2OGE, where the electron-donating atom is S, AIM analysis shows a BCP which links the S atom to the Zn center. This shows the presence of the Sp-bond. In addition, two more BCPs are also present linking the S atom to CH groups of two different Zn-coordinated imidazole rings. The presence of isosurface between S atom and Zn-center from NCIplot analysis further confirms the presence of Sp-bond. The presence of extra BCPs indicates that secondary interactions are usually observed along with Sp-bonds.

In 3lQ0, where the donor atom is the O atom of TYR149, the AIM analysis shows the two BCPs between TYR19 and Zn-center. The first BCP links phenol O of TYR149 to Zn-center, which indicates the presence of Sp-bond. This was further confirmed by NCIplot analysis, where the isosurface is present between Zn-center and phenol O. The second BCP links the π-system of HIS92 to the CH group of the phenol ring. These extra BCPs confirm the presence of secondary noncovalent interactions as in this case it is CH-π and in the case of 1UXM and 2OGE, it is hydrogen bonds. In the case of 6R6F, where the electron-rich partner is a water molecule, we did not find any BCP from AIM analysis connecting O to the Zn-center. Instead, two BCPs connecting the two H atoms of water to vicinal Zn-coordinated two different imidazole rings were observed. This shows the presence of H-bonds. However, the presence of two greenish isosurfaces between the O and Zn-center in the NCIplot analysis denotes the existence of a weak Sp-bond.

Finally, in the case of 5LE1, where the electron-donating atom is O of a carbonyl group belonging to the ligand, no BCP linking the O atom to the Zn-center was found. However, the green isosurface from NCIplot analysis indicates the presence of Sp-bonds. The supporting noncovalent interactions were confirmed by the presence of two BCPs (i) O atom linked to the π-system of HIS179, which shows the presence of lone pair−π (Lp−π) interaction and (ii) CH group of ligand linked to π-system of HIS116, which
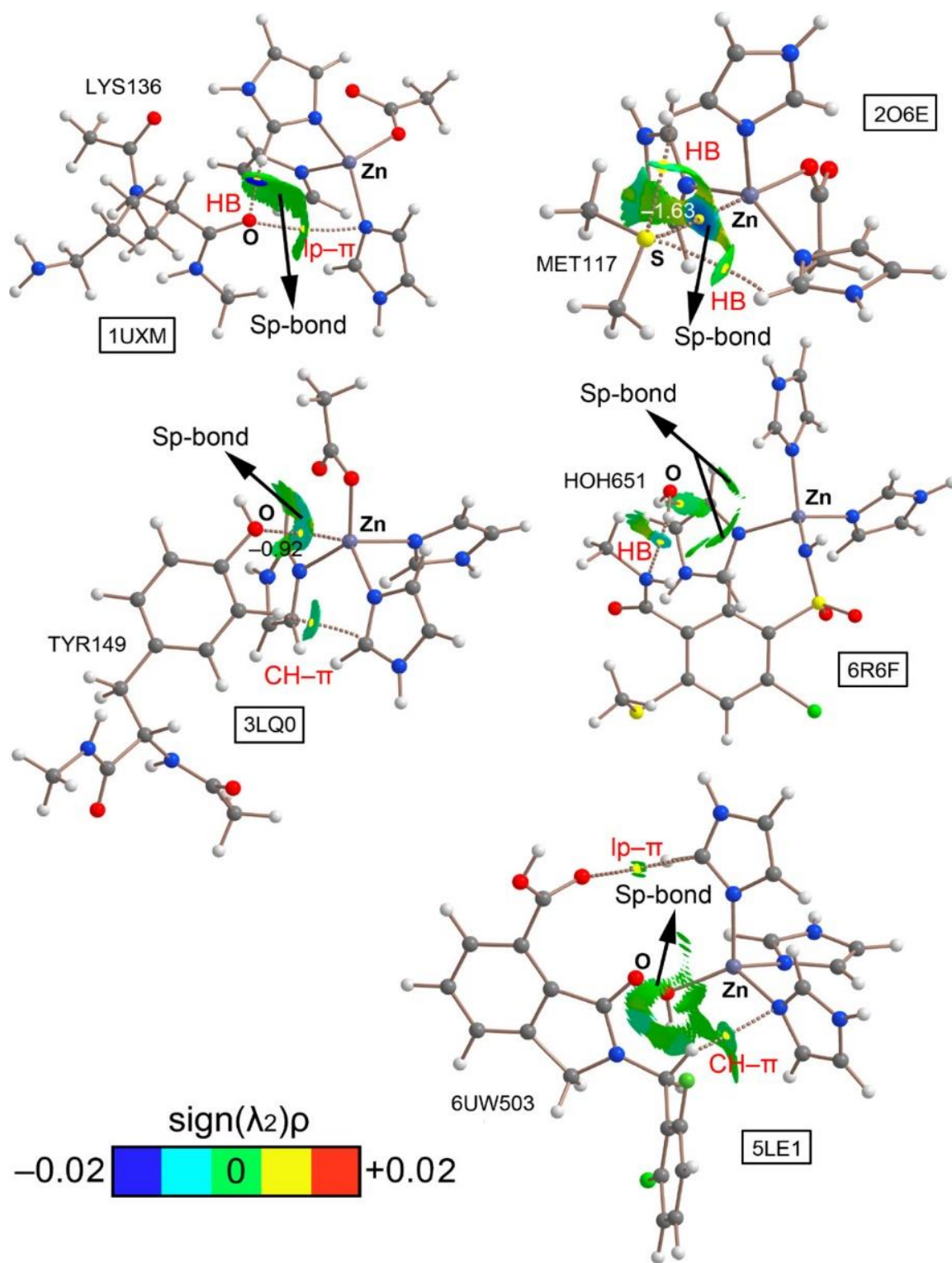
Figure 3: Distribution of molecular graphs of (a) 1UXM, (b) 2O6E, (c) 3LQ0, (d) 6R6F, and (e) 5LE1. The supporting interactions are highlighted in red. The $\rho.10^2$ values for 2O6E and 3LQ0 are also reported along with the NCI plot color range.

denotes the presence of CH−π interaction. The $\rho.10^2$ values at the critical points represent the Sp-bonds both for the 2O6E and 3LQ0, as shown in Figure 3. The electron density value of 2O6E is greater than the value of 3LQ0, which shows that the former has a stronger Sp-bond than the latter. This agrees with the result that we got from the energetic study and their corresponding NCI plot surface color, thus giving credibility to the utilization of the NCI plot index as a method to visualize and characterize interactions.

3.4. Implications of Sp-bonds in biological systems

We have shown the presence of spodium bonds in 5 proteins (Figure 3). Among all these cases, we selected two protein structures, 5LE1 and 3LQ0, to understand the biological implications of this interaction, shown in Figure 4. The PDB file, 5LE1, involves metallo-β-lactamases (MBLs). This family of enzymes is regarded as a potential therapeutic target owing to their bacterial resistance through hydrolysis.[36] Recently, the Verona Integron-encoded (VIM-2) protein was used in the development of a novel family of MBL inhibitors.[37] The VIM-2 protein makes use of diZn(II), with both the ions playing an important role in catalysis, concerning the binding of the β-lactam substrate and the hydrolytic activation of water.[38] Through the ^{1}H CPMG (Carr-Purcell-Meiboom-Gill) NMR analyses, it was revealed that the compound demonstrated the highest efficiency in VIM-2 inhibition (IC_{50} value = 10.6 µM) showed noncovalent binding with the Zn center. Upon further analysis, it was found that there was a region of positive electrostatic potential along with the Zn-N_{HIS114} bond (+71.5 kcal·mol^{-1}), which facilitates spodium bond formation between the O atom from the amide functional group of the inhibitor and one of the zinc atoms. The strength of the interaction was calculated as -13.3 kcal·mol^{-1}, which is almost 15% of the bond energy of a Zn-O bond (70-80 kcal·mol^{-1}).[39] This clearly illustrates the crucial
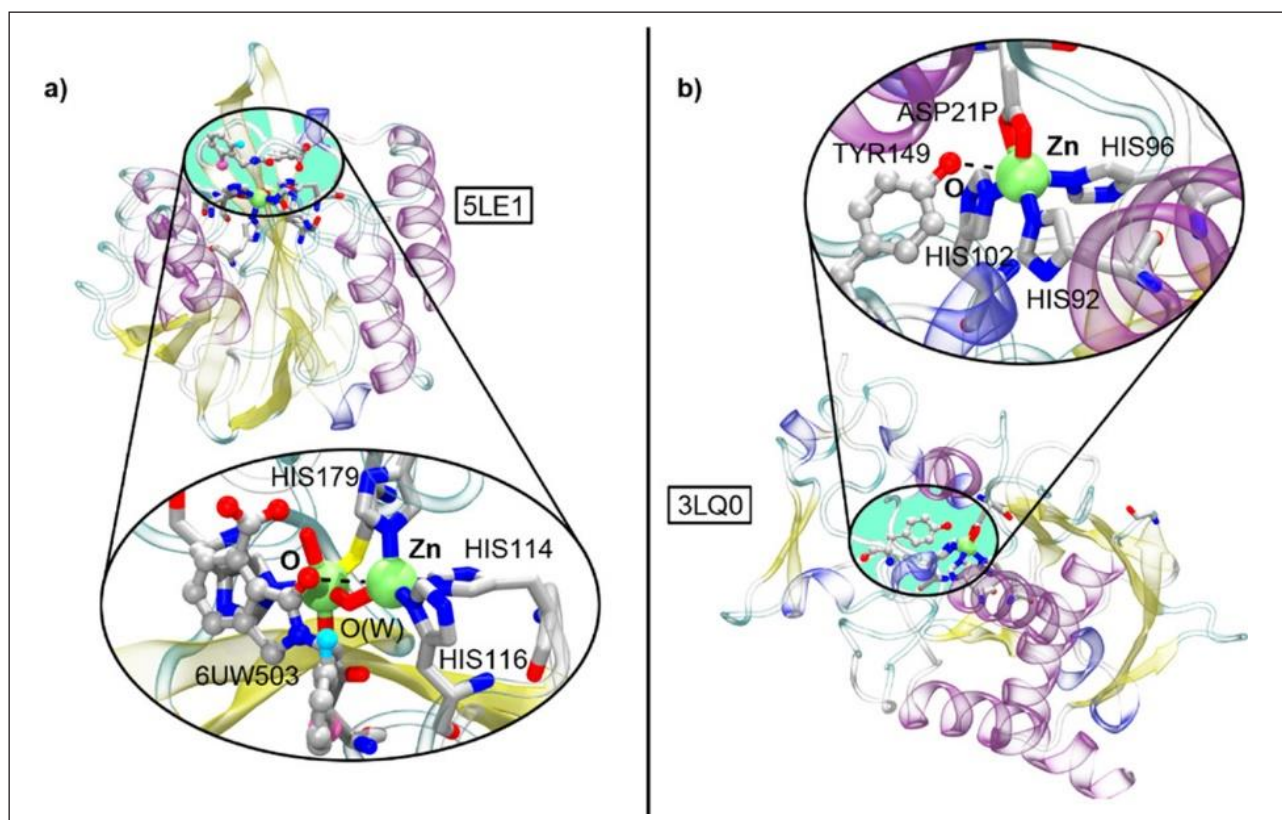

Figure 4: Partial views of X-ray crystal structures of (a) 5LE1 and (b) 3LQ0.

role of Sp-bonds in developing new therapeutic agents for specifically targeting Zn-dependent proteins.

The PDB file, 3LQ0, involves metallopeptidases (MPs) and their structure and mechanism of activation. These MPs carry out the peptide bond cleavage, and hence, their deregulation can cause various diseases such as cancer[40] and cardiovascular disorders.[41] Reports suggest that TYR149 residue shows a back and forth movement, also known as tyrosine switch, which creates a catalytic site at the Zn center in certain proteins.[42] In 3LQ0, we observed that the TYR149 residue forms Sp-bonds with the Zn catalytic center, which is facilitated by the positive electrostatic potential along the Zn-HIS96 axis (+89.1 kcal·mol^{-1}). Since spodium bonds are simple noncovalent interactions, this TYR149 residue can easily flip front and back upon substrate binding. During the catalytic cycle, a hydrogen bond replaces this residue and stabilizes the tetrahedral intermediate. This example shows how Sp-bonds can significantly contribute to the structural flexibility of the tyrosine switch rearrangement.

4. Conclusions

Spodium bonds, though less discovered, are one of the most abundant noncovalent interactions present in nature. These interactions significantly contribute to determining the structure of Zn-proteins and affect their functionality. In our work, we scanned the PDB database for Zn-proteins and looked for the presence of Sp-bonds using certain geometrical criteria. Since the interaction strength between Td Zn and its electron-rich partner was observed to be relatively stronger than all other cases, we shortlisted only those structures with Sp-bonds that demonstrate high directionality. A total of 13 PDB structures were taken into consideration as each of them showed a unique Zn environment, and energetic calculations were performed. The AIM and NCIplot analysis were performed for five structures to gain further insight, which showed that other noncovalent interactions are often found along with Sp-bonds, and these interactions support its formation. Two protein structures, 5LE1 and 3LQ0, were selected, and the biological implications of spodium bonding in such structures were explored in further detail. These examples showed the crucial role in inhibiting β-lactam antibacterials and in the catalytic cycle observed in metallopeptidases. We are hopeful that the findings of this work will provide valuable insights into the Sp-bonds and their functionality. This will be extremely useful in expanding the understanding of Zn as a Lewis acid in biological systems and designing new therapeutic agents, which is a valuable addition to the scientific community.

References

1. Schneider, H.-J. Binding Mechanisms in Supramolecular Complexes. *Angew. Chem. Int. Ed.* **2009,** *48*, 3924-3977.
2. Hunter, C. A.; Sanders, J. K. M. The Nature of .pi.-.pi. Interactions. *J. Am. Chem. Soc.* **1990,** *112*, 5525-5534.
3. Grabowski, S. J. What Is the Covalency of Hydrogen Bonding? *Chem. Rev.* **2011,** *111*, 2597-2625.
4. Cavallo, G.; Metrangolo, P.; Milani, R.; Pilati, T.; Priimagi, A.; Resnati, G.; Terraneo, G. The Halogen Bond. *Chem. Rev.* **2016,** *116*, 2478-2601.
5. Wang, J.; Jin, Z.; Cheng, J.; Li, Y. Assembling Structure of Single-Walled Carbon Nanotube Thin Bundles. *J. Phys. Chem. C* **2009,** *113*, 8132-8135.
6. Scheiner, S. The Pnicogen Bond: Its Relation to Hydrogen, Halogen, and Other Noncovalent Bonds. *Acc. Chem. Res.* **2013,** *46*, 280-288.
7. Bauzá, A.; Mooibroek, T. J.; Frontera, A. Tetrel-Bonding Interaction: Rediscovered Supramolecular Force? *Angew. Chem. Int. Ed.* **2013,** *52*, 12317-12321.
8. Grabowski, S. J. Boron and other Triel Lewis Acid Centers: From Hypovalency to Hypervalency. *ChemPhysChem* **2014,** *15*, 2985-2993.
9. Politzer, P.; Murray, J. S.; Clark, T. Halogen Bonding and Other σ-hole Interactions: A Perspective. *Phys. Chem. Chem. Phys.* **2013,** *15*, 11178-11189.
10. Alkorta, I.; Elguero, J.; Frontera, A. Not Only Hydrogen Bonds: Other Noncovalent Interactions. *Crystals* **2020,** *10*.
11. Chieh, C. Synthesis and Structure of Dichlorobis(thiosemicarbazide)mercury(II). *Can. J. Chem.* **1977,** *55*, 1583-1587.
12. Bauzá, A.; Alkorta, I.; Elguero, J.; Mooibroek, T. J.; Frontera, A. Spodium Bonds: Noncovalent Interactions Involving Group 12 Elements. *Angew. Chem. Int. Ed.* **2020,** *59*, 17482-17487.
13. Vallee, B. L.; Auld, D. S. Active-site Zinc Ligands and Activated H2O of Zinc Enzymes. *Proc. Natl. Acad. Sci. U S A* **1990,** *87*, 220-224.
14. Christianson, D. W. In *Advances in Protein Chemistry*;

Anfinsen, C. B.; Edsall, J. T.; Richards, F. M.; Eisenberg, D. S., Eds.; Academic Press, 1991; Vol. 42.

15. Dudev, T.; Lim, C. Principles Governing Mg, Ca, and Zn Binding and Selectivity in Proteins. *Chem. Rev.* **2003,** *103,* 773-788.

16. Christianson, D. W.; Cox, J. D. Catalysis By Metal-Activated Hydroxide in Zinc and Manganese Metalloenzymes. *Annu. Rev. Biochem.* **1999,** *68,* 33-57.

17. Christianson, D. W.; Lipscomb, W. N. Carboxypeptidase A. *Acc. Chem. Res.* **1989,** *22,* 62-69.

18. Cox, E. H.; McLendon, G. L. Zinc-dependent Protein Folding. *Curr. Opin. Chem. Biol.* **2000,** *4,* 162-165.

19. Plapp, B. V.; Savarimuthu, B. R.; Ferraro, D. J.; Rubach, J. K.; Brown, E. N.; Ramaswamy, S. Horse Liver Alcohol Dehydrogenase: Zinc Coordination and Catalysis. *Biochemistry* **2017,** *56,* 3632-3646.

20. Hao, Q.; Maret, W. Aldehydes Release Zinc from Proteins. A Pathway from Oxidative Stress/Lipid Peroxidation to Cellular Functions of Zinc. *FEBS J.* **2006,** *273,* 4300-4310.

21. Biswal, H. S.; Kumar Sahu, A.; Frontera, A.; Bauzá, A. Spodium Bonds in Biological Systems: Expanding the Role of Zn in Protein Structure and Function. *J. Chem. Inf. Model.* **2021,** *61,* 3945-3954.

22. Berman, H. M.; Westbrook, J.; Feng, Z.; Gilliland, G.; Bhat, T. N.; Weissig, H.; Shindyalov, I. N.; Bourne, P. E. The Protein Data Bank. *Nucleic Acids Res.* **2000,** *28,* 235-242.

23. Cordero, B.; Gómez, V.; Platero-Prats, A. E.; Revés, M.; Echeverría, J.; Cremades, E.; Barragán, F.; Alvarez, S. Covalent radii Revisited. *Dalton Trans.* **2008,** DOI:10.1039/b801115j 10.1039/b801115j, 2832-2838.

24. Heinig, M.; Frishman, D. STRIDE: A Web Server for Secondary Structure Assignment from Known Atomic Coordinates of Proteins. *Nucleic Acids Res.* **2004,** *32,* W500-W502.

25. Biovia, D. S.; Release, 2017.

26. Frisch, M. J.; Trucks, G. W.; Schlegel, H. B.; Scuseria, G. E.; Robb, M. A.; Cheeseman, J. R.; Scalmani, G.; Barone, V.; Petersson, G. A.; Nakatsuji, H.et al. Wallingford, CT, 2016.

27. Becke, A. D. Density-functional Exchange-energy Approximation with Correct Asymptotic Behavior. *Physical Review A* **1988,** *38,* 3098-3100.

28. Grimme, S.; Antony, J.; Ehrlich, S.; Krieg, H. A Consistent and Accurate Ab initio Parametrization of Density Functional Dispersion Correction (DFT-D) for the 94 Elements H-Pu. *J. Chem. Phys.* **2010,** *132,* 154104.

29. Weigend, F.; Ahlrichs, R. Balanced Basis sets of Split Valence, Triple zeta Valence and Quadruple zeta Valence Quality for H to Rn: Design and Assessment of Accuracy. *Phys. Chem. Chem. Phys.* **2005,** *7,* 3297-3305.

30. Weigend, F.; Häser, M. RI-MP2: First Derivatives and Global Consistency. *Theor. Chem. Acc.* **1997,** *97,* 331-340.

31. Ahlrichs, R.; Bär, M.; Häser, M.; Horn, H.; Kölmel, C. Electronic Structure Calculations on Workstation Computers: The Program System Turbomole. *Chem. Phys. Lett.* **1989,** *162,* 165-169.

32. Boys, S. F.; Bernardi, F. The Calculation of Small Molecular Interactions by the Differences of Separate Total Energies. Some Procedures with Reduced Errors. *Mol. Phys.* **1970,** *19,* 553-566.

33. Contreras-García, J.; Johnson, E. R.; Keinan, S.; Chaudret, R.; Piquemal, J.-P.; Beratan, D. N.; Yang, W. NCIPLOT: A Program for Plotting Non-covalent Interaction Regions. *J. Chem. Theory Comput.* **2011,** *7,* 625-632.

34. Alvarez, S. A Cartography of the van der Waals Territories. *Dalton Trans.* **2013,** *42,* 8617-8636.

35. Bondi, A. van der Waals Volumes and Radii. *J. Phys. Chem.* **1964,** *68,* 441-451.

36. Lee, S. Y.; Brem, J.; Pettinati, I.; Claridge, T. D. W.; Gileadi, O.; Schofield, C. J.; McHugh, P. J. Cephalosporins Inhibit Human Metallo β-lactamase Fold DNA Repair Nucleases SNM1A and SNM1B/apollo. *Chem. Commun.* **2016,** *52,* 6727-6730.

37. Li, G.-B.; Abboud, M. I.; Brem, J.; Someya, H.; Lohans, C. T.; Yang, S.-Y.; Spencer, J.; Wareham, D. W.; McDonough, M. A.; Schofield, C. J. NMR-filtered Virtual Screening Leads to Non-metal Chelating Metallo-β-lactamase Inhibitors. *Chem. Sci.* **2017,** *8,* 928-937.

38. Page, M. I.; Badarau, A. The Mechanisms of Catalysis by Metallo beta-lactamases. *Bioinorg. Chem. Appl.* **2008,** *2008,* 576297.

39. Krężel, A.; Maret, W. The Biological Inorganic Chemistry of Zinc ions. *Arch. Biochem. Biophys.* **2016,** *611,* 3-19.

40. López-Otín, C.; Matrisian, L. M. Emerging Roles of Proteases in Tumour Suppression. *Nat. Rev. Cancer* **2007,** *7,* 800-808.

41. Nalivaeva, N. N.; Fisk, R. L.; Belyaev, D. N.; Turner, J. A. Amyloid-Degrading Enzymes as Therapeutic Targets in Alzheimer's Disease. *Curr. Alzheimer Res.* **2008,** *5,* 212-224.

42. Grams, F.; Dive, V.; Yiotakis, A.; Yiallouros, I.; Vassiliou, S.; Zwilling, R.; Bode, W.; Stöcker, W. Structure of Astacin with a Transition-state Analogue Inhibitor. *Nat. Struct. Biol.* **1996,** *3,* 671-675.

***Dr. Himansu S. Biswal** Himansu Biswal is presently an Associate Professor in the School of Chemical Sciences, NISER, Bhubaneswar. After completing his doctoral research (2003–2009) from Tata Institute of Fundamental Research (TIFR) India with Prof. Sanjay Wategaonkar, Dr. Biswal carried out his postdoctoral research (2009–2011) with Prof. Michel Mons at CEA, Saclay, France, and then moved to Prof. Jennifer P. Ogilvie's research group at University of Michigan, USA, to work on 2D-electronic spectroscopy. His research efforts focus on understanding the noncovalent interaction (NCI) in biomolecules. Dr. Biswal's research group combines both spectroscopy, including supersonic jet spectroscopy and theoretical chemistry, to investigate the NCIs at the molecular level. The basic knowledge gained from molecular spectroscopy on different types of NCIs is extended to explore alternative green solvents for the long-term storage of DNA and RNA.*

***Akshay Kumar Sahu** was born in Chhatisgarh, India, in 1994. He received his B.Sc. and M.Sc. degrees from the Department of Chemistry, Bilaspur University, in 2015 and 2017. He did his M.Phil. from Dr. CV Raman University, Bilaspur, in 2018. He is currently doing his Ph.D. with Prof. Himansu Sekhar Biswal from the National Institute of Science Education and Research (NISER), Bhubaneswar, India, since 2019.*

***Shivam Mahapatra** was born in Odisha, India, in 1998. He is currently doing his Integrated Masters' at the Department of Chemistry, National Institute of Science Education and Research (NISER), Bhubaneswar, India. He is working with Prof. Himansu Sekhar Biswal for the completion of his Masters' project.*

Shedding Light onto the Photoluminescence Origin in Carbon Nanodots Synthesized via Top-down Method

Rohit Yadav, Aditya Yadav, Shubham Sharma, Chethana Rao and Chayan Kanti Nandi*

School of Basic Sciences, Indian Institute of Technology Mandi, H.P. India.
Email: chayan@iitmandi.ac.in

Abstract

Although progress have been made in understanding the origin of the multicolor photoluminescence in carbon nanodots (CNDs) synthesized via bottom-up approach, it still remains elusive for the CNDs obtained in top-down method. Here, we present the emission characteristics of the obtained materials synthesized step-by-step using modified hummers' method, a well-known top-down approach for the synthesis of CNDs. We show that, while graphite intercalation compound (GIC) doesn't show any emission, the multicolor emission is evolving from the pristine graphite oxide (PGO) itself. The same was also observed in graphene oxide (GO) and in CNDs synthesized in alkaline medium, however, it vanishes in acidic medium. The enormous amount of homogeneous oxygen containing surface functional groups, those fully covering the graphitic core structure, were found to be responsible for the excitation independent emission in acidic medium. On the other hand, the sub-multichromophoric groups, which were created by the attachment of reduced surface functional groups to the core structure were accountable for excitation dependent emission in alkaline medium.

Keywords: Carbon nanodots, top-down synthesis, bottom-up approach, fluorescence origin, multicolor emission

1. Introduction

Carbogenic nanodots (CNDs), owing to their remarkable properties like high brightness, low toxicity and aqueous solubility, emerging rapidly in bioimaging, photovoltaics, optoelectronics etc.[1-4] CNDs are very small in size, typically ranging from 2-5 nm.[5] Usually, CNDs possess 8-10 crystalline or amorphous graphene layers with sp^2 hybridized graphitic carbon core embedded by sp^3 hybridized epoxy, hydroxy, oxide and carboxyl functional groups.[6] One of the unique features in CNDs is their excitation dependent multicolor photoluminescence.[7-10] Although various mechanism to explain the behavior of such multicolor emission is proposed, the actual photoluminescence mechanism and the corresponding chemical structure of these CNDs are still elusive.

CNDs were first isolated as a dot material from arc-discharge soot by Xu et al. in 2004 during the synthesis of carbon nanotubes.[11] Unfortunately, the quantum yield was found to be extremely low and subsequently, several top-down methods with their surface passivating agents were reported to increase the quantum yield but only upto 10%.[12] Interestingly, in all of the reports, the photoluminescence spectra of the CNDs was found to be dependent on the excitation wavelength. Considering the synthesis method, where there is a chance of producing heterogeneous mixture, the multicolor emission was attributed by the quantum confinement effect. However, at a later stage, the quantum confinement was overruled, as in several instances, the larger sized particle showed blue emission, while smaller sized particle showed red emission.

While the photoluminescence in real CNDs was a factual problem, the synthesis of CNDs via a top-down approach to increase the quantum

yield and get the homogeneous structure posed another problem. Recent reports suggest that the fluorescence in CNDs synthesized via bottom-up approach may significantly originate from molecular fluorophores and/or their aggregates, polymer dots or quasi CNDs (molecular fluorophores attached to the core of CNDs), which were produced as by-products during CNDs synthesis.[5,13,14] As a result, the attribution of photoluminescence properties of the CNDs in several reports may be affected by erroneous conclusions and misleading artifacts.[15] Recently, while the issues in photoluminescence properties of CNDs have been addressed to an extent, the origin of the excitation dependent photoluminescence in actual CNDs synthesized via top-down method is still remains an issue.

Here, using graphite as the precursor, we present the step-by-step emission characteristics of the obtained materials synthesized via modified hummers' method, a well-known top-down method for CNDs synthesis. We present that the multicolor emission actually evolved from the PGO sheet itself in a top-down approach and it was continued to be found out in GO and then smaller size CNDs when synthesized upon treatment of GO in alkaline medium. Surprisingly, the multicolor emission vanishes and excitation independent emission was observed when CNDs synthesized in acidic medium. Several spectroscopic and microscopic techniques proposed that the enormous amount of homogeneous oxygen containing surface functional groups fully covering the graphitic core structure were responsible for the excitation independent emission in acidic medium. On the other hand, the sub-multichromophoric groups, which were created by attaching reduced surface functional groups to the core structure, were accountable for excitation dependent emission in alkaline medium.

2. Results and discussion

The detailed step-by-step synthesis of GIC, PGO and GO using modified hummers' method

is presented in **Figure 1a**. At first, GIC was produced by treating 1 g graphite powder and 0.5 g $NaNO_3$ in concentrated H_2SO_4 (23 ml) and stirred for 1 h. In this step, intercalation of the sulphate ions occurred in between the graphene layers.[16] Next, a potent oxidizing agent $KMnO_4$ (3g) was slowly added, followed by constant stirring for 12 h to synthesize PGO. This step involved further intercalation and oxidation of the intercalated compound. Subsequently, once PGO was formed, 500 ml deionized water was added to it, stirred for 2 h and then, 5 ml H_2O_2 was added to the above solution, followed by stirring for 1 h. The residue was separated from the solution by centrifugation at ~10000 rpm and GO was obtained as black residue.

The corresponding UV-VIS spectra as presented in **Figure 1b-d** confirms the signature of π-π* (234 nm) and n-π* (300 nm) transitions largely in GO, slightly in PGO but not in GIC. These data suggest the incorporation of functional groups such as C=O, -OH and COOH. The emission spectra of GIC, PGO and GO are presented in **Figure 1e-g**. It is interesting to observe the absence of any emission in GIC, while complete excitation dependent emission spectra in PGO, and both excitation dependent and independent emission spectra were observed in GO. As a result, it can be concluded that the excitation dependent emission starts appearing in PGO, where the incorporation of functional groups on the surface, edges (connected to core structure) might play an important role, as discussed later.

The thermal stability of GO was monitored by the thermogravimetric analysis (TGA) data. The TGA curve showed the first weight loss below 100 °C owing to the physically absorbed water molecules on the surface of GO (**Figure 2a**). In the next stage, i.e. 150-250 °C, the pyrolysis of the oxygen-containing functional groups on the GO sheets is responsible for the mass loss. A slight mass loss in the range 250-480 °C was seen and above 500 °C temperature and complete mass loss of the species was noted.[17] Powder
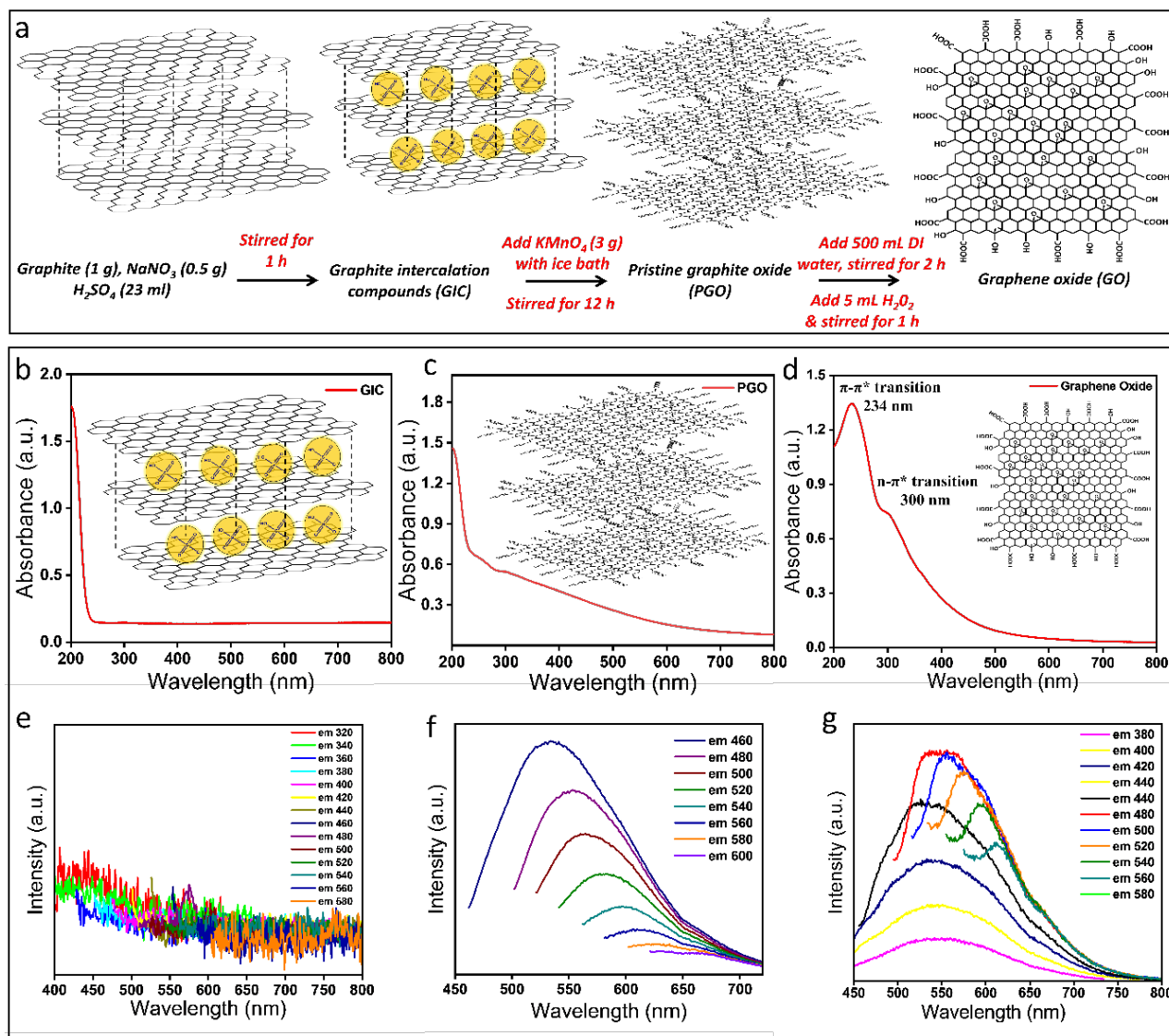
Fig. 1 *(a) Schematic for the synthesis of GIC, PGO and GO from graphite powder using modified Hummers' method. (b-d) Absorption spectra of GIC, PGO and GO. (e-g) Emission spectra of GIC, PGO and GO.*

X-ray Diffraction (PXRD) spectrum revealed two significant peaks, the peak at ~24.5° represents the (002) plane of graphitic carbon while a peak at 9.32° represents the oxidation of graphene sheets (**Figure 2b**).[18] In addition, we recorded the Raman spectrum of GO. Raman spectroscopy, a non-destructive but very powerful to identify the nature of carbon based materials. Two types of vibration, namely in-plane vibrations of sp^2 bonded carbon atoms, designated as G band (~1580 cm^{-1}) and the out of plane vibrations, designated as D band (~1360 cm^{-1}) are the

important signatures in Raman spectroscopy for graphene based materials. The D and G bands for the defect and graphitic states at 1350 cm^{-1} and 1600 cm^{-1} were clearly observed in GO. This data signifies the crystalline nature in GO with some defects states which are ascribed to the different functional groups attached to the graphitic domain (**Figure 2c**). Transmission electron microscope (TEM) images revealed sheets like structures of GO (**Figure 2d**).

Next, we synthesized CNDs from GO via two different experimental conditions i.e. acidic
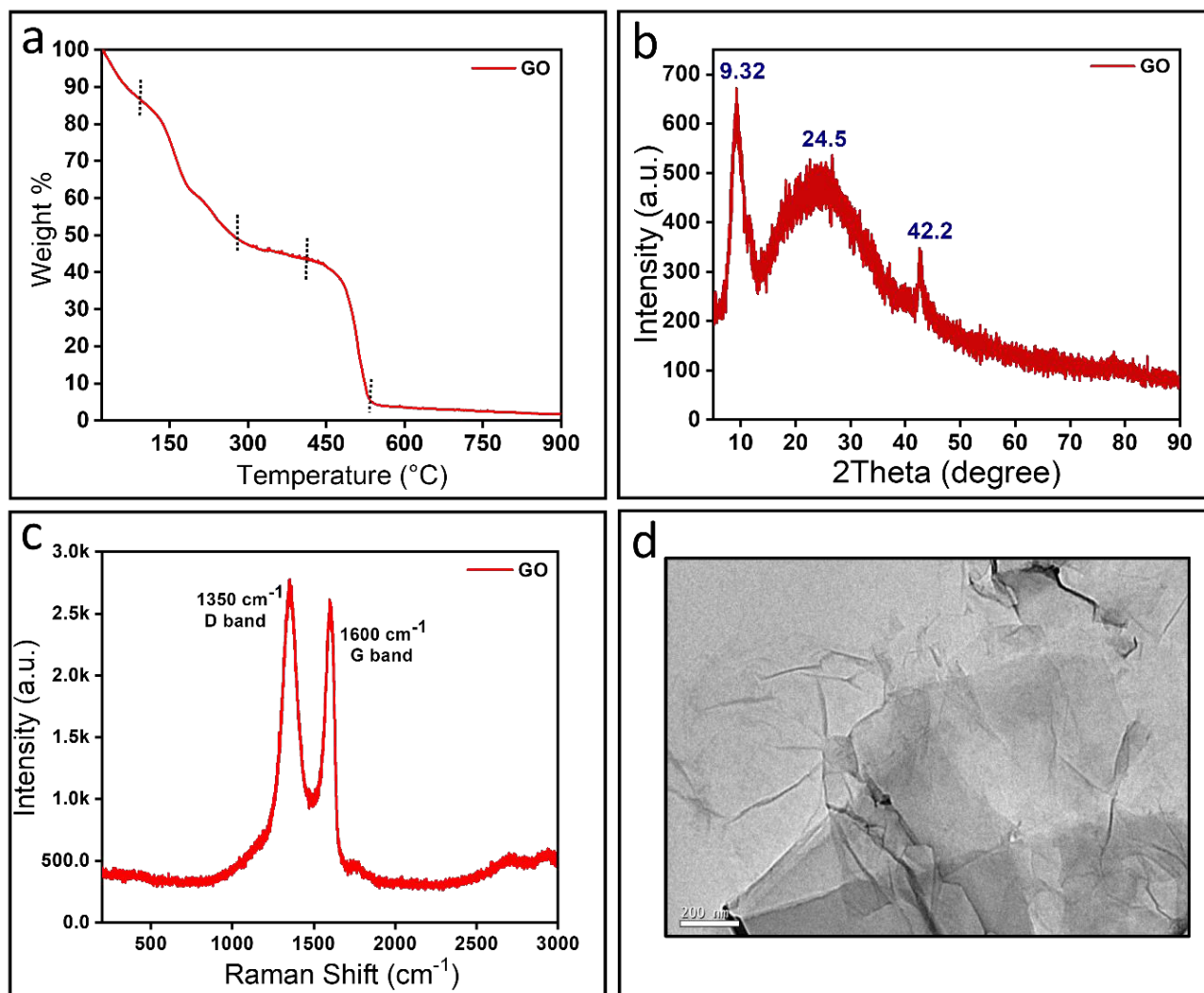
Fig. 2 *(a) TGA spectra of GO show the thermal stability at various temperature ranges. (b) Powder XRD spectrum of GO. (c) Raman spectrum of GO shows clear D and G bands corresponding to the defect and graphitic signature. (d) TEM image of the GO clearly shows the sheet like structure.*

(mixture of H_2SO_4 + HNO_3) and basic (NaOH solution) as shown in the schematic diagram (**Figure 3**). In acidic conditions, 0.2 g of GO was dissolved in 10 ml H_2SO_4 (1 M) and 10 ml HNO_3 (1 M) solution. The same amount of GO was dissolved in 1 M NaOH for the basic condition. Both the solutions were sonicated for 10 min for the complete dissolution of GO and then transferred in different autoclaves for heating at 180 °C for 12 h. After the completion of the reaction, the autoclaves were cooled to room temperature. The crude mixture of the product was first passed through the 0.22 um membrane in order to remove any unreacted GO. The filtered

solution was then centrifuged at ~10000 rpm to remove larger species left after the filtration. The supernatant solution thus collected was purified via dialysis membrane (1-3 kDa). After purification of both the systems, the solutions were characterized individually to get an insight into CNDs. The CNDs synthesized in acidic medium will be called as ACNDs and CNDs synthesized in alkaline medium will be called as BCNDs in the upcoming discussion.

The UV-Vis absorption spectra of both ACNDs and BCNDs were recorded. The absorption was mainly concentrated in the lower wavelength region, i.e. 200-390 nm signifying
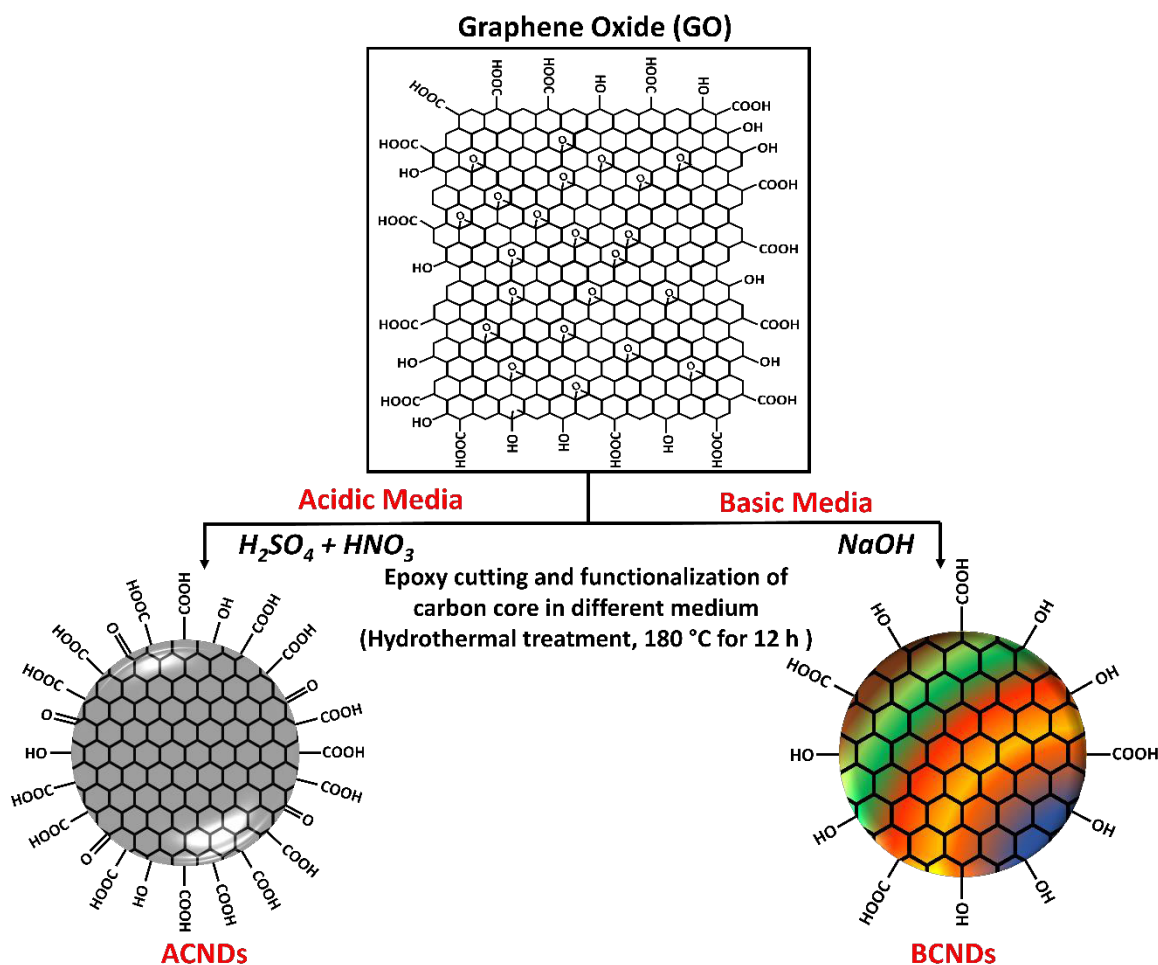
Fig. 3 *Schematic for the synthesis of ACNDs (left) and BCNDs (right) using the GO as precursor material.*

absorbance from п-п* transition in the aromatic domain and n-п* transition in C=O, -OH and COOH functional groups (**Figure 4a & 4d**). The measured emission spectra for both ACNDs and BCNDs showed contradictory but interesting results. In ACNDs, the structured emission with a peak maxima at around 410 nm and with completely excitation independent emission was observed (**Figure 4b**). The excitation spectra of ACNDs was a mirror image of the emission spectra as shown in **figure 4c**. However, in case of the BCNDs, the emission spectra were found to be excitation dependent which is the characteristic feature of the CNDs as reported earlier in top-down approach (**Figure 4e**). The measured excitation spectra was also closely mirror image for BCNDs as well (**Figure 4f**).

Surprisingly, the excitation spectra in both cases have a high resemblance, suggesting that similar type of functional groups might be responsible in the emission of both ACNDs and BCNDs.

To understand the contradicted emission characteristics observed in ACNDs and BCNDs, we carried out a detailed characterization of the materials using Raman spectroscopy, atomic force microscopy (AFM), TEM and X-ray photoelectron spectroscopy (XPS). In case of ACNDs, there was not any signature of D and G bands rather a high fluorescence background was observed (**Figure 5a**). In contrast, the presence of D and G bands on the top of the fluorescence background clearly be seen in BCNDs (**Figure 5d**). However, interestingly, the tapping mode AFM images
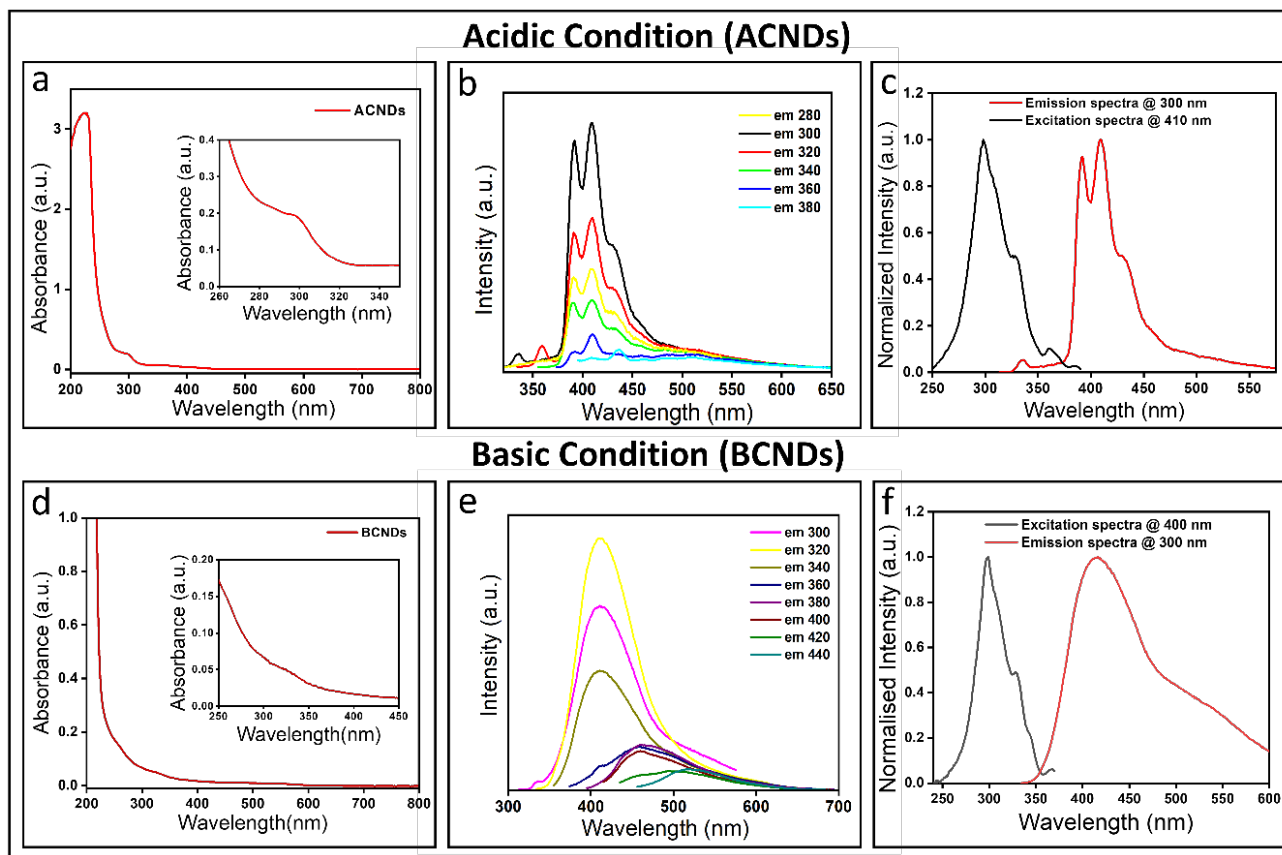
Fig. 4 *(a) Absorption spectra of ACNDs shows different electronic transition (inset shows a clear shoulder around 300 nm). (b) Emission spectra of ACNDs shows excitation independent behavior at various excitation wavelengths. (c) Comparison of emission and excitation spectra shows mirror symmetry in case of ACNDs. (d) Absorption spectra of BCNDs. (e) Emission spectra of BCNDs show excitation dependent behavior at various excitation wavelengths. (f) Comparison of emission and excitation spectra shows closely mirror image for BCNDs as well.*

showed the spherical morphology of both the CNDs with a height of 2-6 nm (**Figure 5b & 5e**). In addition, the TEM data, as presented in **Figures 5c & 5f** also showed the dots with a size 3-5 nm in both the CNDs. Nevertheless, the extent of dots formation was much larger in numbers in BCNDs than in ACNDs. In addition, ACNDs also showed some aggregated structure.

For a better understanding of the functional group on the ACNDs and BNCDs, we carried out XPS measurements. The XPS survey scan shows promising outcomes, which shed light on the different extent of functional groups in both the CNDs. A strong signal of C1s at 285 eV and O1s peaks at 531 eV for both ACNDs and BCNDs (**Figure 6a & 6d**) was observed. Interestingly,

the high-resolution spectrum of C1s and O1s of ACNDs confirms the presence of the large excess of C-OH, C-O, C=O and COOH functional groups along with C=C and C-C functional groups (**Figure 6b & 6c**). On the other hand, the high-resolution spectrum of C1s and O1s in BCNDs showed a substantial amount of C=C, C-C, C=O but a less or negligible amount C-OH and COOH functional groups (**Figure 6e & 6f**). In addition, the amount of C=O groups also was found to be a lesser extent in BCNDs than ACNDs.

All the experimental findings suggested that synthetic conditions play a decisive role in the emission behavior of CNDs. While in both the cases dots like structures (as confirmed by AFM and TEM images) are formed, the Raman
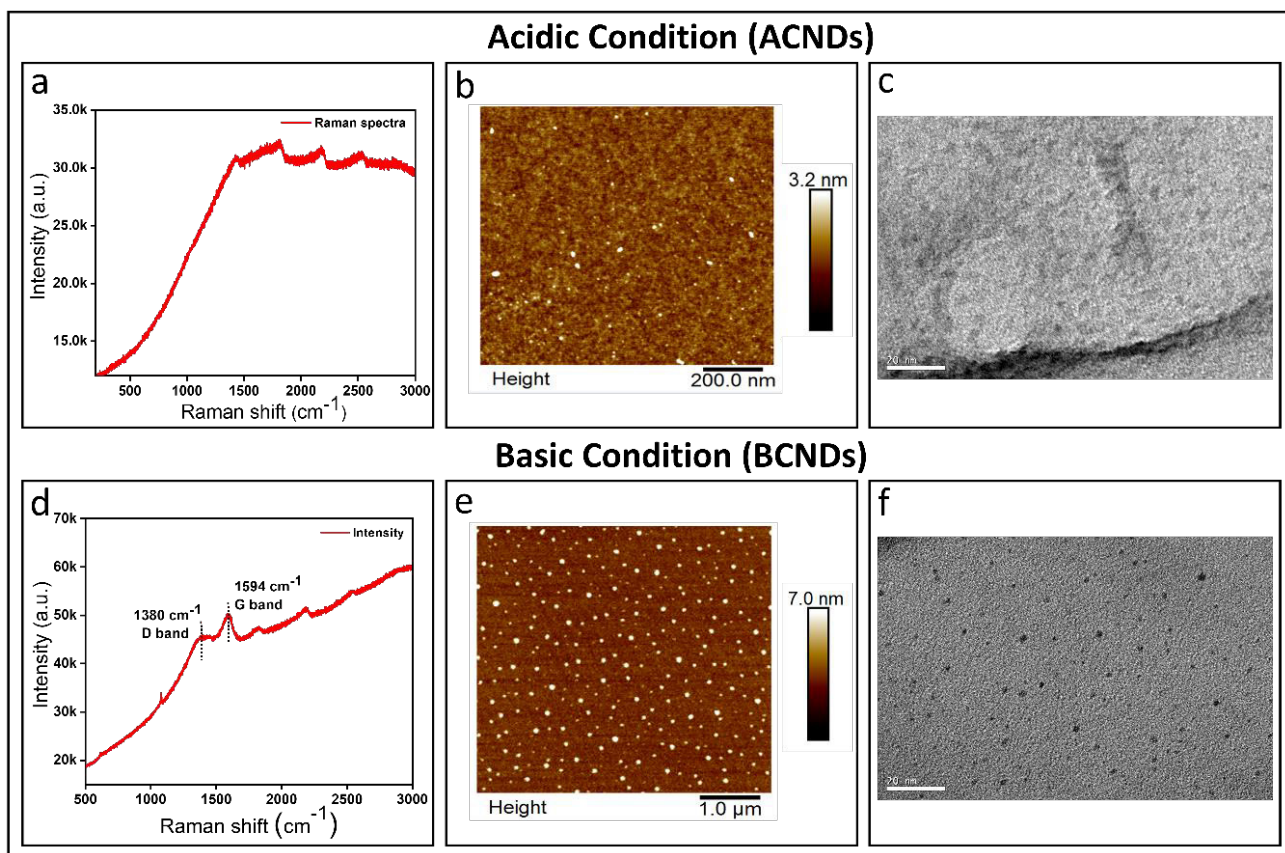
Fig. 5 *(a) Raman spectra of ACNDs shows fluorescence background. (b) AFM image of the ACNDs. (c) TEM image of ACNDs shows dots like structures with some aggregated structures. (d) Raman spectra of BCNDs shows clear D and G band buried under a fluorescence background representing the defect and graphitic signature. (e) AFM image of the BCNDs. (f) TEM image of BCNDs shows clear dots like structures.*

spectroscopy data doesn't show the typical D and G bands for ACNDs, rather a huge fluorescence background was obtained in this case. On the other hand the BCNDs showed proper D and G bands with a fluorescence background. As a result, it could be concluded that the difference in the surface functional groups played a crucial role for the difference in emission characteristics in ACNDs and BCNDs. The results suggested that the enormous amount of homogeneous oxygen containing surface functional group (C-OH, C-O, C=O and COOH) fully covering the graphitic core structure were responsible for the excitation independent emission in acidic medium. The sub-multichromophoric group, which were created due to the reduced surface functional groups attached to core structure, was responsible for excitation dependent emission in alkaline medium.

4. Conclusions

In summary, we unveil the photoluminescence mechanism of the CNDs obtained by top-down method using modified hummers' method. The multicolor emission was observed in CNDs when synthesized in alkaline medium, in contrary, excitation independent emission was observed in CNDs synthesized in acidic medium. The enormous amount of homogeneous oxygen containing surface functional groups in ACNDs were found to be responsible for the excitation independent emission in acidic medium. The sub-multichromophoric group in BCNDs was responsible for excitation dependent emission in alkaline medium.
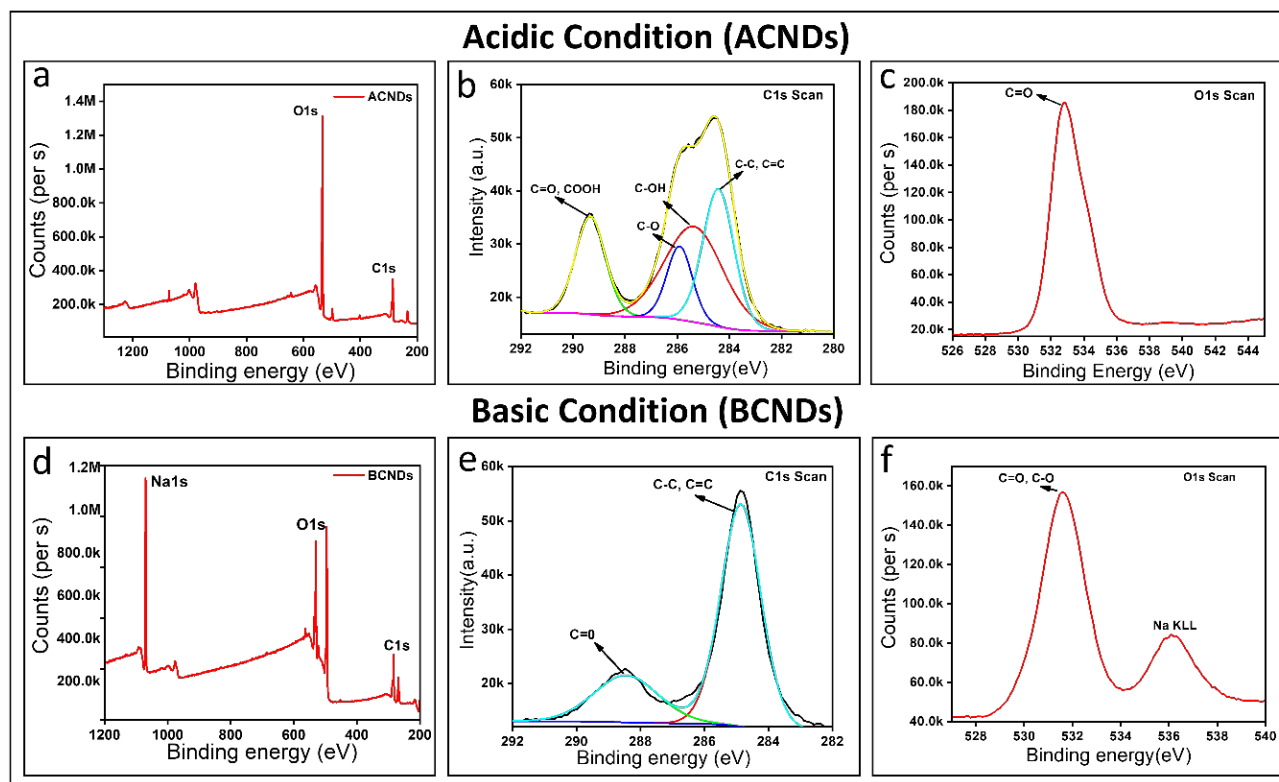
Fig. 6 *(a) XPS survey scan of ACNDs. (b) High-resolution XPS spectra of C1s for ACNDs show the presence of C=O, COOH, C-O, C-OH, C-C and C=C functional groups. (c) High-resolution O1s spectra of ACNDs show peak for C=O functional group. (d) XPS survey scan of BCNDs. (e) High-resolution XPS spectra of C1s for BCNDs show the presence of C=O, C-C and C=C functional groups. (f) High-resolution O1s spectra of BCNDs show peaks for C=O, C-O functional groups.*

References

1   S.-T. Yang, L. Cao, P. G. Luo, F. Lu, X. Wang, H. Wang, M. J. Meziani, Y. Liu, G. Qi and Y.-P. Sun, *J. Am. Chem. Soc.*, 2009, **131**, 11308–11309.

2   S. Paulo, E. Palomares and E. Martinez-Ferrero, *Nanomaterials*, 2016, **6**, 157.

3   T. Feng, X. Ai, G. An, P. Yang and Y. Zhao, *ACS Nano*, 2016, **10**, 4410–4420.

4   X. Li, M. Rui, J. Song, Z. Shen and H. Zeng, *Adv. Funct. Mater.*, 2015, **25**, 4929–4947.

5   N. C. Verma, A. Yadav and C. K. Nandi, *Nat. Commun.*, 2019, **10**, 2391.

6   S. Zhu, Y. Song, X. Zhao, J. Shao, J. Zhang and B. Yang, *Nano Res.*, 2015, **8**, 355–381.

7   R. Liu, D. Wu, S. Liu, K. Koynov, W. Knoll, Q. Li, [R Liu, D. Wu, S. Liu, K. Koynov, W. Knoll and Q. Li, *Angew. Chemie Int. Ed.*, 2009, **48**, 4598–4601.

8   Y. Zhou, E. M. Zahran, B. A. Quiroga, J. Perez, K. J. Mintz, Z. Peng, P. Y. Liyanage, R. R. Pandey, C. C. Chusuei and R. M. Leblanc, *Appl. Catal. B Environ.*, 2019, **248**, 157–166.

9   Y. P. Sun, B. Zhou, Y. Lin, W. Wang, K. A. S. Fernando, P. Pathak, M. J. Meziani, B. A. Harruff, X. Wang, H. Wang, P. G. Luo, H. Yang, M. E. Kose, B. Chen, L. M. Veca and S. Y. Xie, *J. Am. Chem. Soc.*, 2006, **128**, 7756–7757.

10   S. H. Lee, D. Y. Kim, J. Lee, S. B. Lee, H. Han, Y. Y. Kim, S. C. Mun, S. H. Im, T. H. Kim and O. O. Park, *Nano Lett.*, 2019, **19**, 5437–5442.

11   X. Xu, R. Ray, Y. Gu, H. J. Ploehn, L. Gearheart, K. Raker and W. A. Scrivens, *J. Am. Chem. Soc.*, 2004, **126**, 12736–12737.

12   Y.-P. Sun, B. Zhou, Y. Lin, W. Wang, K. A. S. Fernando, P. Pathak, M. J. Meziani, B. A. Harruff, X. Wang, H. Wang and others, *J. Am. Chem. Soc.*, 2006, **128**, 7756–7757.

13   N. Soni, S. Singh, S. Sharma, G. Batra, K. Kaushik, C. Rao, N. C. Verma, B. Mondal, A. Yadav and C. K. Nandi, *Chem. Sci.*, 2021, **12**, 3615-3626.

14 S. Khan, A. Sharma, S. Ghoshal, S. Jain, M. K. Hazra and C. K. Nandi, *Chem. Sci.*, 2017, **9**, 175–180.

15 J. B. Essner, J. A. Kist, L. Polo-Parada and G. A. Baker, *Chem. Mater.*, 2018, **30**, 1878–1887.

16 A. M. Dimiev and J. M. Tour, *ACS Nano*, 2014, **8**, 3060–3068.

17 P. Cui, J. Lee, E. Hwang and H. Lee, *Chem. Commun.*, 2011, **47**, 12370–12372.

18 S. Saxena, T. A. Tyson, S. Shukla, E. Negusse, H. Chen and J. Bai, *Appl. Phys. Lett.*, 2011, **99**, 013104.

Rohit Yadav *studied Chemistry at Indian Institute of Technology Mandi, India (M.Sc. 2021) and carried out his master's thesis under the supervision of Prof. Chayan Kanti Nandi. Since 2021, he has been carrying out Ph.D. research at Johannes Kepler University, Austria in Biophysics under the supervision of Prof. Peter Pohl. His research focused on protein translocation, fluorescence microscopy, electrophysiology, fluorescence correlation spectroscopy and protein reconstitution.*

Aditya Yadav *studied Chemistry at the University of Delhi, India (M.Sc. 2014). He then joined CSIR IIP Dehradun, India for his project work on methane activation. Since 2018 he has been carrying out Ph.D. research at the Indian Institute of Technology Mandi, India under the supervision of Prof. Chayan Kanti Nandi. His research concentrates on the design and development of nanomaterial probes (AuNCs "Gold nanocluster" and SPIONs), highly specific to cellular organelles for superresolution applications.*

Shubham Sharma *studied Chemistry at the Indian Institute of Technology (IIT) Mandi, India (M.Sc. 2018). Since 2020 he has been carrying out Ph.D. research work at IIT Mandi, under the supervision of Prof. Chayan Kanti Nandi. His research broadly focuses on exploration of the fundamentals of Carbon nanodots (CNDs), which involves delving into origins of their photoluminescence behavior and finally using these moieties for the different biological applications.*

Chethana Rao *procured Master's degree from the National Institute of Technology Karnataka, Surathkal, India, in physical science. She is pursuing her Ph.D. under the supervision of Prof. Chayan Kanti Nandi at the Indian Institute of Technology Mandi, India, since 2017. Her research is based on exploring methods of using carbon dots for bioimaging applications using Fluorescence lifetime imaging and Transmission Electron microscopy. It also involves development of doxorubicin delivery nanocarriers with high efficacy at low dosage.*

Chayan Kanti Nandi *received his Ph.D. in 2006 from the Indian Institute of Technology Kanpur India. He completed two consecutive postdocs from Germany in 2009 and at Princeton University in 2010. Currently, he is an professor at the Indian Institute of Technology Mandi India. He has been awarded as Alexander von Humboldt fellow in 2007. In 2019, he received CRSI bronze medal award for his outstanding research in chemistry. His current research is to design new fluorescent nanoprobes for localization based superresolution microscopy.*

Semiconductor and Graphene Quantum Dots: From a Perspective of Biosensing Applications

Abhijit Saha

UGC-DAE Consortium for Scientific Research,
Kolkata Centre, III/LB-8, Bidhannagar, Kolkata 700 106, India
E-mail: abhijit@alpha.iuc.res.in

Abstract

The applications of quantum dots (QDs) as sensors ranges from simple fluorescent labels, as used in immunoassays, to intrinsic sensors that utilize the inherent photophysical response of QDs to fluctuations in temperature, electric field, or ion concentration. In more complex arrangements, QDs and biomolecular recognition moieties, like enzymes, antibodies are conjugated with a third component to modulate the optical signal through the mode of energy transfer. QDs can act as donors, acceptors, or as both in the energy transfer-based sensors utilizing Förster resonance energy transfer (FRET), nanometal surface energy transfer (NSET), or charge or electron transfer. The changes in both spectral response and photoluminescent lifetimes have been successfully harnessed to produce sensitive sensors and multiplexed devices. While technical challenges related to biofunctionalization and the expensive instrumentation have thus far prevented broad implementation of QD-based sensing in clinical or commercial settings, interest is growing in improvements of the bioconjugation methods and detection schemes, using simple consumer devices like cell phone cameras to lowering barrier for broad use of more sensitive QD-based devices.

Compared with conventional dye molecules and semiconductor QDs, grapheme quantum dots (GQDs) have many advantages including their low toxicity, excellent biocompatibility, good resistance to photobleaching, stable emission and easy modulation. Therefore, GQDs are expected to be outstanding alternatives to organic dyes and semiconductor QDs for fluorescence sensing platforms. In this presentation, some typical aspects of synthesis, spectroscopic characterization and biomolecular sensing of these materials will be discussed.

1. Introduction

Over the last two decades, semiconductor quantum dots (SQDs) have dominated the field of nanoscience and nanotechnology owing to unique and well characterized optical properties. Among various types of nanomaterials, semiconductor nanocrystals or quantum dots and graphene have attracted tremendous interest because of myriads of possible diverse applications[1]. The large surface area to volume ratios of the nanoparticulatefluorophores enables them to be endowed with several modalities, including the targeting of specific biomarkers and drug delivery capabilities, promoting them as therapeutic agents as well. Among various types of diagnostic detection methods, fluorescence-based techniques offer unique practicalities, such as high sensitivity, specificity, activatable signal and multiplexing capabilities and fast acquisition times. SQDs like CdSe, ZnSe, ZnTe, CdS, CdTe, ZnS, PbSe, etc. stabilized by some suitable capping ligands, show size dependent optical properties having broad excitation with narrow emission. High luminescence quantum yield and symmetric emission exhibited by SQDs made them promising candidate for the applications related to sensing of metal ions and biomolecules, *in-vitro*bioimaging, and immunosensing assays.[8–13]

Furthermore, large surface area to volume ratio of SQDs can be utilized for the attachment of multiple biomolecules to its surface, in order to produce desired composite for application in the biomedical field.[14]However, semiconductor QDs being unsuitable for *in vivo* applications due to reports of toxicity issues relating to the presence of heavy metals commonly found in their composition and also the availability of said elements in nature is relatively low. In contrast, carbon, on the other hand, is abundant, inexpensive and is generally considered to be biocompatible. Thus, GQDs have emerged as potential alternatives.

Zero-dimensional (0D) GQDs, the latest carbon family member, contains single or few layers of graphene with different functionalized groups on its edge[16,17] with a size less than 20 nm[18]stable photoluminescence (PL, .GQDs shows several interesting characteristics, such as stable photoluminescence, biocompatibility, high PL quantum yield,, excellent solubility, surface grafting and so on.[19,20]we studied its effects on the embryonic development of zebrafish.\nMethods\nIn vivo, biodistribution and the developmental toxicity of GQDs were investigated in embryonic zebrafish at exposure concentrations ranging from 12.5-200 µg/mL for 4-96 h post-fertilization (hpf Unique properties shown by GQDs, make it a promising candidate for applications in the diverse field of modern scientific research and technology. The applications of GQDs in optoelectronic devices, bioimaging, biosensor, drug delivery, and other biomedical fields are being extensively investigated.[21-24]

In this article, the properties of two types of quantum dots are discussed in the context of using them as fluorescent labels for sensing biologically important molecules. As guiding principles for suitability of the label/probe include: (a) the optical properties of the probes, such as their brightness, photostability and convenient excitation; (b) their chemical properties, such as the solubility, stability under experimental or physiological conditions, availability of chemical modification strategies for labelling and appropriate conjugation; (c) the potential toxicity and biocompatibility of the probe. The aim of this article is not to deliver an extensive summary of the literature, but rather to provide a a glimpse of functionalities of the two quantum dots types in order to facilitate the choice between them for a particular application.

2.1. Biological applications

Biocompatibility is perhaps the most important property of a newly-developed material when considering its utilisation for biomedical applications. It is usually evaluated by considering the cytotoxicity (*in vitro* toxicity) of the material and through in vivo studies that look at biodistribution, clearance routes and longterm side effects post-injection. Biocompatibility is a highly complex property that cannot be fully predicted based on the composition of the material. For many colloidal nanomaterials, factors such as nanoparticle size, shape, aspect ratio, surface functionalisation, encapsulation layers, presence of external excitation source and (especially) dose have all been found to have a profound effect.A number of biocompatibility studies have been carried for both SQDs and GQDs. With respect to the former, the toxicity of commonly used SQDs has raised a lot of concern due to the intrinsic toxicity of such Cd-containing quantum dots. Consequently, recent years saw a shift in the scientific focus towards the development of non-heavy metal based SQDs or their encapsulation in protective layers, both of which have shown reduced toxicity. On the other hand, the demand for safer alternatives generated interest in carbon-based nanoprobes, including graphene quantum dots, which promised intrinsic biocompatibility. Another contributor to SQD's toxicity in *vitro* and *in vivo* is the free radical generation, such as singlet oxygen, hydroxyl radical ($\cdot$OH), superoxide anion (O_2^-), hydrogen peroxide (H_2O_2), and peroxynitrite ($ONOO^-$). SQDs are extremely photosensitive and are known to transfer the

energy to molecular oxygen forming singlet oxygen, which reacts with water and catalyses the enzymatic reaction in order to produce reactive oxygen or nitrogen species (ROS/RNS). The free radicals can cause damage not only on the cellular level (cell apoptosis) but can also lead to mutations in the DNA. Some consider oxidative stress to be the primal cause of toxicity of QDs *in vitro*. However, this production of singlet oxygen can also be used to an advantage, where this particular property showed potential in the application of PDT for a more targeting cancer therapy as discussed previously. In an attempt to reduce the toxicity of SQDs, shell coating method has been applied on numerous occasions which, as the name suggests, involves coating of SQD cores with shells of another inorganic material (e.g. ZnS), small molecules, polymers, proteins or silica.9,127 The coatings allow for a slower transport of oxygen to the core surface thus reducing the rate of ROS production, however, they do not completely inhibit it and they tend to be susceptible to degradation in the cellular environment. GQDs, on the other hand, were first considered because of their intrinsic low toxicity owing to their carbon-based compositions and they have since become an attractive target for biomedical applications. However, even though GQDs have been shown to have quite a low toxicity, it is not altogether absent.

The application of carbon nanomaterial in the biological area has been one of the leading research interests of researchers since recent past years. In particular, GQDs are one of the carbon nanomaterials which has played an important role in the diverse field of applications. To understand the properties shown by GDQs, extensive research has been carried out using different techniques, like doping, surface and edge functionalization, shape, size controlling, and so on. Important features of synthesized GQDs are high quantum yield, tunable PL emission, good water solubility, resistance to photobleaching, low toxicity, and biocompatibility. These unique properties make GQDs a promising carbonaceous nanomaterial for bioimaging and biosensing. Here, advances in bioanalytical applications of semiconductor and GQDs have been highlighted.

2.2. Biosensing

By virtue of their unique size dependent physical and chemical characteristics, semiconductor QDs may act as optical indicators for the development of various biosensors. QDs have triggered extensive attention in describing sensitive detection of target molecules using QDs based sensor. Because of its high sensitivity and simplicity in measurements, QD-based fluorescence sensor for determination of chemical and biological molecules have dragged lot of attention of the researchers Owing to their unique spectral properties and physicochemical stability, it is apparent that quantum dots effectively address some of the limitations encountered by conventional fluorophores currently forming the basis for biosensors and bioanalytical assays, yet quantum dot use in biosensing applications has thus far been limited to proof-of-concept experiments. Recent advances in adapting quantum dots for predominantly in vitro biosensing applications, such as immunoassays, nucleic acid detection, and fluorescence resonance energy transfer (FRET)-based sensing are being investigated. Here, we focus on the limitations that have precluded quantum dots from finding widespread use in biosensing applications.

Multivalency renders quantum dots an attractive nanoscaffold that can accommodate multiple copies of different functional elements. Not only can such architecture result in higher sensitivity and lower limits of detection, but it may also serve as a basis for multifunctional biosensors. However, as previously mentioned, it is current lack of control over conjugation stoichiometry as well as the orientation and conformation of a surface sensing element that is a major obstacle to fully capturing the advantages of multivalency. Failure to determine the exact number and orientation in space of a surface sensing element in a reproducible manner can lead
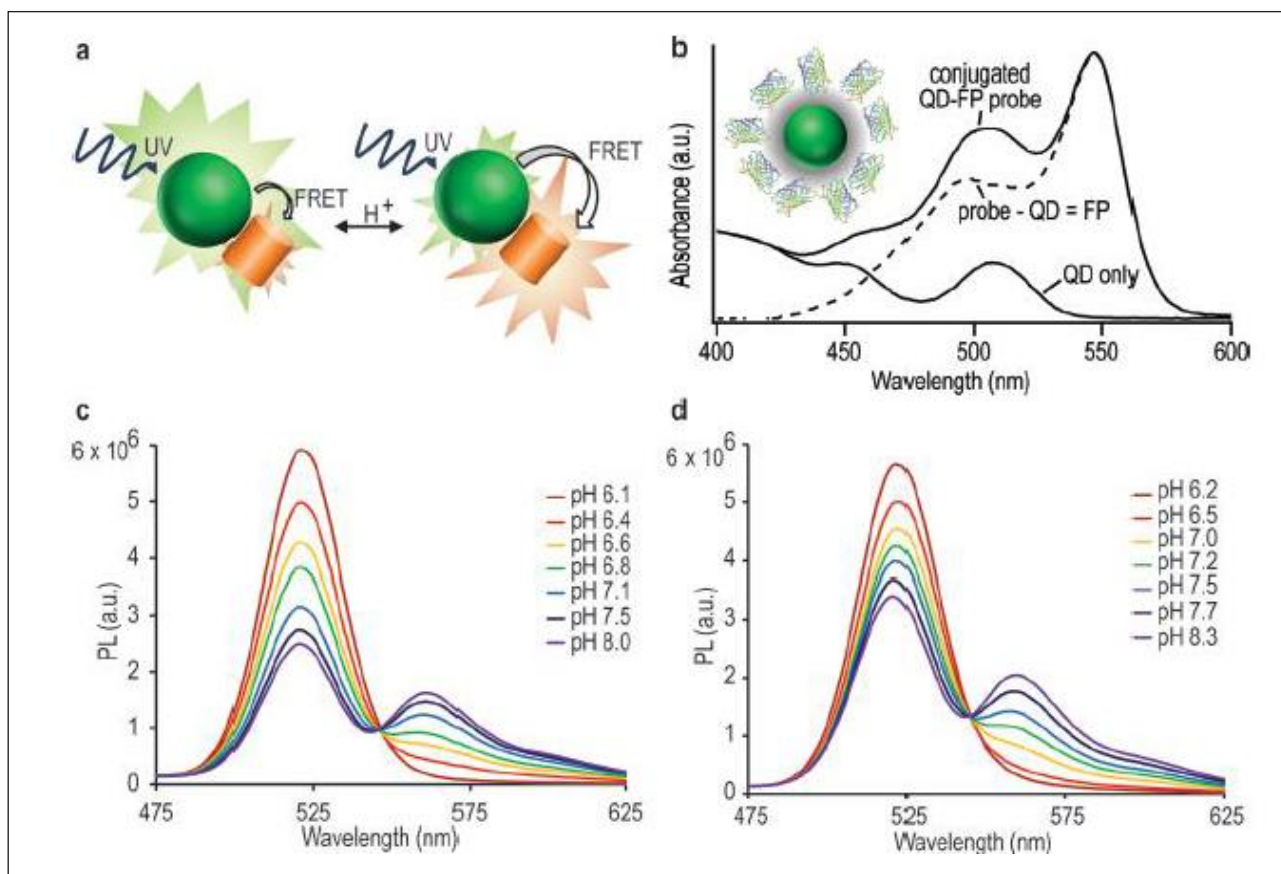
Figure 1 Schematic demonstration of the pH-dependent energy transfer between the quantum dot and fluorescent protein (FP). (b) Absorbance spectroscopy indicates multiple proteins bound to each QD, as depicted in the inset. (c and d) Titration of QD-FP probes containing the FP acceptors mOrange and mOrange M163K, respectively, showing increased energy transfer at alkaline pHs with clear isosbestic points. (ACS Nano, 2012, 6, 2917).

to either under- or overestimation of an analyte-specific signal. This is particularly relevant in the case of ligand-binding assays, where the number and conformation of ligand-specific proteins present at the surface of a quantum dot are critical to accurate determination of ligand potency.

Compared with conventional fluorophores, quantum dots are characterized by larger size, which enables multivalency and may be useful in ex vivo sensing applications. One often-used strategy employed for designing QD nanosensors is based on Förster resonance energy transfer (FRET) with the QDs. Under certain excitation, the emitted energy form a donor fluorophore is absorbed by an acceptor molecule which is present in the closer proximity resulting in the FRET phenomenon. distance between the donor

and accepter molecule which is typically less than 10 nm. QDs are highly fluorescent species with good photostability and brightness and act as perfect fluorescent donor and the target analyte may induce the occurrence of energy transfer. To date, quantum dots have been predominantly utilized as donor molecules in FRET-based sensing assays. Their use as FRET acceptors has been limited by two key properties. First, although their broad absorption profile presents a distinct advantage in multiplexed experiments, it results in unavoidable direct excitation. Second, it has been reported that the lifetime of the acceptor relative to that of the donor is critical to efficient FRET. Quantum dots have a longer excited-state lifetime compared to that of organic dyes, and it has been shown that FRET is virtually absent in dye-quantum dot D-A pairs even at favorable
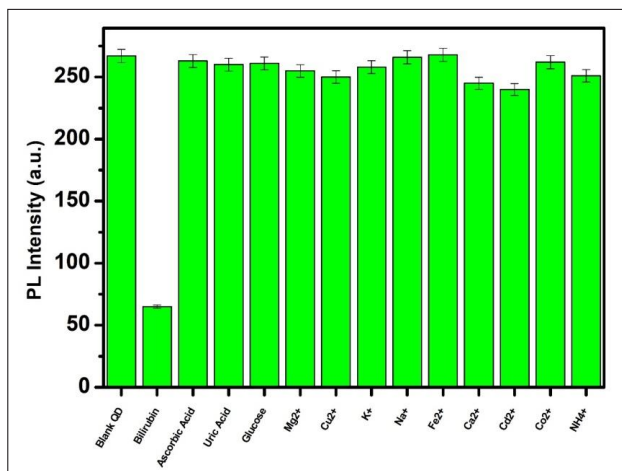
Figure 2 Specificity of binding of bilirubin with BSA-CdSe QDs in the presence of other possible coexistent substances (ACS Appl. Bio Mater. 2020, 3, 12, 882)

separation distances. Further, their relatively large size becomes a significant concern for in vivo sensing applications and FRET. The final size of a water-soluble, functionalized quantum dot poses a serious limitation, often exceeding the donor-acceptor distance required for efficient FRET. Nevertheless, as a result of their high quantum yield, superior physicochemical stability, and size-tunable, narrow photoluminescence spectra, quantum dots have been used in a number of FRET-based sensors, predominantly as a donor molecule. To illustrate, the following figure presents quantum dot fluorescent protein FRET probes for sensing of intracellular pH (Figure 1).

Besides, FRET operated processes, luminescence quenching analysis has also been exploited in a number of applications for biological sensing. Very recently, bovine serum albumin (BSA) encapsulated quantum dots has shown great promise where it was demonstrated that a strong affinity of BSA toward bilirubin resulting in luminescence quenching of the quantum dots can be fruitfully utilized in determining selectively free bilirubin, a key biomarker of jaundice, in submicromolar level in human blood samples (Figure 2).

The use of nanoparticle-based platforms for biosensing has introduced another powerful tool to array-based chemical sensing. The QDs based sensor arrays are increasingly developed for the pattern identification of multiple analytes. For instance, exciton energy transfer-based fluorescence sensing array has been developed for the discrimination of different nucleobases through target nucleobase-triggered self-assembly of quantum dots (QDs) (Figure 3).

As mentioned earlier, in recent time GQDs have got tremendous attention as an alternative to semiconductor QDs for use as biosensor because of excellent optical properties and more importantly biocompatibility. GQDs have shown great promise in detection of biomolecules, ions, and other compounds with high selectivity and sensitivity. The high quantum yield and tunable fluorescence of GQDs are advantages for sensing. A few typical recent developments are being highlighted to illustrate the approaches undertaken to explore the possibilities of use of GQDs as effective biosensors. Amine functionalized GQDs based fluorescent biosensor was developed for the detection of lung cancer cell biomarker *via* fluorescence 'turn on' mechanism, as represented in Figure 4a. FRET based system can effectively identify complementary and mismatched nucleic acid sequences with high sensitivity and good reproducibility. The system can be applied also for *in vivo* and in vitro imaging, and promote the application of carbon-based nanomaterials in immunoassays. Similarly, GQDs can be used as luminescence probe for the DNA methylation detection and MTase activity by fluorescence anisotropy. In this case, DNA probe was connected with the GQDs through end that contains CCGG sequence. The quenching of fluorescent intensity of GQDs was observed due to the interaction of GQDs to DNA strands. However, florescence intensity was found to be enhanced when HpII cleaved DNA strands due to insufficient M.SssI enzyme. An important approach was to design GQDs-aptamer-cDNA bioconjugates for the detection of ochratoxin A (OTA). The detection strategy uses the advantage of structure switching signaling of aptamer on combining with GQDs. Quenching mechanism
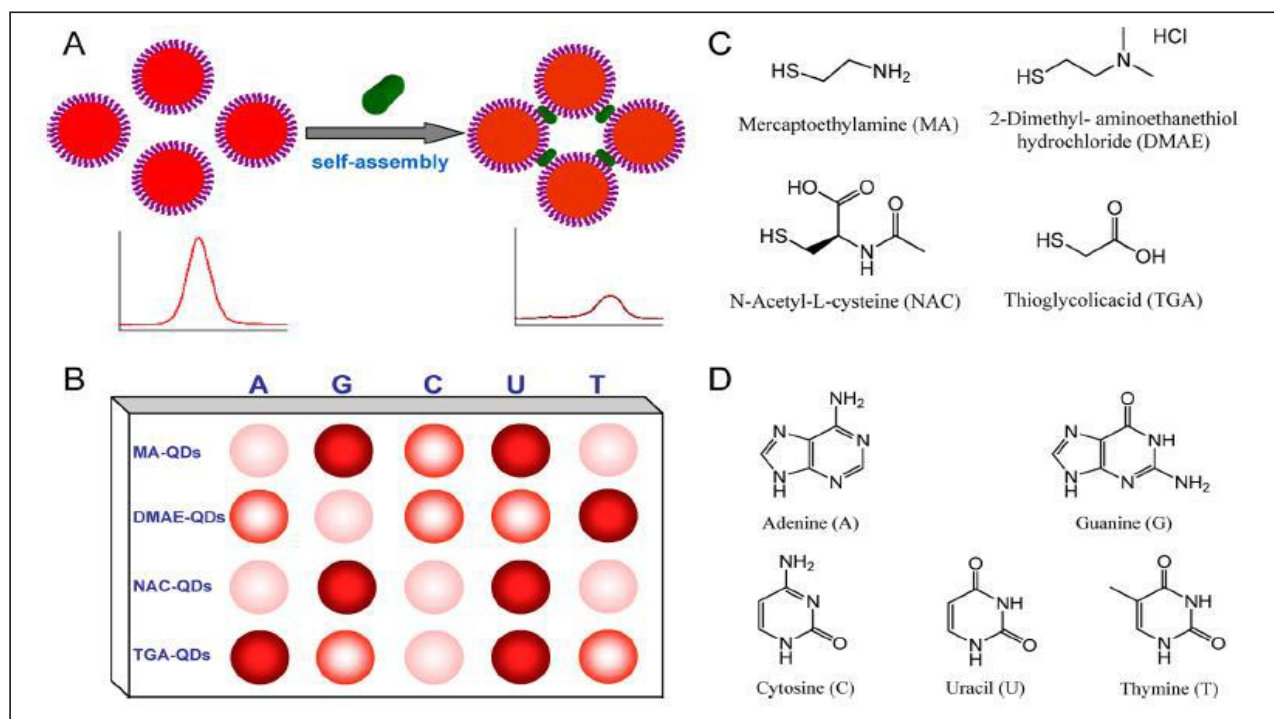
Figure 3 Schematic presentation of the exciton energy transfer-based QD fluorescence sensing array for discrimination of nucleobases. (A) Target-guided self-assembly of QDs results in the exciton energy transfer between assembled QDs, which is accompanied by a fluorescence quenching. (B) Fluorescence pattern generation through distinct assembly behavior and the exciton energy transfer effect. The wells on the microplate contain functionalized QDs with different ligands, and the addition of nucleobase analytes produces a fingerprint for a given nucleobase. (C) Chemical structure of the acceptor ligands on the surface of QDs. The terminal mercapto group coordinates with QDs, and the other terminal group determines the QDs with different features. (D) Chemical structure of the five nucleobase analytes (Anal. Chem., 2015, 87, 876)

based on aggregation and disaggregation of GQDs in the presence of DNA aptamer has been presented on Figure 4b. The fluorescence signal-on based platform can detect OTA with high selectivity and sensitivity. A detection limit of 13 pg/mL was observed with 95-103% recovery in red wine samples. Recently, sensing of lysine was shown using GQDs. Lysine was adsorbed on the GQDs surface *via* electrostatic interactions, which triggered fluorescence enhancement at 420 nm. Because of having a small diameter, lysine approaches GQDs easily, which is responsible for the change in emission of GQDs. Further, it is seen that N-GQDs and nitrogen and sulfur co-doped GQDs(N,S-GQDs) show higher sensitivity than GQDs. Detection of cancer cell was shown through folate bioreceptor functionalized N-GQDs. A comparison was made to check the specificity of the folate decorated Nitrogen-doped

GQDs (FA-N-GQDs) nanocomposite towards the detection of MKN 45 with HEK 293 as a normal cell. A minimum amount of attachment was observed when GQDs were allowed to make contact with MKN 45. The targeting ability of GQDs toward the cancer cells was confirmed by these measurements.

Curcumin-GQDs based dual-mode biosensor was developed for sensitive detection of APOe4, responsible for Alzheimer's disease. They utilized the fluorescence and electrochemical properties of curcumin electropolymerized on GQDs-ITO (Indium-Tin-Oxide) surface. The dual-mode sensing platform exhibited good reproducibility, sensitivity, and selectivity. The limit of detection (LOD) of the sensor was found to be 0.48 pg.mL^{-1}. GQDs-enzyme based biosensor was reported for the determination of hydrogen peroxide and
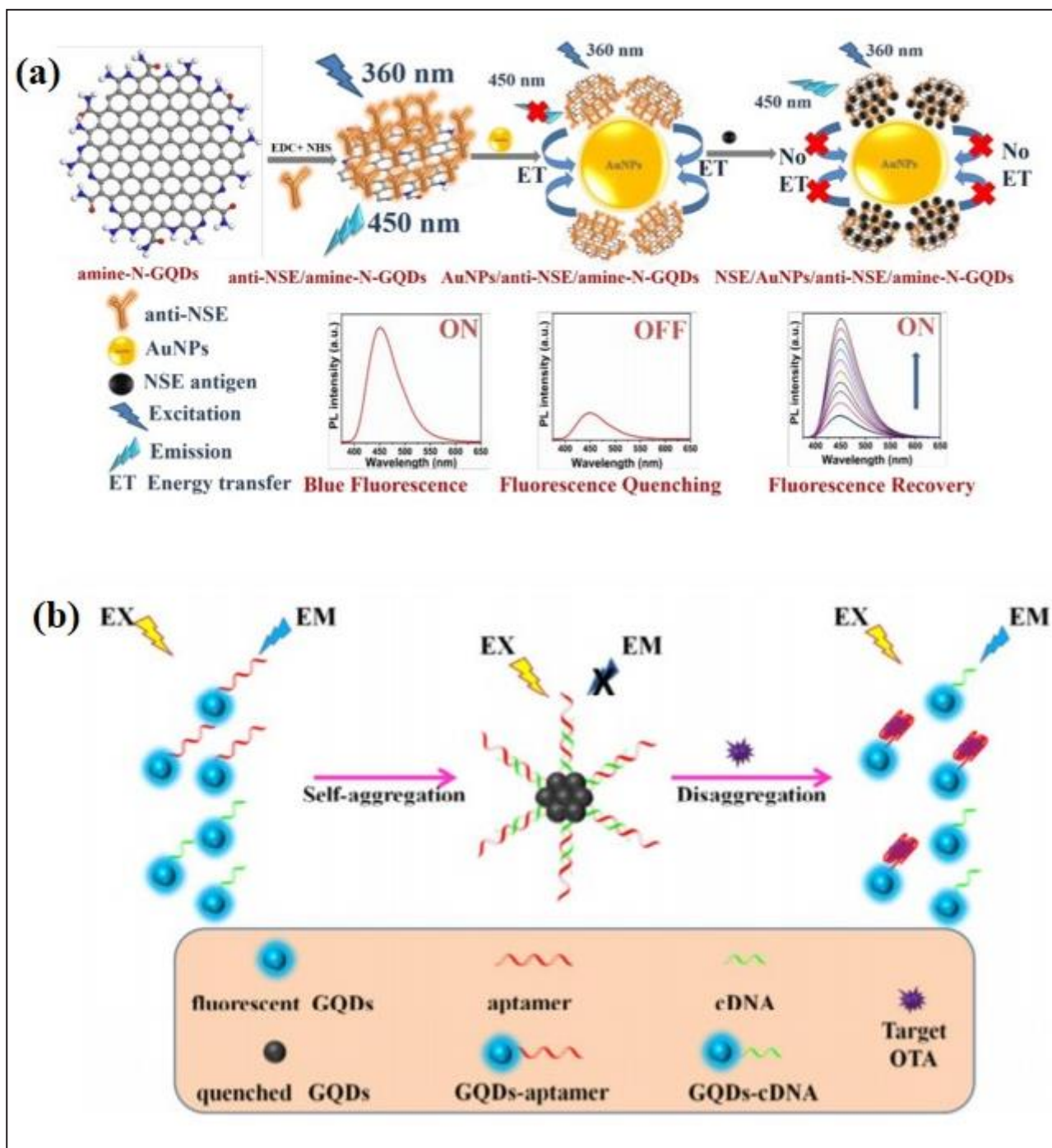
Figure 4 (a) Schematic representation of mechanism of FRET based sensing of small cell lung cancer detection. (b) Schematic diagram on aggregation state change of GQDs-aptamer based fluorescent signal-on based platform for the detection of OTA. (ACS Appl. Bio Mater. 2020, 3, 4922; Anal. Chem. 2017, 89, 1704)

glucose. Hydrogen peroxide was formed by the oxidation of glucose using glucose oxidase (GOx). The hydrogen peroxide produced was later allowed to oxidize phenol to quinone. Due to oxidation of phenol by hydrogen peroxide, the fluorescence of GQDs–GOx–HRP–phenol system (HRP stands for horse radish peroxidise) was quenched. Limit of detection for glucose was as low as 0.08 µ mol/L.

Attempts are made to compare to the detection efficiency of SQDs and GQDs. An estimate was shown as considering only the photophysical properties of the quantum dots, the signal that can be obtained with SQDs may about 7 times larger on using GQDs at the same concentration. However, this estimate is not so definitive as extinction coefficient of GQDs is taken to be same as that for the SQD sample since the extinction coefficients of GQDs are not well reported,

3. Concluding remarks

Quantum dots will become, and one can argue they already are, and indispensable tool for biological research. Quantum dots will see increasing use to elucidate the molecular mechanisms of protein binding, signaling, and regulation. They will be used to establish molecular mechanisms of disease and at the same time become a tool for drug discovery to treat disease. In the future we may also see further incorporation of quantum dots as cell reporters of biological function, implementation as tools for interrogating tissue, and forming the basis of novel biochemical assays. The varieties of commercially available quantum dots for the research community will continue to grow and dual-functional nanoparticles will become available, such as particles that can be used for dual imaging modalites. We believe that the future of quantum dots in biology is as bright as the quantum dots themselves.

Because of unique properties, GQDs find applications in emerging biomedical, optical and energy related areas. GQDs synthesized through different approaches like top-down and bottom-up have some advantages and drawbacks. Microwave-assisted synthesis is simple and one of the fastest methods. The acidic exfoliation methods used been extensively employed for the synthesis of good quality GQDs, although the methods are cumbersome and time-consuming. Thus, the synthesizing of GQDs with acid exfoliation method with a simple procedure is still challenging and needs to be explored. Purification of GQDs may be done shortly by utilizing size-selective precipitation method instead of dialyzing for days. GQDs can easily get functionalized with functional groups by using different techniques. The synthetic procedure may be chosen based on applications. The applications of GQDs are diverse. In very recent years, GQDs with various edge functionalization have been gaining tremendous prospects in the field of drug delivery, bioimaging, and biosensing due to their small size, high fluorescence, and low toxicity. Excellent loading capacity of GQDs is a key advantage in drug delivery.

However, some of the properties of GQDs and mechanism of interactions with different biological systems require more investigation for greater understanding of the functional aspects. Reports on red-emitting GQDs are scarce. Red emitting GQDs can be of great significance in bioimaging applications because of the low absorption in tissues in the range. In the future, research needs to be carried out on developing more sensitive and selective biosensors based on the GQDs. *In-vivo* toxicity of GQDs are very low. Hence, more investigation on the toxicological aspects of GQDs for long term exposure will help understand its potential for biological applications.

Finally, despite substantial progress in nanocrystal surface chemistry and conjugation strategies, surface modification and functionalization remains the most important issue when utilizing quantum dots as a basis for biosensing applications. A single surface modification step may require several purification steps,

often resulting in unwanted aggregation and crosslinking. Nevertheless, quantum dots have come a long way since their introduction to the field and have a large potential in biosensing applications that still remains untapped.

References

1. Glowing Graphene Quantum Dots and Carbon Dots: Properties, Syntheses, and Biological Applications, Zheng, X. T.,Ananthanarayanan, A., Luo, K. Q., Chen, P. *Small* 11, 1620−1636. (2015)
2. Synthesis of Excitation Independent Highly Luminescent Graphene Quantum Dots through Perchloric Acid Oxidation, S. Maiti, S. Kundu, C. N. Roy, T. K. Das and A. Saha, *Langmuir* 33, 14634-14642 (2017).
3. Physicochemical Understanding of Protein-Bound Quantum Dot-Based Sensitive Probing of Bilirubin: Validation with Real Samples and Implications of Protein Conformation in Sensing, S. Karmakar, T. K. Das, S. Kundu, S. Maiti, and A. Saha, *ACS Applied Bio Materials*, 3, 8820-8829 (2020).
4. Graphene quantum dots from chemistry to applications P. Tian, L. Tang, K.S. Teng and S.P. Lau, Materials Today Chemistry 10, 221-258 (2018).
5. Semiconductor versus graphene quantum dots as fluorescent probes for cancer diagnosis and therapy applications, A. Rakovich and T. Rakovich, J. Mater. Chem. B, 6, 2690-2712 (2018)
6. Sensing with photoluminescent semiconductor quantum dots, M. Chern, J. C Kays, S. Bhuckory and A. M Dennis, *Methods Appl. Fluoresc.* **7**. 012005 (2019)
7. Quantum Dots for Sensing. In: Sensors Based on Nanostructured Materials, J. Goicoechea, F.J. Arregui, I.R. Matias Arregui F. (eds) Springer, Boston, MA (2009).
8. Recent Advances in Synthesis and Biological Applications of Graphene Quantum Dots, S. Karmakar, T. K. Das, S. Kundu, S. Maiti and A. Saha, J. Ind. Chem. Soc. 98, 100069 (2021) (special issue).

Dr. Abhijit Saha after completing M.Sc. degree from the University of Calcutta joined Post M.Sc. Associateship conducted by Saha Institute of Nuclear Physics, Kolkata where he worked for Ph.D. degree which was conferred by the University of Calcutta. After his post-doctoral research in Hebrew University, Israel, Dr. Saha joined UGC-DAE Consortium for Scientific Research as Scientist. In 2016, he assumed the position of Centre-Director of UGC-DAE CSR, Kolkata Centre. He has guided 14 Ph.D. students in addition to a good number of Masters' projects. He delivered more than 50 invited talks in national and international conferences. He has about 200 publications in well-known International Journals including 03 book articles. Dr. Saha received Scientific excellence award of UGC-DAE CSR, Indore. He was conferred certificate of award of Chair Professor in Nanoscience and Nanotechnology by Mahatma Gandhi University. He worked in the area of radiation chemical sciences which include ion beam modification of polymeric materials, radiation damage in biological systems. His current research interests are on development of synthesis approaches for bio-mimetic and size-tunable luminescent nanostructures for site-specific binding and cellular imaging and to study the interactions with different biomolecular systems to develop protocol for nanoparticle based sensors.

Ultrafast Dynamics of a Thiocyanate Probe in an Alcohol and an Alcohol-Based Deep Eutectic Solvent: A Comparative Study Using 2D IR Spectroscopy

Srijan Chatterjee[§,†], **Samadhan H. Deshmukh**[§,†,] , **Sayan Bagchi**[*,§,†]

[§]*Physical and Materials Chemistry Division, National Chemical Laboratory (CSIR-NCL),*
Dr.Homi Bhabha Road, Pune- 411008, (India)
[†]*Academy of Scientific and Innovative Research (AcSIR), Ghaziabad- 201002, India*

Abstract

Deep eutectic solvents, consisting of a hydrogen bond acceptor and a hydrogen bond donor are the novel green solvents with plethora of sustainable applications. Due to the low intrinsic viscosity, alcohol-based deep eutectic solvents find utility in several applications. Interestingly, alcohols can act as both hydrogen bond donors and acceptors. Therefore, it is essential to distinguish between the molecular level interactions and dynamics present in the alcohol-based DES and in the DES-constituent (alcohol).

In this work, we have performed two dimensional infrared spectroscopy on methyl thiocyanate dissolved in 1,2-ethanediol and in ethaline (1,2-ethanediol based deep eutectic solvent). Our results show that the solvation dynamics slows down almost threefold in ethaline when compared to than in the alcohol. In addition, although the nitrile stretch shows a similar peak-width in the IR absorption spectra, the alcohol spectrum had a larger contribution from homogeneous broadening. The intrinsic larger inhomogeneity in the deep eutectic solvent arises from increased configurational heterogeneity due to hydrogen bonding between the two components, 1,2-ethanediol and choline chloride.

1. Introduction

In the last few decades, deep eutectic solvents (DES) have emerged as a promising green alternative to conventional solvents due to their various favorable properties, such as biodegradability, low vapor pressure, high conductivity, and recyclability.[1,2] These favorable properties of the DES have been utilized in various fields of chemistry, including carbon dioxide capture, electrochemistry, organic catalysis, and bio-extraction. Although different types of DES has been synthesized since the seminal work of Abbott and co-workers ,[3] the most popular candidate consists of a quaternary ammonium salt (e.g., choline chloride, CHCl) as a hydrogen bond donor (HBD) and different hydrogen bond acceptors (HBA) like amides, carboxylic acids, and alcohols. THE HBA and HBD are mixed in a certain mole ratio to prepare the DES. The choice of the HBA and the variation in molar ratios can provide tenability of the DES properties. DES shows a significant depression in melting point from that of its constituents. The decrease in the melting point happens due to the interspecies hydrogen bonding (H-bonding) between the HBA and the HBD.

What makes DES more desirable is that not only it has a significantly lower melting point than either of its constituents, but it is also a liquid at room temperature. However, the widespread use of DES is limited by its high viscosity. Among different DES, alcohol-based DES have lower viscosity among the others. Analysis of hydrocarbon chain length dependence on the viscosity of the alcohol-based DES has shown that the viscosity decreases with the decrease in the chain length. A combined theoretical and experimental study using molecular dynamics

simulations and two dimensional infrared (2D IR) spectroscopy connected the viscosities of the DES to the corresponding timescales of solvation dynamics.[4] Interestingly, similar to the interspecies H-bonding in DES, alcohols themselves are known to form extended structures due to interspecies H-bonding as they can be both HBA and HBD. Although most previous studies provided an excellent analysis of the DES characteristics,[5-7] decoupling the contribution of alcohol in the final DES property is essential to obtain a molecular understanding of the DES.

In this work, we have utilized the nitrile stretch of methyl thiocyanate (MeSCN) dissolved in 1,2-ethanediol (ED) and 1,2-ethanediol-based DES (ethaline) to understand the subtle differences in the solvation dynamics using 2D IR spectroscopy.

2. Materials and Method

MeSCN, ChCl, 1,2ethanediol of highest available purity are purchased from the Sigma-Aldrich. Ethaline DES are made according to the previous published procedure.[7]

The IR absorption spectra are recorded in on a Bruker Vertex 70 FTIR spectrometer with a 2 cm^{-1} resolution at room temperature. For each sample, ~100 µL of the sample solution is loaded into a demountable cell (PIKE Technologies) consisting of two windows (CaF2, 3 mm) thickness, Shenzen Laser) separated by a mylar spacer of 100 µm thickness.

The 2D IR and pump-probe spectra were collected by using a pulse shaper-based 2D IR spectrometer developed by PhaseTech Spectroscopy, Inc., USA. A detailed description of the setup used for this work has been described elsewhere.[4] In a nutshell, IR pulses, are generated with approximately ~60 fs pulse width. The pulses are then split into a strong pump beam and a weak probe beam. A germanium acoustic-optic modulator (AOM) based pulse shaper is used to generate two pump pulses with a delay interval of (τ). The pump and probe pulses are spatially and temporarily overlapped and focused at the
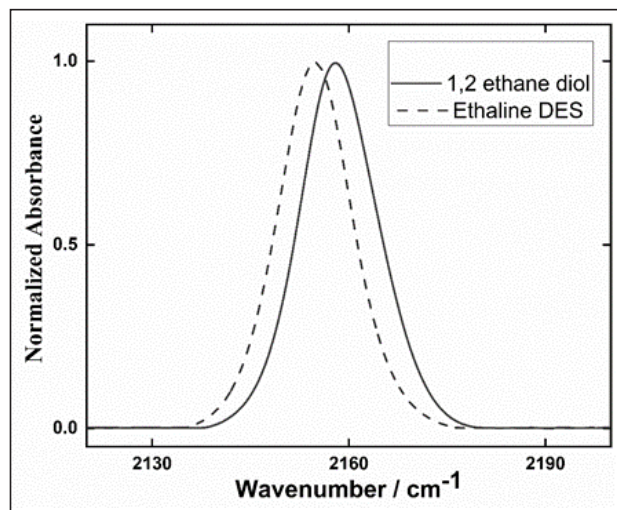

Fig 1: IR absorption spectra of MeSCN in ethaline DES and 1,2-ethane diol.

sample. 2D IR spectra are acquired by changing the delay (Tw) between the pump and the probe pulses. The signal is collected using a monochromator and detected on a nitrogen- S6 cooled 64 pixel HgCdTe (MCT) IR array detector. Final 2D IR spectra are constructed by Fourier transforming the experimental data along the τ axis.

3. Results and Discussion

IR absorption spectra of the nitrile stretch of MeSCN in ED shows a peak at 2158 cm^{-1} with a full width at half maximum (FWHM) of ~13.5 cm^{-1}. In ethaline, the nitrile peak is centred at 2155 cm^{-1} with a FWHM of ~13.8 cm^{-1}. Interestingly, although the nitrile stretch is ~ 3 cm^{-1} blue-shifted in ED to that in ethaline, the FWHM of the peaks are the same within the experimental error. The blue-shift of the nitrile peak in ED indicates the presence of extensive H-bonding between MeSCN nitrogen and the hydroxyl groups. However, the extent of H-bonding of the thiocyanate nitrogen is plausibly less in ethaline, resulting in a 3 cm^{-1} red-shift. This is further corroborated by the fact that the previous study on molecular and ionic probe in ethaline reported a neligible hydrogen bonding population.[4,8]

Although there is a difference in the extent of H-bonding, it is interesting to note that the nitrile
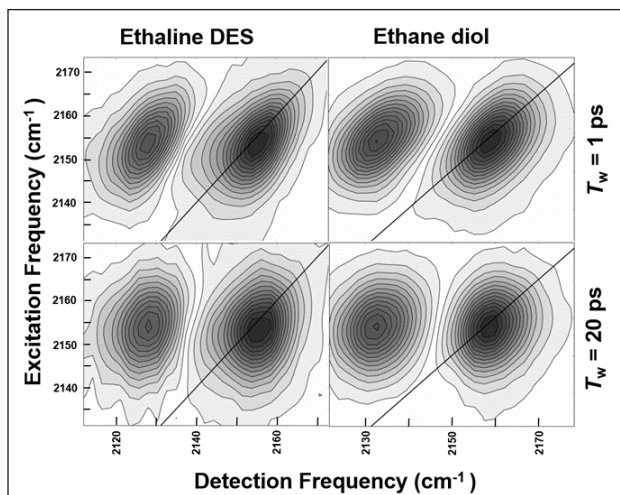
Fig 1: 2D IR spectra of MeSCN in ethaline DES and 1,2 ethane diol at two different values of T_w (1 ps and 20 ps)

stretch of MeSCN shows a similar lineshape in both the IR absorption spectra. Moreover, the time-averaged absorption spectra cannot report on any difference in the solvation dynamics between the two solvent systems. We have performed 2D IR experiment at different waiting times to obtain a better understanding of the microenvironment near the nitrile probe and to quantify the solvation dynamics timescales.

A 2D IR spectrum spreads the frequency information in two axes (excitation and detection axes) and in turn deciphers the different sub-ensembles hidden in the broad IR absorption spectrum. Three ultrafast femtosecond (fs) pulses are focused at the sample in 2D IR spectroscopy at different time-delays. The delay between the second and the third pulse, known as waiting time (T_w), is scanned from few fs to tens of picosecond (ps) to obtain the dynamic information. The correlation between the excitation frequency (caused by the first pulse excitation) and the detection frequency (caused by the third pulse interaction) decreases with increasing waiting time due to spectral diffusion. For this reason, early waiting time 2D IR spectra are highly correlated and are therefore diagonally elongated. The correlation is gradually lost as T_w increases and the spectra become increasingly upright. The loss in correlation in directly related to the solvent fluctuation timescale, i.e. a faster

loss in correlation denotes faster fluctuations. Thus, a careful analysis of the change in 2D spectral lineshapes of MeSCN in ethaline and ED would allow us to decipher the inherent difference in dynamics of the DES system from one of its constituents.

Fig. 2 shows 2DIR spectra of the ethaline DES and 1, 2 ethanediol at a short (1ps) and a long (20 ps) waiting time. Each spectrum contains a peak-pair corresponding to v=0→v=1 transition (peak at the right side) along the diagonal (line shown in Fig.2) and the v=1→v=2 transition (peak at the left side) shifted by the anharmonicity of the nitrile vibrational stretch along the detection axis. Spectral diffusion in ethaline is quite slow compared to that in ED, which results in a more diagonally elongated spectrum at 20 ps in the DES. Slowdown of dynamics in DES compared to that in alcohol can be rationalised by considering the higher viscosity of the DES. However the important question remains: how much of the DES dynamics comes from the alcohol constituent. To get a quantitative picture of the dynamical difference in both of the systems we have implemented central line slope method (CLS).[9] CLS analysis effectively constructs a frequency frequency correlation function (FFCF) which is fitted to multi-exponentials (see equation below) to obtain the timescales of the solvent fluctuation.

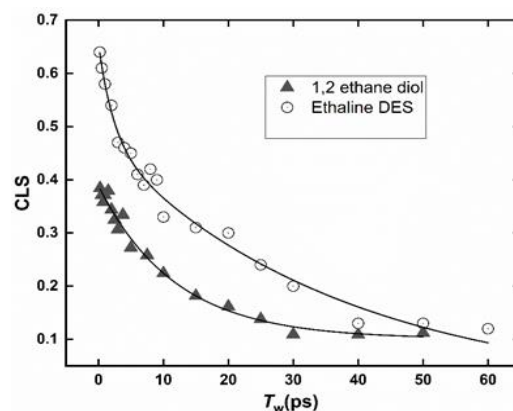$$C(t) = \sum_i a_i e^{-t/\tau_i}$$

Figure 3: T_w dependent CLS of ethaline DES and 1,2 ethane diol. Black curves are the exponential fit. Initial drop from 1 at T_w = 0 indicates the homogenous contribution.

Interestingly the CLS decay starts from a higher value for the DES (~0.65) than the alcohol (~0.4). If only inhomogeneous dynamics between the second and the third pulse have contributed to the CLS decay, the value at T_w would have been unity. The drop in the CLS value at the early waiting time form unity signifies the homogenous contribution to the line shape of the IR peak.

The CLS decay curves shown in Fig.3 are fitted with a bi-exponential decay function for DES. The fit provides a short time component of ~2 ps and a long time component of ~37 ps. The CLS decay in ED is fitted with a single exponential decay function of timescale ~11 ps. The long component of the bi-exponential CLS decay is known to be sensitive for the bulk dynamics of the DES and previously shown to be directly related to the hydrocarbon chain length of the alcohol of the DES.[4,10] The timescale of long component in pure DES (~37 ps) is higher compared to that in its individual constituent (~11ps). Although the viscosity of ethaline is approximately double than that of ED, it is important to note that a larger effect slowdown in solvation dynamics (>3 times) is observed. This result is somewhat counterintuitive to the previous finding that the long timescale of the DES dynamics scales linearly with the viscosity of the DES for alcohols of different chain length.[4,9] As it is well known that the alcohols forms all kind of H-bonded polymeric structure, the pertinent question will be how much of those polymeric structures persist in the DES. It is quite evident form the timescale obtained from the 2D IR that introduction of the choline chloride perturbs the alcohol arrangement significantly to cause approximately a near three fold decrease in the long timescale.

In addition, the initial CLS values in ethaline (~0.65) and in ED (~0.4) indicate a larger inhomogeneity in the DES. Although, alcohols form heterogeneous polymeric structures through an extended H-bonded network, addition of choline chloride increases the configurational heterogeneity of the solvent, as reflected by the intial CLS values. Although, both homogeneous and inhomogeneous line broadening mechanisms contribute to the lineshapes of the IR absorption spectra in ED and in ethaline, the extent of these contributions could not be estimated from the similar FWHM. 2D IR allows us to dissect these contributions and brings out the subtle changes in the molecular arrangements of the solvent systems.

4. Conclusion

In this study, we have performed 2D IR spectroscopy on MeSCN dissolved in ethaline and in ED to estimate the solvation dynamics timescales in a DES and in one of the DES constituents. Our results demonstrate that the solvent fluctuations are slower in alcohol-based DES than in the pure alcohol. We have also observed that the relative slowdown the fluctuation dymamics is larger than the increase in relative viscosity of the two solvent systems. In the future, comparison of solvation dynamics using different chain length of alcohols and the corresponding DES dynamics will be an interesting addition to understanding the fundamental question behind the formation of the DES.

References

1. Smith, E. L.; Abbott, A. P.; Ryder, K. S. Deep Eutectic Solvents (DESs) and Their Applications. *Chem. Rev.* **2014**, *114*, 11060-11082.
2. Wagle, D. V.; Zhao, H.; Baker, G. A. Deep eutectic solvents: sustainable media for nanoscale and functional materials. *Acc. Chem. Res.* **2014**, *47*, 2299-2308.
3. Abbott, A. P.; Capper, G.; Davies, D. L.; Rasheed, R. K.; Tambyrajah, V. Novel solvent properties of choline chloride/urea mixtures. Chem. Commun. 2003, 70−71.
4. Chatterjee, S; Ghosh, D; Haldar, T; Deb, P; Sakpal, S.S.; Deshmukh, S.H.; Kashid, S.M.; Bagchi, S. Hydrocarbon Chain-Length Dependence of Solvation Dynamics in Alcohol-Based Deep Eutectic Solvents: A Two-Dimensional Infrared Spectroscopic Investigation. J. Phys. Chem. B, 2019, 213, 9355-9363.
5. Hammond, O. S.; Bowron, D. T.; Edler, K. J., The Effect of Water upon Deep Eutectic Solvent Nanostructure: An Unusual Transition from Ionic Mixture to Aqueous Solution. *Angew. Chem., Int. Ed.* **2017,** *56*, 9782-9785.
6. Kumari, P.; Shobhna; Kaur, S.; Kashyap, H. K. Influence of Hydration on the Structure of Reline Deep Eutectic Solvent: A Molecular Dynamics Study. *ACS Omega* **2018**, *3*, 15246-15255.

7. Harris, R. C. Physical properties of alcohol based deep eutectic solvents; University of Leicester, 2008.

8. Cui, Y.; Fulfer, K. D.; Ma, J.; Weldeghiorghis, T. K.; Kuroda, D. G. Solvation dynamics of an ionic probe in choline chloride-based deep eutectic solvents. Phys. Chem. Chem. Phys. 2016, 18, 31471− 31479.

9. Kwak, K.; Park, S.; Finkelstein, I. J.; Fayer, M. D. Frequency-frequency correlation functions and apodization in two-dimensional infrared vibrational echo spectroscopy: a new approach. *J. Chem. Phys.* **2007**, *127*, 124503-124517.

10. Hossain, S. S.; Samanta, A. How do the hydrocarbon chain length and hydroxyl group position influence the solute dynamics in alcohol-based deep eutectic solvents? Phys. Chem. Chem. Phys. 2018, 20, 24613−24622.
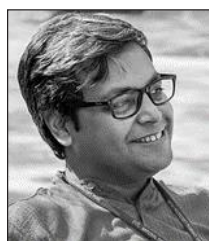
Dr. Sayan Bagchi is a Principal Scientist in Physical and Materials Chemistry Division, CSIR-NCL, Pune Dr. Bagchi completed his BSc. from Presidency College, Kolkata (2000) and MSc. from IIT Kanpur (2002). He received the PhD degree from University of Pennsylvania (USA), in 2008. After the completion of PhD, Dr. Bagchi joined Stanford University as a post-doctoral researcher. Dr. Bagchi joined National Chemical Laboratory (NCL), Pune in 2012 as a Senior Scientist.

Dr. Bagchi's research interest includes obtaining spectroscopic insights about complex scientific problems in the field of chemistry, biology, and materials science. He is interested in the molecular structure-function relation which is governed by both interactions and dynamics. He uses the concept of vibrational Stark spectroscopy to obtain the interaction picture. He has set-up the two-dimensional infrared (2D IR) spectrometer to decipher the timescales of the ultrafast dynamics happening in femtoseconds to picoseconds timescale. In addition to experiments, he performs computations (both ab- initio and molecular dynamics) to obtain a molecular understanding of the different chemical processes.

Srijan Chatterjee did his bachelor study form Ramakrishna Mission Residential College Narendrapur, Kolkata in 2015 and his masters in chemical science form Indian Association for the cultivation of Science in 2017.After that he joined physical and material chemistry department of CSIR National Chemical laboratory Pune under the supervision of Dr Sayan Bagchi. He is currently working on various condensed matter system such as deep eutectic solvents to understand the underlying dynamics using both 2DIR spectroscopy and classical molecular dynamics simulation.

Samadhan H Deshmukh was born in Maharashtra, in 1992. After completing his B.Sc. from Punyashlok Ahilyadevi Holkar Solapur University and M.Sc. in Chemistry from the Shivaji University, Kolhapur he joined for his doctoral studies in 2018 under the supervision of Dr. Sayan Bagchi at the Physical and materials Chemistry, CSIR National chemical laboratory Pune, where he is currently pursuing his research work on synthesis and surface characterisation of quantum dots using ultrafast 2D IR spectroscopy and computational methodology.

Laser Induced Tuning in Linear and Nonlinear Optical Properties of Triangular Shaped Ag Nanostructures

Pathik Kumbhakar*, Koushik Mondal, Subrata Biswas and Ashim Pramanik
Nanoscience Laboratory, Dept. of Physics, National Institute of Technology Durgapur, 713209, West Bengal, India
*E-mail: pathik.kumbhakar@phy.nitdgp.ac.in

Abstract

The development of laser is one of the important milestones in the human civilization and laser radiations are now extensively utilized in the advancement of the sciences, technology and society. Also, in the last a few decade laser sources are used extensively in the field of nanotechnology for the development and determinations of optical properties of nanostructured materials. Recently, in our group we have also reported some works in this direction and a summary is presented here. The tuning of the Plasmon Resonance band (PLB) within a wide wavelength range of 400-540 nm has been achieved by *ns* pulse Nd:YAG laser induced reshaping of the chemically synthesized triangular shaped Ag nanoparticles (Tr-Ag-NPs). The used Tr-Ag-NPs after coating of Au layers are found to exhibit interesting nonlinear optical (NLO) properties, as determined by *fs* Z-scan technique. Additionally, Tr-Ag-NPs are further employed in demonstration of random lasing with a low lasing threshold.

1. Introduction

Since the emergence of the working laser from the realm of the Science fiction movies in the late 1950's, where it was shown as a weapon, the laser has found its way into a wide range of applications [1]. Laser finds applications in the medical field, in auto mobile industry, in the defense sector as well as in the field of nanotechnology [1-3]. The widespread use of Plasmonic nanoparticles (NPs) from the medical to defense sectors requires a thorough exploration of their linear and nonlinear optical (NLO) properties. Laser radiations can be used to determine various optical properties of NPs as well as it is possible to tune the linear and NLO properties of NPs [3]. However, the tuning of the Plasmon Resonance band (PLB) of Ag NPs from 540 to 400 nm by its reshaping is demonstrated through the photochemical interaction of Ag NPs with ns laser pulses. The multiphoton absorption properties and other NLO parameters of the triangular shaped Ag NPs with Au coating are also successfully quantified by performing the Z-scan experiment under a pump wavelength of 532 nm and having pulsed duration of 100 fs. On the other hand, in the recent past a lot of research activities are being carried out in the development of random lasers (RLs) by using nanostructured materials as scatterer [1, 4, 5]. Unlike the conventional lasers, in RLs optical feedback is provided by the scatterers. It has been predicted earlier that the phenomenon of random lasing is analogous to a nuclear reactor and can be achieved through stimulated emission in disorder-induced light scattering [1, 5]. It has been found that the synthesized Tr-Ag NPs may play an important role in the development of visible random laser light emission with a relatively low lasing threshold. However, a summary of some of our recent reports [2-4] are presented here.

2. Experimental details

The Tr-Ag-NPs are synthesized by using hydrothermal procedure and then *ns* laser induced reshaping is carried out to tune its PLB as demonstrated recently by our group [2]. Briefly, the as-synthesized Tr-Ag-NPs ($N_{Ag} \approx 10^{14}$ nos./

ml) are exposed to the 1064 nm i.e. Nd:YAG laser fundamental radiation having pulsed duration of 10 *ns* and 10 Hz repetition rate. The exposure time of laser has been varied but with a fixed laser fluence (F_{in}). The morphological and optical properties of the Tr-Ag-NPs, before and after exposing to the laser have been investigated using different characterization techniques. Also, we have utilized the Plasmonic property of the Tr-Ag-NPs for generation of random laser (RL) emission at NIR region under CW pumping condition in which Hibiscus rosa-sinensis leave (HRL) extract has been used as gain medium. The aqueous mixture of HRL extract and Tr-Ag-NPs is pumped with a 632.8 nm CW laser and the generated emission spectra is collected by using a photo detector (Avaspec-2048), placed at an angle of 60° w. r. t the direction of incidence of the pump beam [4]. The Tr-Ag-NPs have been further chemically wrapped with Au layer of thickness 3 nm, and the NLO properties [3] of the synthesized Au coated Tr-Ag-NPs (Tr-Ag-NPs@Au) has been investigated by Z-scan technique at 532 nm with 100 *fs* pulsed laser radiation.

3. Results and discussion

3.1. Effect of *ns* pulsed laser radiation on the shape and surface plasmon resonance band of Tr-Ag-NPs

It has been found that reshaping of nanoparticles is possible by exposing those materials in the high power pulsed laser radiation of appropriate wavelength, fluence and laser ablation time duration. Recently, we have demonstrated reshaping of chemically synthesized triangular shaped Ag nanoparticles (Tr-Ag-NPs) through laser ablation in liquid (LAL) technique [2]. The Tr-Ag-NPs are exposed to 1064 nm Q-switched Nd:YAG laser radiation for various time durations but the fluence of the incident laser radiation is kept fixed at 104 J/cm^2 [2]. To find the effect on the linear optical absorption properties of Tr-Ag-NPs the UV-Vis. absorption spectra of the Tr-Ag-NPs before and after *ns* pulsed laser irradiations are measured

at room temperature and the summary of the obtained results are shown in Fig. 1 (a).

Figure 1 shows that the PLB of Tr-Ag-NPs (0 min) is located at 538 nm [2]. And after the samples are exposed to the *ns* pulsed laser radiation, the PLB is blue shifted due to the truncation of its sharp corners (as can be found from the TEM images of the samples shown in Fig. 1(b)). From Fig. 1(a) it can be observed that after 40 min of exposer the PLB is shifted to 489 nm. Also after 40-60 min of laser exposure the
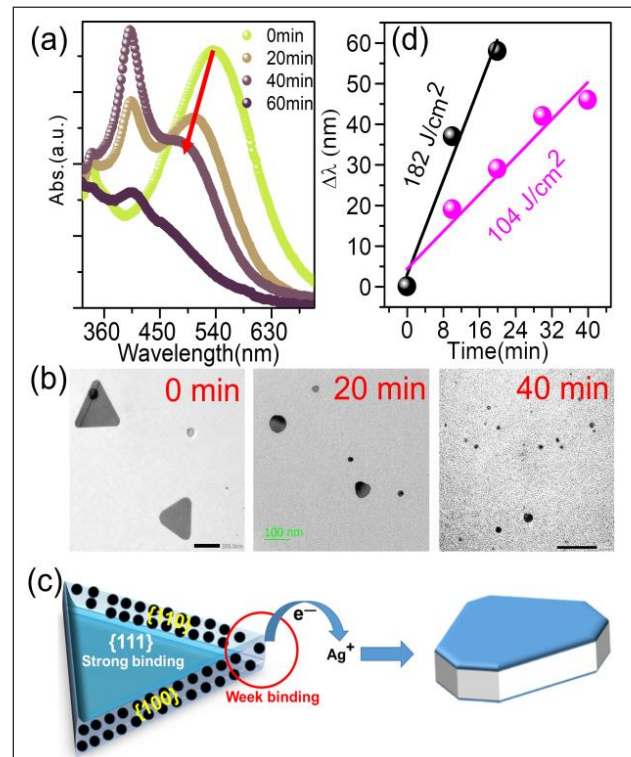

Fig 1: (a) UV-Vis. absorption spectra of Tr-Ag-NPs before and after laser exposer. (b) TEM images of Tr-Ag-NPs before and after laser exposer. (c) Schematic of laser induced reshaping mechanism. (d) The shift in the PLB position (Δλ) w.r.t. that of as-synthesized Tr-Ag-NPs (i.e. 0 min sample) is plotted against the exposer time (Adapted from the ref. no. 2).

shape of the NPs has become near spherical type [2].

The reshaping of the Tr-Ag-NPs has been confirmed from the typical TEM images, presented in Fig. 1 (b). The reason behind such laser induced reshaping is described below briefly [2]. At the top and in the bottom, the flat

faces of Tr-Ag-NPs are consisting of {111} plane, which is the most stable facet of Ag. The Ag atoms which are present in the sharp corners of the Tr-Ag-NPs are loosely bound and through Coulomb explosion process these may come out from the NPs during the laser ablation experiments [2]. Consequently, the share edges of the Tr-Ag-NPs get truncated, as shown schematically in Fig. 1(c). In Fig. 1(d), the shift in the PLB position ($\Delta\lambda$) w.r.t. that of as-synthesized Tr-Ag-NPs (i.e., 0 min sample) is plotted against the exposer time and from this it is clearly found that as the fluence is increased to 182 J/cm^2 the reshaping process even becomes faster.

3.2. Determination of nonlinear optical effects of Au coated Tr-Ag-NPs by *fs* Z-scan experiments

A material medium may get polarized on exposure to an electromagnetic wave and it can be written that the induced polarization (*P*) is proportional to the incoming electric field (*E*) i. e.,

$$\vec{P}(r,t) = \varepsilon_0 \chi^{(1)} \vec{E}(r,t) \,. \tag{1}$$

The intense electric field of laser can induce the electric polarization in atoms and molecules. But when the incident field is sufficiently intense then the polarization becomes nonlinear and many optical properties that are nonlinear in nature are begins to appear which are hardly evident in the low intensity region. However, when the intensity of the incident E. M. radiation is sufficiently large then the polarization is related to the incident the electric field vector as can be written as [6],

$$\vec{P} = \varepsilon_0 \chi^{(1)} \vec{E} + \varepsilon_0 \chi^{(2)} \vec{E}\vec{E} + \varepsilon_0 \chi^{(3)} \vec{E}\vec{E}\vec{E} + \varepsilon_0 \chi^{(4)} \vec{E}\vec{E}\vec{E}\vec{E} + \cdots. \tag{2}$$

Where, $\chi^{(2)}$, $\chi^{(3)}$, etc. are the nonlinear susceptibility of second-, third- order etc. of the materials. In terms of the order of magnitude three susceptibilities are in the ratio $\chi^{(1)}{:}\chi^{(2)}{:}\chi^{(3)}$ =1:10^{-8}:10^{-16} [6]. It is well established that the first order susceptibilities $\chi^{(1)}$ is responsible for the linear refractive index, birefringence and dispersion [6].
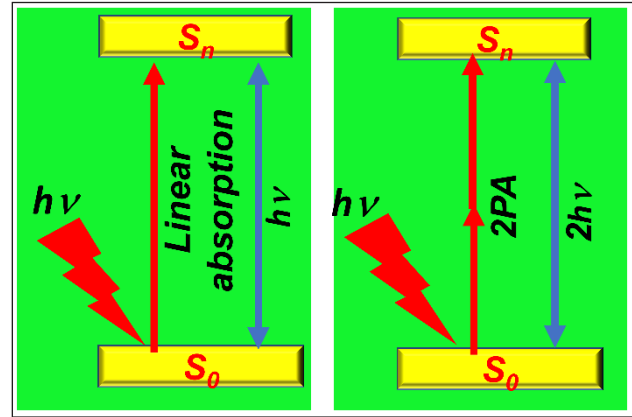

Fig 2: A schematic representation of linear and nonlinear (i. e., 2PA) absorption processes.

On the other hand, the second order susceptibility $\chi^{(2)}$ is responsible for interesting NLO phenomena like SHG, parametric generation or frequency mixing and third order nonlinear susceptibilities $\chi^{(3)}$ is responsible for the nonlinear absorption (NLA), third harmonic generation (THG), etc. [6].

However, the linear and nonlinear 2PA processes are shown schematically in Fig. 2. In presence of more than one NLA phenomena, the intensity dependent NLA can be expressed as a function of the incident intensity (*I*) as [7, 8],

$$\alpha = \beta_0 + \beta_{2PA}I + \beta_{3PA}I^2 + \cdots\cdots \tag{3}$$

Among different available techniques, open aperture (OA) Z-scan technique is very much useful in the determination of the NLO properties of any materials including the NLA properties of the nanostructured materials [3, 6, 7].

Tr-Ag-NPs are known for their local field (LF) effect and by coating it with Au, the magnitude of the LF can be significantly enhanced as found from COMSOL simulation (data not shown here) [3]. We have prepared a typical Tr-Ag-NPs@ Au core-shell nanostructure, with Tr-Ag-NPs as core and Au shell of thickness around 6 nm as determined by TEM measurements (a typical TEM image is shown in Fig. 3a). The enhanced LF in such Tr-Ag-NPs@Au nanostructure may results in higher order NLO response.

A schematic of the usual Z-scan setup has been shown in the Fig. 3 (b). The sample is scanned through the pre and post focal positions of the first lens and far field transmission traces are measured. The scan range is dependent on the several factors and most importantly on the sample thickness. The sample thickness is usually kept in such a way that its value becomes less than the Rayleigh length so that the thin sample approximation is becoming applicable. When simultaneously two different k and $(k+1)$ PA nonlinear absorption processes are present in the medium, then the propagation of the laser beam can be monitored with the Eq. 4 [7].

$$\frac{dI}{dz'} = -\beta_0 I - \beta_{kPA} I^k - \beta_{(k+1)PA} I^{(k+1)} \quad (4)$$

Where, β_{kPA} is the kPA coefficient. When the medium exhibits only 2PA, its coefficient β_{2PA} can be obtained by fitting the normalized OA Z-scan transmittance data with the following solution of the above Eqn. 4 [8],

$$T(Z) = \sum_{m=0}^{\infty} \left[-\frac{L_{eff}^{(k)} \beta I}{(k+1)^{3/2}(1+Z^2/Z_0^2)} \right]^m \quad (5)$$

Here, Leff, represents the effective path length of the medium travelled by the light pulse, and L is the actual length of the medium.

In case of three photon absorption (3PA) induced 4PA process the β_{3PA} and β_{4PA} can be determined by fitting the normalized OA Z-scan data by using the following solution of Eq. 4 as [7],

$$T(Z, \psi_3, \psi_4) = \sum_{n=0}^{4} \sum_{i=0}^{4} a_{ni} \psi_3^n \psi_4^i. \quad (6)$$

Where, $\psi_k = \dfrac{\left[(k-1)\beta_k I_0^{(k-1)} L_{eff}^{(k)} \right]^{\frac{1}{k-1}}}{(1+Z^2/Z_0^2)}. \quad (7)$

In the present study the co-presence of three and four photon absorptions (3PA & 4PA) at 532 nm is successfully identified by using the Z-scan technique in OA mode with an ultrafast (100 fs, 1 KHz) laser radiation.

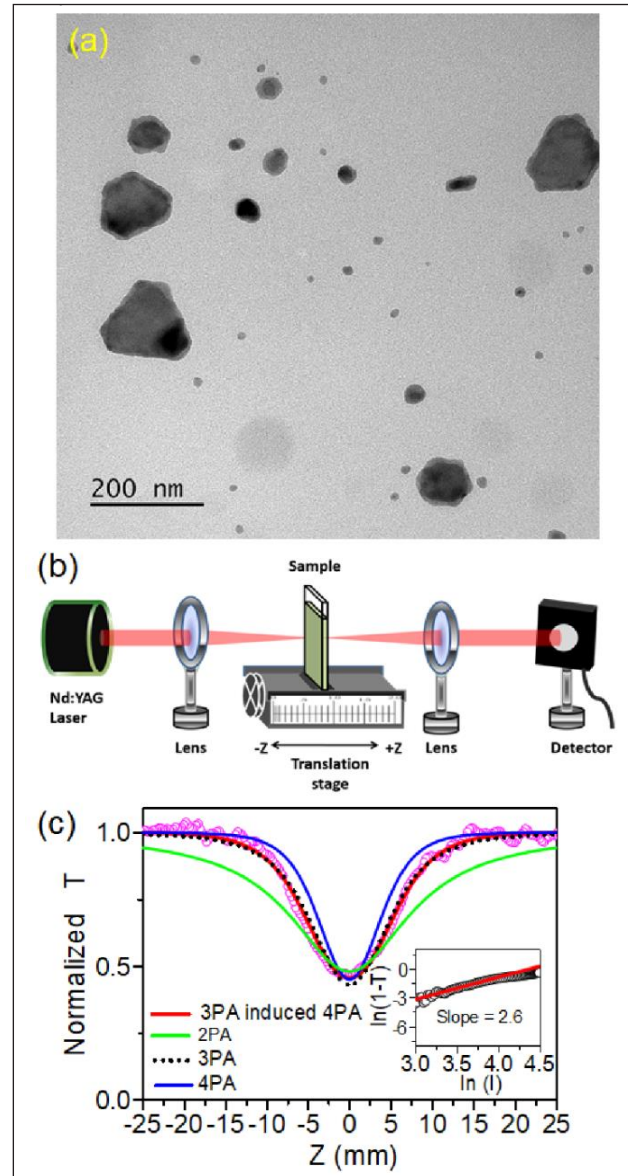The OA Z-scan data shown in the Fig. 3(c) and the symmetrical valley in both side of the

Fig 3: (a) TEM image of the Tr-Ag-NPs@Au nanostructure. (b) Schematic representation of the Z-scan experiment setup. (c) Theoretical fitting to the OA Z-scan data with 2PA, 3PA, 4PA and 3PA induced 4PA model and in the inset ln(1-T_OA) vs ln I plot is presented. (Fig. C was adapted from the ref. no. 3)

Z=0, represent the reverse saturable absorption behaviour of the Tr-Ag-NPs@Au nanostructure. Interestingly, the appropriate fitting to the normalized OA Z-scan data is obtained with the Eq. 6 by considering the co-presence of 3PA and 4PA [Fig. 3(c)].

The extracted value of β_{3PA} and β_{4PA} are found to be (5.3 to 0.18) × 10^{-3} (cm³/GW²) and (0.18 to

48) × 10^{-3} (cm^5/GW^3), respectively, for I_0 lying between 51 and 89 GW/cm^2. The linear fitting of the $ln(1-T_{OA})$ vs. $ln (I)$ data [shown in the inset of Fig. 3(c)] showed that the slope of the line is 2.6 at $I_0 = 89$ GW/cm^2. This result also established that 4PA phenomenon is contributing to the nonlinear optical absorption in the sample during the OA z-scan experiments.

In recent times high power lasers are extensively used in various applications ranging from industry to medicine. These has generated much research interest towards the search for new NLO materials which can acts as a passive optical limiter and protects human eyes as well as the optoelectronic instruments and solid-state optical sensors from their damages even in the presence of intense laser beams. The optical limiting (OL) property of a device is defined by its capabilities to keep the output power below some specified maximum value regardless of the magnitude of the input laser attains a high value i.e., it's transmittance drops drastically at high input power. OL performance of a material is being measured by its value of limiting threshold, defined by the input fluence at which the intensity of the output beam drops by 50 % w. r. t. the input beam intensity. In our study the OL threshold for the Tr-Ag-NPs@Au nanostructure is found to be 5.4 mJ/cm^2 which is very much lesser than those of some 2D nanomaterials, like MoS_2, graphene, and graphene oxide nanosheets [3]. Also, further discussions related to this work have been made elaborately in Ref. [3].

3.3 Application of Tr-Ag-NPs in development of random laser

The basic component of laser [9] contains a gain medium, a mechanism to energize it, and something to provide optical feedback as shown schematically in the Fig. 4(a). In most of the cases a pair of highly polished parallel mirrors [10] provides the optical feedback. Light enters into the gain medium from a highly luminous source (pumping), travels through the gain medium, bounces back and forth by the mirrors and simultaneously gets amplified by the stimulated emission from the gain medium. However, there are several conditions that must have to be fulfilled if the laser is to operate successfully. The cavity condition is so chosen that the total gain in the cavity is larger than the losses, the system reaches a threshold and lasing process starts. The emission characteristics of lasing modes *i.e.*, the directionality and its frequency are determined by the cavity parameters. In conventional laser any randomness is undesirable because it drives the system away from the lasing condition.

In our secondary class we often learned why the sky appears blue? It is due to the scattering [11] of the sunlight by molecules, tiny water droplets and dust particles in air. Smaller the wavelength more will be the scattering and this is why sky appears blue. Thus, scattering plays a very important role in our daily life. Each object which appears opaque, scatter incident light in all directions. Scattering of classical wave in random medium has been studied for centuries. The Brownian motion [12] which is microscopic manifestation of diffusion process (wave propagation) in the macroscopic level was first observed by Robert Brown in year 1827 while
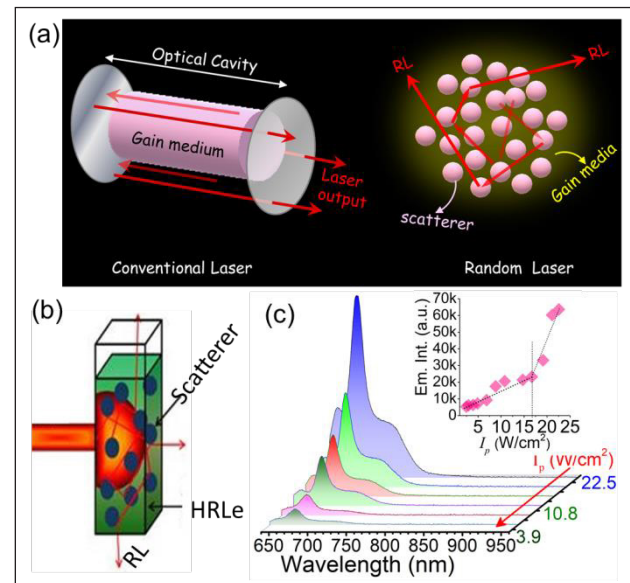

Fig 4: (a). A schematic diagram of a conventional and random laser. (b) Schematic representation of RL generation. (c) Emission spectra of HRL in presence of Tr-Ag-NPs at different input intensities (I_p in W/cm^2), inset: variation of emission intensity with I_p. (Adapted from the ref. no. 4)

looking through a microscope at particles trapped in cavities inside pollen grains in water. Brownian motion was researched by Langevin and Einstein in the late 19th and early 20th centuries [12]. After the discovery of the diffusion equation, random travel of classical particles could be examined quantitatively using the diffusion coefficient. Boltzmann explored the classical non-equilibrium transport problem and proposed the renowned Boltzmann equation. In 1958, Anderson has reformulated the Boltzmann's equation during the introduction of localization of electrons in a spatially random potential 1, 5, 11-14].

The transport of light intensity in such a context of strong scattering can be characterized by a random walk [1, 13-14].

Multiple scattering traps light, transforming the disordered material into a virtual cavity. In a typical laser, this can be utilized to observe a lasing threshold in the presence of gain and induced amplification of spontaneous emission. A "random laser" is a laser that does not have any reflectors [15]. The deliberate creation of nanostructured scattering environment inside a gain medium helps in amplification of photons occuring via multiple scattering events, before they exit the gain media [16], as shown in Fig. 4(b).

Unlike the conventional lasers, RLs do not require a complicated and costly optical arrangement. RLs can be either coherent or incoherent depending on the type of feedback mechanism. Generally, coherent or resonant feedback occurs in strongly scattering regime i.e., when the scattering mean free path (l_{sc}) of light is close to the emission wavelength ($l_{sc} \leq \lambda$). In coherent feedback induced RLs; above threshold pump energy, dramatic enhancement in the emission intensity could be observed with the appearance of discrete lasing modes [5]. However, incoherent or non-resonant feedback induced RL emission can be observed when $l_{sc} > \lambda$ i.e., in weakly scattering regime. Depending on the type of scatterer, a RL system can be either active or passive. In active RL system, both amplification (gain) and scattering are offered by the same element.

Likewise, in our case, Plasmonic property of the Tr-Ag-NPs has been used as passive scatterer for generation of RL emission from a bio-pigment i.e., HRL extract (gain medium) under CW pump laser, as shown schematically in Fig. 4(b). Figure 4(c) depicts the pump intensity dependent spectra of HRL extract in presence of Tr-Ag-NPs as scatterer. Furthermore, details of the theoretical calculations for estimation of l_{sc}, and other parameters controlling the RL action in HRL extract are available in our recent report [4]. However, RL emission from HRL extract at ~ 674 nm is achieved with a lasing threshold of 16.8 W/cm² (inset, Fig. 4 (c)) in the presence of Tr-Ag-NPs as passive scatterer.

4. Conclusions

Laser radiations are found to be playing important roles in development of materials for different applications. Laser radiations are also employed in the field of nanotechnology for development, reshaping and characterization of properties of nanostructured materials. Here, the tuning of the Plasmon resonance band of Tr-Ag-NPs has been shown to be possible by simply exposing it to *ns* pulse laser radiation operated at the wavelength of 1064 nm. The NLA coefficients *i.e.*, β_{3PA} and β_{4PA} are also determined by using an (532 nm, 100 *fs*) pulsed laser radiation and by using Z-scan technique. Furthermore, generation of Plasmon assisted RL in the visible region has been found to be possible from a bio-pigment by using Tr-Ag-NPs has been described as passive scatterer element.

in the Z-scan measurement. Authors are thankful to Dr. S. Ghosh and Dr. S. K. Pal of Assam University for their help in COMSOL studies.

References

1) M. Noginov, Solid State Random Laser, (2005) 1, Springer, New York, NY.
2) K. Mondal, S. Biswas, P. Kumbhakar, Plasmonics (2020) 15, 145–153.
3) K. Mondal, S. Biswas, T. Singha, S. K. Pal, S. Ghosh, P. K. Datta, P. Kumbhakar, Opt. Lett. (2021) 46, 4879–4882.
4) S. Biswas, P. Kumbhakar, Nanoscale (2017) 9, 18812-18818.
5) N. M. Lawandy, Nature Phys. (2010) 6, 246–248.
6) R. W. Boyd and B. R. Masters, Nonlinear optics, J. Biomed. Opt., (2009) 14, 029902.
7) B. Gu, X.-Q. Huang, S.-Q. Tan, M. Wang, W. Ji, Appl. Phys. B (2009) 95, 375–381.
8) M Sheik-Bahae, A. A. Said, T. H. Wei, D. J. Hagan, E. W. V. Stryland, IEEE J. Quantum. Electron. (1990) 26, 760–769.
9) A. L. Schawlow, C. H. Townes, Phys. Rev. (1958) 112, 1940.
10) Schawlow, L., Lasers and Light, W. H. Freeman and Co. (1969).
11) L. S. Rodberg, R. M. Thaler, Introduction to the quantum theory of scattering. Academic Press Inc., 111 Fifth Avenue, New York NY 10003, USA 1st edition 1985.
12) A. Einstein, Ann. d. Phys., (1905) 17, 549.
13) P. W. Anderson, Phys. Rev., (1958) 109, 1492–1505.
14) R. P. Feynman, R. B. Leighton, M. Sands, The Feynman Lectures on Physics, (1989) Vol II, 2-1.
15) D. S. Wiersma, M. P. van Albada, A. Lagendijk, Nature (1995) 373, 203–204.
16) S. Kedia, S. Sinha, Results Phys. (2017) 7, 697–704.

Prof. Pathik Kumbhakar *is presently serving as Professor (HAG) at Dept. of Physics, NIT Durgapur, India. He has received B.Sc. (Hons.), M.Sc. (Physics), and Ph.D. degrees in1993, 1995, and 2003, respectively from B.U., Burdwan, India. He did postdoctoral research work (during 2002–2004) at Tokyo University, Japan in Laser-Technology. He has received several awards/citations including FRSC, IAPT-DSM award, and Fellow of WAST (FAScT). He is also a Senior Member of OSA. His name appeared in the Stanford list of world's top 2% scientists (single year data, 2021). His current research activities are focused on the area of Synthesis of semi-conductor, metal, 2D materials and carbon (GO, rGO, Carbon Dots, Graphene, etc.) nanostructured materials for linear and nonlinear optical, catalytic properties, energy harvesting, and random lasing.*

Mr. Koushik Mondal *received his M. Sc. in Physics from Visva Bharati University, West Bengal and currently pursuing his doctoral studies under the guidance of Professor Pathik Kumbhakar. His doctoral research involved in linear and nonlinear optical properties of noble metal nanostructures and their nanocomposites.*

Dr. Subrata Biswas *received his Ph.D. degree from at Dept. of Physics, NIT Durgapur. Prior to his doctoral degree, he has received his M. Sc. in Physics from Visva Bharati University, West Bengal, India. His research interest focuses on investigation on synthesis and nonlinear optical response of Plasmonic nanostructures, generation of random laser in disorder optical system.*

Dr. Ashim Pramanik *received his Ph.D. degree from at Dept. of Physics, NIT Durgapur. Prior to his doctoral degree, he has done M.Tech. in Advanced Materials Science and Technology from NIT Durgapur. His current research interest focuses on the area of Synthesis of 2D materials carbon (GO, rGO, Carbon Dots, Graphene, etc.) nanostructured materials for linear and nonlinear optical, catalytic properties, energy harvesting, and random lasing application.*

Fluorescence Correlation Spectroscopy: An Emerging Tool to Probe the Dynamics of Molecular Self-assembly

Subhankar Kundu* and Abhijit Patra*

Department of Chemistry, Indian Institute of Science Education and Research Bhopal,
Bhopal By-Pass Road, Bhauri, Bhopal 462066, Madhya Pradesh, India.
E-mail: subhankar16@iiserb.ac.in and abhijit@iiserb.ac.in

Abstract

Supramolecular self-assembly with tunable emission found enormous attention for diverse applications in light-harvesting, nanodevices, bioimaging, sensing, and switches. However, deciphering the evolution of molecular self-assembly from a solution leading to diverse nanostructures is a challenge. The morphology of the molecular aggregates can be obtained using electron microscopy, i.e., solid-state analysis. On the other hand, their optical properties are mostly studied in the dispersion state. Nevertheless, asserting a correlation between the morphology and the emission property in the dispersion is often rudimentary and needs a critical assessment. Recently, we deciphered a combined picture of the evolution of supramolecular nanofibers from solution through oblong-shaped nanoaggregates correlating the intriguing processes of molecular self-assembly in both solution/ dispersion and the solvent evaporated state using a thiophene-based small organic molecule, TPAn. In this article, we emphasize the scope of fluorescence correlation spectroscopy (FCS) as an emerging tool to probe the evolution of molecular self-assembly in complex and heterogeneous media.

1. Introduction

Self-assembly deals with the thermodynamically driven spontaneous associations of molecules through noncovalent interactions that play a unique and significant role in creating several complex bio-architectures like DNA, proteins, peptides, etc., and regulates diverse cellular activities.[1] Myriad unique patterns are evident in nature, such as the feather of the peacock, petals of flowers, seashell, etc. Such natural self-assembly processes have been encouraged researchers to construct diverse nano/microarchitectures of the micelle, vesicles, gels, etc., over the last few decades (Figure 1).[2] Additionally, the tunable emission of such artificial self-assembled structures found immense applications in light-harvesting, biomedicine, sensing, and imaging.[3] Thus, exploring the underlying mechanism behind the formation of supramolecular self-assembly and probing their dynamics is necessary to construct
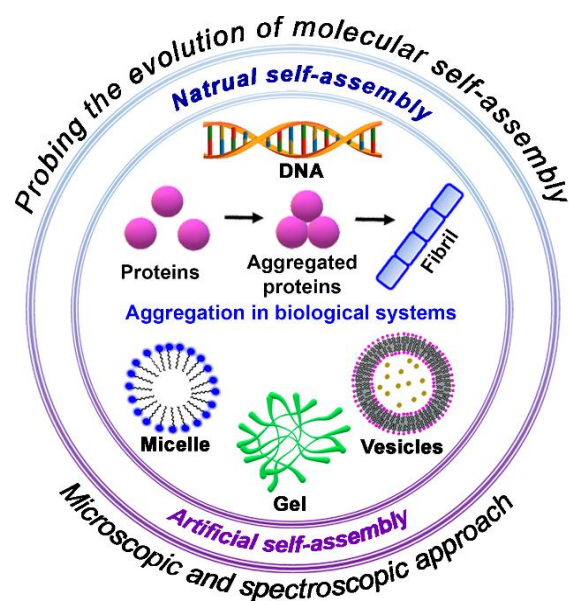

Figure 1. Schematic illustration depicting the theme of the article probing the evolution of molecular self-assembly through a combined microscopic and spectroscopic approach; the pictorial representation of diverse natural and artificial self-assembled structures.

Table 1. Different analytical tools to probe the molecular self-assembly in solution/ dispersion and solid-state.

Solid-state	Solution/ dispersion
● *Field emission scanning electron microscopy (FESEM)* [4]	● *Dynamic light scattering (DLS)* [8]
● *Transmission electron microscopy (TEM)* [5]	● *Fluorescence correlation spectroscopy (FCS)* [9]
● *Atomic force microscopy (AFM)* [6]	*Challenge:*
● *Confocal laser scanning microscopy (CLSM)* [7]	*deciphering the evolution of molecular self-assembly in solution or dispersion*

efficient multifunctional molecular materials. In this context, microscopic imaging tools such as transmission electron microscopy (TEM), field emission scanning electron microscopy (FESEM), atomic force microscopy (AFM), and confocal laser scanning microscopy (CLSM) are useful to elucidate the self-assembled structures only in the solid-state (Table 1).[4-7] On the other hand, probing the evolution of molecular self-assembly in the solution is not straightforward. In this view, fluorescence correlation spectroscopy (FCS) finds an important consideration to understand the growth of diverse self-assembled structures in solution and dispersion states (Table 1).[9] The fluctuations of the fluorescence intensities due to molecular diffusion and/ or conformational variation were invoked to demonstrate several dynamic processes like conformational changes of proteins, different binding processes (e.g., dye and proteins), aggregation, etc. However, the exploration of FCS as a tool in material chemistry to understand the growth and dynamics towards the formation of diverse nanomaterials to polymers, covalent organic frameworks, etc., has been rarely explored to date.

γ-Cyclodextrin (γ-CD) and coumarin 153 (C153)-based nanotube formation in solution was explored by Bhattacharyya and coworkers using FCS.[10] The diffusion time (τ_d) obtained from the FCS analysis was employed for the determination of the length of the nanotube. The

results indicated that the nanotubes were much larger (~ 480 times) than that of the 1:1 complex of γ-CD and C153 and the nanotube consisted of ~ 950 γ-CD units. Ganguli and coworkers explored the evolution of iron oxalate nanorods using electron microscopy and FCS.[11] The FCS data revealed that nanoparticles formed at the initial stage further agglomerated to form the nanorods. We demonstrated an intriguing case of the evolution of all-organic molecular anisotropic nanostructure through spontaneous self-assembly in solution employing a π-conjugated thiophene-pyridoacetonitrile-based small organic molecule, TPAn, using FCS coupled with FESEM and TEM.[12] In this article, we would like to highlight the scope of FCS analysis to elucidate the complex self-assembly processes of π-conjugated organic molecules using the results obtained with TPAn.

2. Experimental Section

The Knoevenagel condensation reaction was employed to obtain TPAn from the precursor molecules 4,4′-(thiophene-2,5-diyl)dibenzaldehyde (TBA) and 2-pyridylacetonitrile.[12] The stock solution (0.2 mM) of TPAn was prepared by dissolving 1 mg of the solid compound in 10 mL of tetrahydrofuran (THF). Then, 30 µL of the solution was quickly added to 3 mL of THF-water mixture under sonication for 1 min. As prepared dispersion was used for the spectroscopic measurements. TPAn dispersions were drop-casted on a silicon wafer and subsequently dried under vacuum for 6 h for the electron microscopy measurements. The FCS data for the dispersions with 50-70% water content and acid-base-induced reversible morphological transformation were fitted using the two-component diffusion model for both free and aggregated TPAn (equation 1). A three-dimensional (3D) diffusion model was used to fit the FCS data for TPAn in 20% THF and 80% water containing dispersion (equation 2).[12]

$$G(\tau) = \frac{1}{N}\left[\left[\frac{1-y}{\left(1+\frac{\tau}{\tau_{D1}}\right)}\frac{1}{\sqrt{1+\frac{\tau}{\omega^2\tau_{D1}}}}\right] + \left[\frac{y}{\left(1+\frac{\tau}{\tau_{D2}}\right)}\frac{1}{\sqrt{1+\frac{\tau}{\omega^2\tau_{D2}}}}\right]\right](1)$$

$$G_{3D}(\tau) = \frac{1}{N} \frac{1}{1+\frac{\tau}{\tau_D}} \frac{1}{\sqrt{1+\frac{\tau}{\omega^2\tau_D}}}. \qquad (2)$$

The autocorrelation function is noted as $G(\tau)$ in the equations. The average number of fluorescent particles in the focal volume is abbreviated as N. The total diffusion time is and the correlation time is τ. The total diffusion times for the free TPAn molecules (y) and TPAn aggregates (1-y) are denoted as and , respectively. ω is the structural parameter, and it is the ratio of longitudinal radius (ω_z) and transverse radius (ω_{xy}) for the confocal volume. Rhodamine 6G solution was used as a standard to calibrate the instrument.[12]

3. Results and discussion

Our cardinal objective is to highlight the distinction between the self-assembled nanostructures obtained in the dispersion probed by fluorescence correlation spectroscopy (FCS) and that imaged after drying the same dispersion through electron microscopy using TPAn as a model system. TPAn exhibited green emission in organic solvents. A THF and water mixture was used to probe the molecular self-assembly of TPAn. A drastic change in absorption and emission was noticeable for the dispersion with a water content of 80%. The dispersions of varying water contents (60%, 70%, and 80%) were drop-casted to visualize the morphology
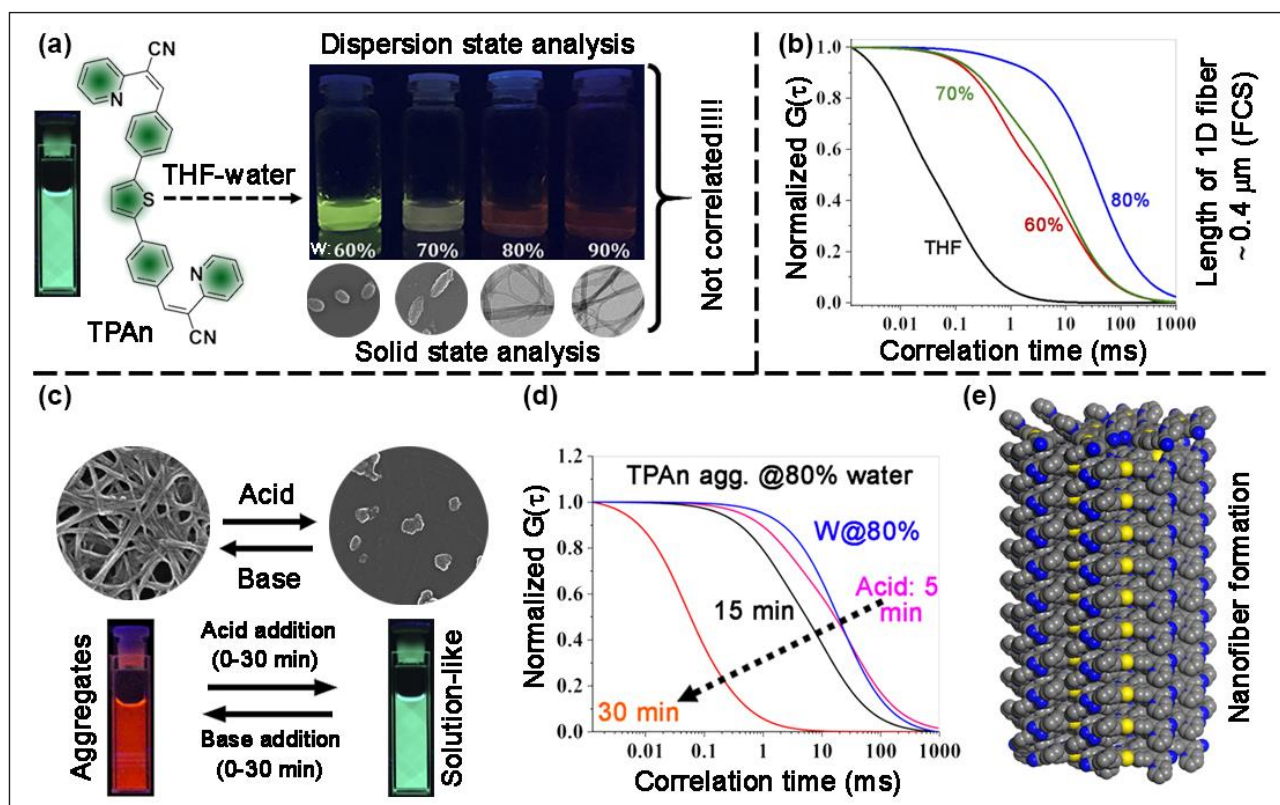

Figure 2. Molecular structure of TPAn. The digital photographs of TPAn in THF (5 μM) and THF-water binary solvent mixture under UV irradiation (l_{ex} = 365 nm); corresponding electron microscopy images of the TPAn dispersions with the varying water fraction. (b) The normalized FCS traces for TPAn both in THF (1 nM) and in THF-water solvent mixtures (2 μM). (c) Acid-base-induced reversible morphological transformation of TPAn dispersion (20% THF-80% water) between connected network of nanofibers and discrete nanoparticles at pH ~ 0.7 and ~ 7.2, respectively demonstrated through FESEM images and the corresponding dispersion under the illumination of UV light (l_{ex} = 365 nm). (d) The normalized FCS traces of the TPAn dispersion (20% THF-80% water) at pH ~ 0.7 with increasing time up to 30 mins. (e) The space-filling model for the nanofibers of TPAn. The figure was adapted from the reference number 12.
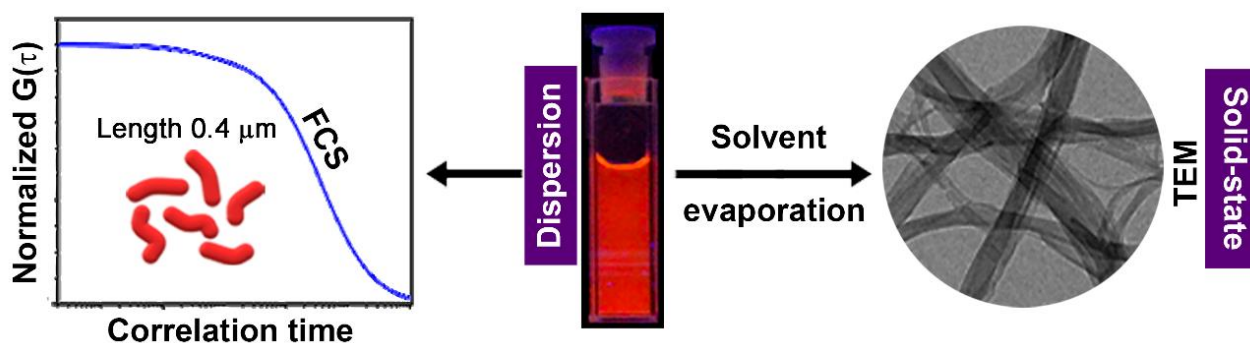
Figure 3. Pictorial representation highlighting the distinction of the nanostructures obtained in the dispersion probed by fluorescence correlation spectroscopy (FCS) and that obtained after drying the same dispersion through electron microscopy.

of the aggregates through different microscopic tools like FESEM, TEM, and AFM. A sequential morphological evolution from spherical, oblong-shaped particles, to connected networks of nanofibers was noticed by tuning the polarity of the medium by increasing the water fractions from 60% to 80% (Figure 2a). However, the morphological transformation (particles to connected networks of nanofibers) due to the evaporation of the solvent molecules during the sample preparation for the microscopic analysis could not be ruled out. Thus, we employed FCS to understand the aggregation behavior in the dispersion state itself. Only a four-fold enhancement in the diffusion time was noticeable for the aggregates having a water content of 80% as compared to that of 70% (Figure 2b). On the other hand, the FESEM images showed a drastic change in the morphology for the dispersions with a water content of 80% compared to 70% (Figure 2). The diffusion time obtained from the FCS analysis was further used to calculate the length of the nanofibers in dispersion by solving the equations 3-5 at Stick hydrodynamic boundary conditions through the Newton Raphson method.

$$D_\parallel = \frac{k_B T}{2\pi\eta L}\ln(L/d)\dots\dots(3)$$

$$D_\perp = \frac{k_B T}{4\pi\eta L}\ln(L/d)\dots\dots(4)$$

$$D_t = (D_\parallel + 2D_\perp)/3\dots\dots(5)$$

Here, the Boltzmann constant is denoted as k_B. T is the temperature during the time of the measurements. η is the viscosity of the medium. The diffusion coefficient parallel to the major axis and minor axis were denoted as $D_\parallel$ and , respectively. is the total diffusion time. The length and the diameter of the fibers were denoted as L and d, respectively.

FCS analysis revealed the formation of smaller-sized (~ 0.4 µm) anisotropic nanoaggregates in the dispersion contrary to entangled long nanofibers obtained through electron microscopy. These smaller-sized nanoaggregates were converted to the network of nanofibers through solvent evaporation during the sample preparation for FESEM/ TEM/ AFM studies (Figure 3).

External stimuli like acid-base, light, temperature, etc., play an important role in regulating the dynamics of self-assembly processes.[13] In addition to obtaining the length and hydrodynamics radius of aggregates, the FCS measurements along with electron microscopy can also be used to elucidate the dynamics of the molecular self-assembly in the solution/ dispersion. Primarily, the electron microscopy images demonstrated the reversible morphological transformation of TPAn between the connected network of nanofibers and spherical nanoparticles through the addition of acid and base, respectively, to the 80% water-containing dispersion (Figure 2c).[12] The FCS

study for the acid-base-induced aggregation-disaggregation processes further shed light on the dynamics of the self-assembly process (Figure 2d). FCS traces of the TPAn dispersion (80% water content) were found to be similar to that obtained for THF solution upon addition of acid. The same FCS trace (80% water-20% THF) was obtained upon the addition of the base to the acidified dispersion (Figure 2d). Thus, the combination of FCS analysis and electron microscopy can provide a better understanding to the evolution dynamics of diverse self-assembled structures in a solution or a dispersion state.

References

1. (a) D. Philp and J. F. Stoddart, *Angew. Chem. Int. Ed.*, **1996** (35) 1154; (b) G. M. Whitesides and B. Grzybowski, *Science*, **2002** (295) 2418.

2. S. I. Stupp and L. C. Palmer, *Chem. Mater.*, **2014** (26) 507.

3. (a) S. Kundu, B. Sk, P. Pallavi, A. Giri and A. Patra, *Chem. Eur. J.*, **2020** (26) 5557; (b) S. Kundu, B. Behera, A. Giri, N. Saha and A. Patra, *Chem. Commun.*, **2021** (57) 6875; (c) S. Das, S. Kundu, B. Sk, M. Sarkar and A. Patra, *Org. Mater.*, **2021**, DOI: 10.1055/a-1679-955.

4. R. Kubota, W. Tanaka and I. Hamachi, *Chem. Rev.*, **2021** (121) 14281.

5. X. Zhang, Z. Chen and F. Würthner, *J. Am. Chem. Soc.*, **2007** (129) 4886.

6. J. Singh, A. T. Sabareesan, M. K. Mathew and J. B. Udgaonkar, *J. Mol. Biol.*, **2012** (423) 217.

7. O. Gould, H. Qiu, D. Lunn, J. Rowden, R. Harniman, Z. Hudson, M. Winnik, M. Miles and I. Manners, *Nat. Commun.*, **2015** (6) 10009.

8. J. Yang, K. Wu, C. Koňák and J. Kopeček, *Biomacromolecules*, **2008** (9) 510.

9. K. Garai, B. Sahoo, S. K. Kaushalya, R. Desai and S. Maiti, *Biochemistry*, **2007** (46) 10655.

10. A. Mandal, D. Das, A. Das, S. Mojumdar and K. Bhattacharyya, *J. Phys. Chem. B*, **2011** (115) 10456.

11. S. Sharma, N. Pal, P. Chowdhury, S. Sen and A. Ganguli, *J. Am. Chem. Soc.*, **2012** (134) 19677.

12. S. Kundu, A. Chowdhury, S. Nandi, K. Bhattacharyya and A. Patra, *Chem. Sci.*, **2021** (12), 5874.

13. Y. Cai, Z. Guo, J. Chen, W. Li, L. Zhong, Y. Gao, L. Jiang, L. Chi, H. Tian and W. Zhu, *J. Am. Chem. Soc.*, **2016** (138) 2219.

Mr. Subhankar Kundu *completed his B.Sc. and M.Sc. from Scottish Church College (University of Calcutta, 2014) and National Institute of Technology Rourkela (2016), respectively. He was the gold medalist during his M.Sc. Later he joined the Indian Institute of Science Education and Research Bhopal for Ph.D. under the supervision of Dr. Abhijit Patra. His research is on exploring the molecular self-assembly of organic fluorophores through the combination of spectroscopic and microscopic tools.*

Dr. Abhijit Patra *has been working as an Associate Professor in the Department of Chemistry at the Indian Institute of Science Education and Research Bhopal. He completed his Ph.D. working with Prof. T. P. Radhakrishnan at the University of Hyderabad in 2009. Then he moved for postdoctoral research at PPSM, ENS Paris-Saclay, and the University of Wuppertal as an Alexander von Humboldt fellow before joining at IISER Bhopal in 2012. His research interests are developing functional fluorescent molecules for light-harvesting, intracellular imaging, and porous organic polymers for carbon dioxide fixation, photocatalysis, and energy storage.*

Understanding of the Photophysics of Faecal Pigments and their Zinc Complexes towards Sensitive Fluorescence Based Detection

Swayam Prakash and Ashok Kumar Mishra*

Department of Chemistry, Indian Institute of Technology Madras, Chennai 600036, India
(email: mishra@iitm.ac.in)

Abstract

Faecal pigments (FPs) analysis is an emerging and very active area in the field of water quality analysis and monitoring. The presence of faecal pigments like stercobilin (SB) and urobilin (UB) is considered as indicators of faecal pathogens in water. A detailed photophysical study of the pigments and their zinc (II) complexes shows that in aqueous media, FPs have the intriguing presence of multiple emitting species, which indicate the coexistence of monomers (λ_{ex}= 525 nm, λ_{em}= 540 nm), lower-order H-aggregates (dimers) (λ_{ex}= 506 nm, λ_{em}= 516 nm), and higher-order H-aggregates (λ_{ex}= 480 nm, λ_{em}= 500 nm) even at a very low concentration. Hydrogen bonding as well as π-π stacking interactions appear to play major roles in the formation of H-aggregates by the FPs. This work uses spectroscopic, thermodynamic and computational techniques to investigate the nature of the FP-Zn(II) complexation. Disaggregation of FPs and their subsequent complexation results 1:1 and 1:2 stoichiometry of FP-Zn(II) complexes. The insolubility of FP-Zn(II) complexes in water is increased which results the development of molecular aggregates of the complexes. This is the primary reason of time-dependent loss of FP-Zn(II) fluorescence which adversely affects the sensitivity of FPs detection in the aqueous medium. Both spectroscopic and computational evidence corroborate well with this proposed model. The study was further extended by utilizing this aggregation-induced emission phenomenon of FPs by using a series of primary alcohols with increasing viscosity. FP-Zn(II) has stable and maximum fluorescence intensity in 1-hexanol. Furthermore, 1-hexanol can also be used as an efficient extraction medium for FPs, which can enhance fluorescence as well as minimization of matrix components interference for high sensitivity detection (picomolar and sub picomolar concentration). This molecular-level understanding of FPs and FP-Zn(II) fluorescence behaviour could contribute to the development of aqueous phase analytical techniques based on fluorimetric detection of FPs.

1. Introduction

Water pollution is a major concern in present days due to contamination of environmental water with the millions of industrial, agricultural and chemical waste. Faecal matter (FM) is considered the primary source of water contaminant due to pathogenic viruses and bacterias. FM contains undigested carbohydrates, bile pigments (bilirubin, stercobilin (SB) and urobilin (UB)), dead leukocytes, protein, fat and inorganic substances.[1] The chemicals hydrogen sulfide, indole and skatole, are produced by various bacterial actions, which causes the odour of faeces.[2] Faecal pollutants are considered serious among other water contaminants because they act as a growing medium for various pathogenic and non-pathogenic organisms like viruses, bacterias etc. These water contaminants can only be managed by developing an online water monitoring and remediation system.

Faecal pigments (FPs) are open tetrapyrrole class of compounds. Urobilin (UB) and Stercobilin (SB) constitute important components of this class of pigments.[4] In hemolysis, bilirubin is produced, which form urobilinogen in the intestine.[5-6] Urobilinogen is converted to yellow colour urobilin, which can be found in the urine.[5] The stercobilinogen in the intestine is reduced
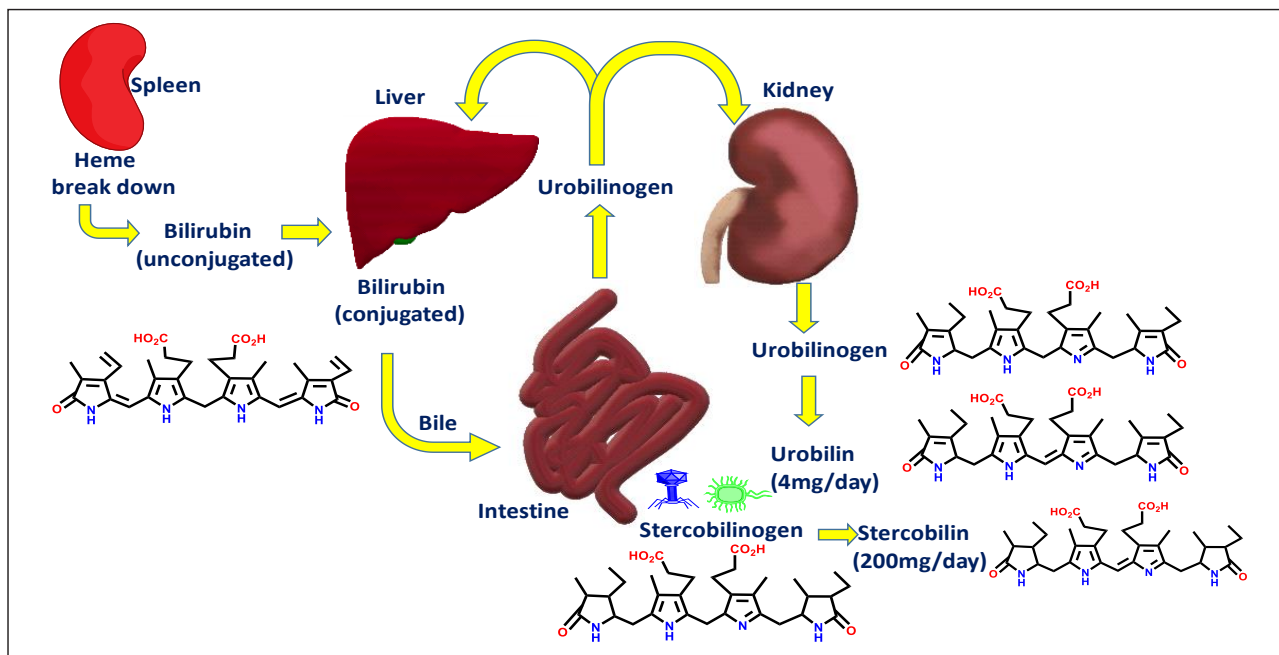
Fig 1: *The metabolic pathway for the formation of urobilin and stercobilin in the human body. (The concept of the scheme was adapted from Kumar et al.[3] and recreated with Chemdraw 20.0)*

directly to brown stercobilin, which gives the faeces to brown colour.[6] The detailed metabolic pathway for the formation of urobilin and stercobilin is presented in Fig 1. The amount of faeces excreted by an adult human is 100-250 mg of SB in faeces and 1-4 mg UB in urine per day.[5,7] This contribution is still much more from other livelihoods. FPs are excreted by many mammals, including humans, animals (cows, horses, and pigs), and birds.[4, 8-9] Many studies have revealed that faeces contaminate environmental water even in vary trace concentration.[4, 9]

2. Primary sources of faecal matter pollution

Ground and surface water quality is essential to public health in developed as well as developing countries. This water source is often utilized as a primary source for drinking water and food production use. Thus, there is a strong need for reliable evaluation of primary sources of faecal matter to successfully enforce and monitor water management practices to remediate faecal contaminants.

Broad classification of the primary sources of faecal pigment is (i) wild animal and bird waste, (ii) mismanagement of pet waste and (iii) improper planning of sanitary waste as depicted above (Fig 2).

FPs are considered as primary sources of water contaminants and the most relevant cause of human illnesses worldwide. The World Health Organization (WHO) had already recognized in 2018 that globally about 2 billion people use drinking water sources contaminated with faeces.[10] Thus, a cost-effective, rapid and real-time analytical method for water quality analysis is needed to be explored. The enhancement of FPs fluorescence by Zn(II) in alcoholic media is often used to detect and determine the faecal matter in aqueous media (Schlesinger's test). However, this is a laboratory based technique and is not amenable to on-site monitoring. At present, there is no easy-to-use and reasonably robust screening test available, based on the fluorescence of FP-Zn(II) complexes, despite its sensitivity. A detailed photophysical study of the complexes could enable adaptation of the existing method for real-time application. It has also the possibility of reaching the sensitivity levels offered by more sophisticated, expensive
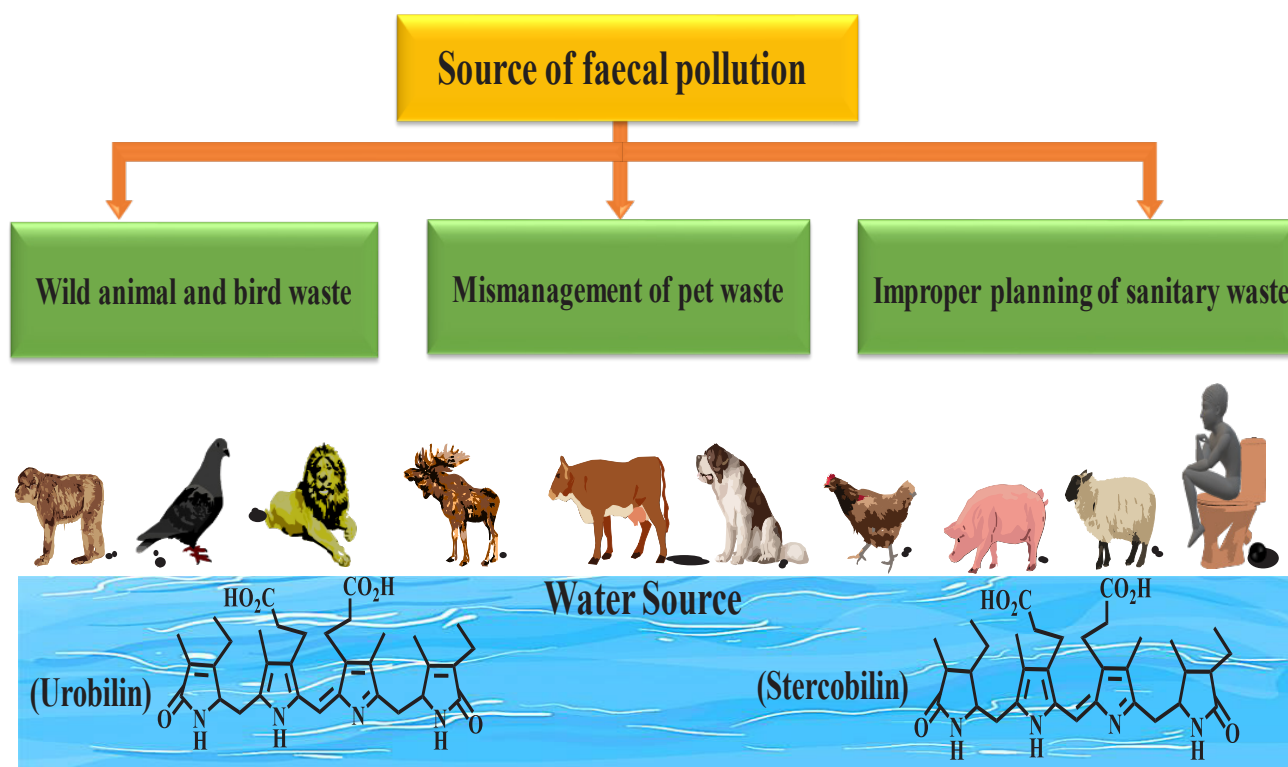
Fig 2: The primary source of urobilin and stercobilin contamination in ground and surface water. (Concept adapted from https://swuertzlab.com/research/ and recreated with Chemdraw 20.0)

and time-consuming instrumental methods like high-performance liquid chromatography-electrospray mass spectrometry (HPLC–ES-MS) and Gas chromatography-mass spectrometry etc. [11-12]

This article summarizes some of our recent work to towards understanding the fluorescence of urobilin, stercobilin and their Zn(II) complexes in water and other solvent media with particular focus on developing sensitive fluorescence based analytical methods that can be rapid and low-cost. For this work stercobilin hydrochloride and urobilin hydrochloride were purchased from Genetix biotech and Frontier Scientific, respectively. Photophysical studies were carried out by UV-2600 (SHIMADZU) for absorbance, Aqualog Horiba Jobin-Yvon and Fluoromax-4 spectrophotometer for steady-state emission. Horiba Jobin Yvon TCSPC instrument for fluorescence lifetime measurements.

3. Results and discussion

3.1 Photophysics of faecal pigments and their aggregates: (This work has been published in *Journal of Physical Chemistry A* [13])

In general organic molecules in the aqueous medium tend to self-associate, resulting in the development of dimers or higher aggregates due to their poor solubility in the solvating media.[14] Fluorescence studies revealed that FPs too exist in water in different stages of aggregation at different concentrations. In nanomolar and sub-nanomolar concentrations of FPs in aqueous media, higher aggregates (500 nm), lower aggregates (518 nm), and monomers (550 nm) were detected. Higher-order aggregates (500 nm) and lower-order aggregates (518 nm) appear to be present between 100 nM and 60 nM concentrations. Higher-order aggregates tend to break up between 1 nM and 0.5 nM concentrations in a 50% water-ethanol combination, creating a new emission band at
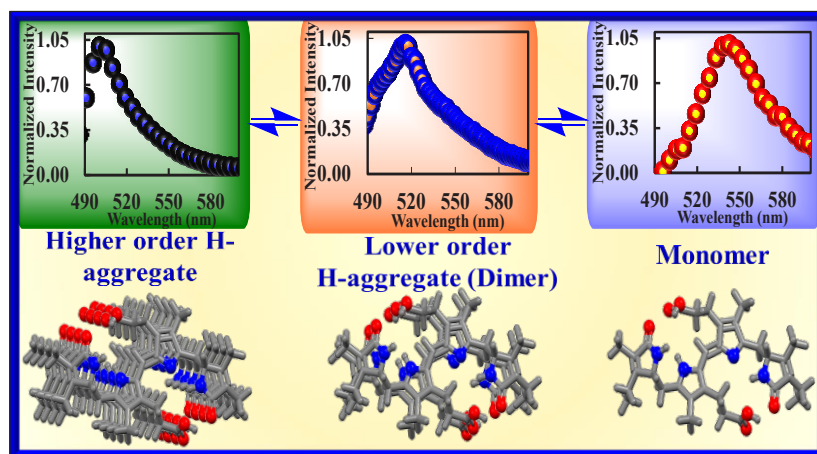
Fig 3: Higher order H- aggregation, lower order H-aggregation and monomer of FPs in the aqueous media (Ref: https://doi.org/10.1021/acs.jpca.0c08642)

a longer wavelength (550 nm) attributed to the monomer species. Since absorbance spectroscopy could not be used at nanomolar concentrations, fluorescence excitation spectra was used to determine the transition wavelengths. Four sets of independent experiments, including the variation of (i) FP concentration, (ii) temperature, (iii) pH, and (iv) ethanol/water mixture as solvent media, revealed the presence of monomer (540 nm), dimer (516 nm), and higher-order aggregates (500 nm) of FPs in aqueous solutions. In addition to steady-state fluorescence investigations, lifetime decay studies and excitation-emission matrix fluorescence studies (EEMF spectra) were carried out to better understand the aggregation dynamics. In the formation of H-aggregates of FPs in aqueous media, the contributions of $\pi-\pi$ stacking and hydrogen-bonding interactions were found to be crucial. The B3LYP functional and LANL2DZ basis sets were used to optimize the H-aggregate dimer geometry of FPs, with a solvent contribution IEFPCM model. Additionally, the experimentally observed results and theoretically predicted absorption maximums are well correlated.[13]

3.2 Photophysics of faecal pigments and faecal pigment-Zn(II) complexes in aqueous and mixed-aqueous media (This work has been published in *Chemosphere* [15])

In ethanol, FPs and their Zn(II) complexes have identical absorption and emission maxima.

When 20 mM zinc acetate was added, the absorption maximum remained unchanged after complexation. The absorbance maximum of SB and UB rises 2.5 to 3.5 times due to complex formation as compared to uncomplexed SB and UB. In ethanol, the fluorescence emission maxima of SB and UB emerges at 516 nm after a 475 nm excitation. When FPs are complexed, their emission intensity increases, similar to absorption, but the band maximum remains unchanged. However, the intensity of the band rises by 3-5 times when FP-Zn(II) is complexed. The solubility of the FP-Zn(II) complexes in the ethanol medium significantly enhance the fluorescence intensity.

Both SB and UB have absorption maximum at 488 nm in the aqueous medium. When zinc acetate salt is added, the absorbance at 488 nm decreases and a new band emerges at 505 nm. The electronic spectral behaviour of FPs in the aqueous media got changed due to the FP-Zn(II) complexation. The complexation-induced rigidity of the chromophoric units and the concomitant decrease in nonradiative decay rate constants (k_{nr}) of the excited singlet states were attributed to the enhancement of UB and SB fluorescence. In water, the fluorescence intensity of SB-Zn(II) and UB-Zn(II) complexes is 10 to 15 times lower than in ethanol. The low fluorescence intensity in water indicates the possibility of aggregation of the complexes. Dynamic light scattering (DLS) investigations were used to investigate the ground state aggregation in water. The aggregates of SB-Zn(II) and UB-Zn(II) complexes have hydrodynamic diameters of 394 nm and 987 nm, respectively. It confirms the presence of ground state aggregates in the aqueous media. It happens due to the complex's insolubility in water, which is correlated to emission lifetime and quantum yield investigations.[15] The average size of the aggregates steadily grows with time, as seen from
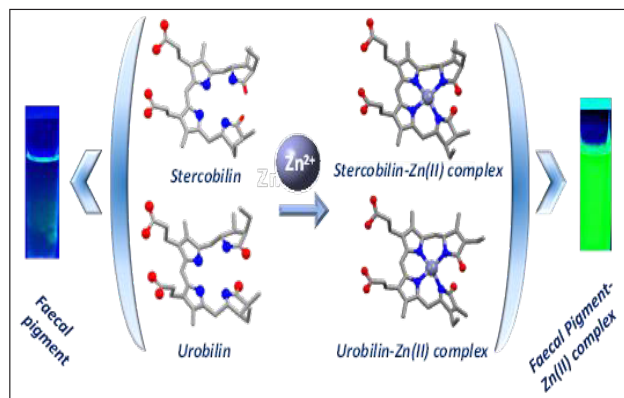
Fig 4: Graphical presentation of Photophysics of faecal pigments and faecal pigment-Zn(II) complexes in aqueous and mixed-aqueous media (Ref: https://doi.org/10.1016/j.chemosphere.2020.129189)

a time-dependent study of DLS. The progressive rise in the average size of FP-Zn(II) complexes in water reduced the complexes' emission intensity over time. This problem could be addressed by using water-alcohol mixed solvents. The best possible combination for FP-Zn(II) enhanced fluorescence in order to get high sensitivity analytical medium is ethanol:water (70:30). With the explicit and implicit solvent environment, theoretical studies indicate a deformed tetrahedral and pentacoordinate structure of FP-Zn(II) complexes. The study of FP-Zn(II) complexes in different physicochemical conditions, such as temperature, pH, light irradiation, and water hardness, yields a better knowledge of their fluorescence response to FPs analysis.[15]

3.3 Complexation behaviour of faecal pigments-Zn(II) and its various possible stoichiometry (This work has been published in *Journal of Molecular Structure*[16])

Given the relevance of this simple complexation-based fluorimetric analysis of FPs, it's surprising that a thorough investigation of the structure of the FP-Zn(II) complexes, their complexation stoichiometry, thermodynamics, and aggregation-disaggregation dynamics has not been studied yet. The ESI-MS spectra of the FPs (UB and SB) were recorded as a control experiment. Due to (M+H)[+], a stable precursor ion showed the mass spectrum of UB ($C_{33}H_{42}N_4O_6$) at

m/z 591.2. In the case of SB, a stable precursor ion was found at m/z 595.1 owing to (M+H)[+] and another at m/z 617.3 due to (M+Na)[+]. The elimination of four, three, and two methyl ions anticipated the peaks at m/z 568.1, m/z 611.2, and m/z 624.2 for the 1:1 stoichiometric combination of UB-Zn(II) complexes, according to the mass fragmentation rule. [17] Similarly, the m/z 716.1 mass fragment was formed due to the 1:2 stoichiometry UB-Zn(II) complexes. By removing four, three, and two methyl ions, mass fragments of m/z 572.1, m/z 614.2, and m/z 628.2 were expected to have 1:1 stoichiometry of SB-Zn(II) complexes. Zn(II) complexation with SB produced a mass fragment of m/z 720.1 due to the 1:2 stoichiometry. Evidence of complexation was further confirmed by the removal of the NH stretching signal in FT-IR spectra. For molecular orbital TD-DFT calculations on the UB-Zn(II) complex, a rigorous benchmarking process suggested the use of the B3LYP hybrid functional and LANL2DZ basis set as the optimal combination. The B3LYP functional and LANL2DZ basis sets were utilized for FP-Zn(II) complexes of various zinc stochiometry geometry. The Benesi–Hildebrand plots and the ESI-MS analysis reveal a 1:1 predominant stoichiometry for FP-Zn(II) complexes. The endothermic enthalpy of FP–Zn(II) complexes involves the first disaggregation of higher FPs, followed by metal-ligand complexation. Furthermore, the correlation between the experimental and theoretical results of binding constant (K_a), absorbance, enthalpy,
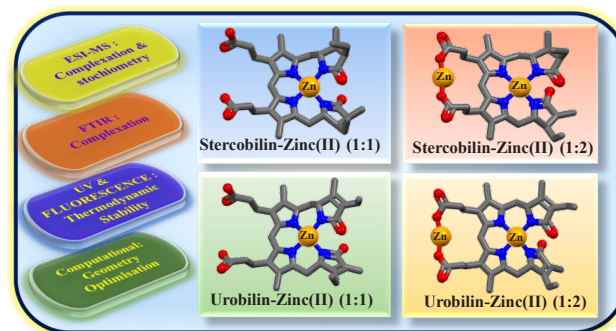

Fig 5: Graphical presentation of Complexation behaviour of faecal pigments-Zn(II) and its various possible stoichiometry, thermodynamics and computational studies (Ref: https://doi.org/10.1016/j.molstruc.2021.130440)

and vibrational studies provide the best molecular level insight towards FP–Zn(II) complexation.

3.4 Proposed fluorescence-based methods for highly sensitive detection of faecal pigments

(This work has been published in *Analytical Methods*[18])

Using a different approach, the aggregation-induced emission phenomenon of FPs was utilized for the enhancement of fluorescence, thereby increasing the detection sensitivity. This was done by using primary alcohols that are sparingly soluble in water. By taking water-immiscible aliphatic alcohols with increasing chain length, it is possible to extract relatively water-insoluble FPs to the alcohol layer. This can enhance the fluorescence of FPs in the alcohol layer due to the increase of the concentration of FPs in the layer. The fluorescence enhancement is also increased due to the increase in viscosity by increasing the chain length of primary alcohol.

The insolubility of FPs facilitates lower-order H-aggregation in the respective alcohol medium. Hence the fluorescence emission was observed for FPs in alcohol medium attributed to lower-order H-aggregation. When compared to the same concentration of FPs in an aqueous medium, the fluorescence intensity of FPs in 1-hexanol rises by 108-136 times. The steady-state emission at 518 nm and absorption at 506 nm of FPs increase upon increasing the viscosity of the alcohols. It is well known that the fluorescence emission intensity increases linearly with viscosity.[19-21] As expected, the emission spectrum of FPs at 518 nm of excitation 480 nm is regularly increased with the increase of viscosity of the solvents from methanol to 1-hexanol. The fluorescence intensity again decreases for 1-heptanol and 1-octanol. The aliphatic chain (hydrophobic group) increase in higher alcohol makes it
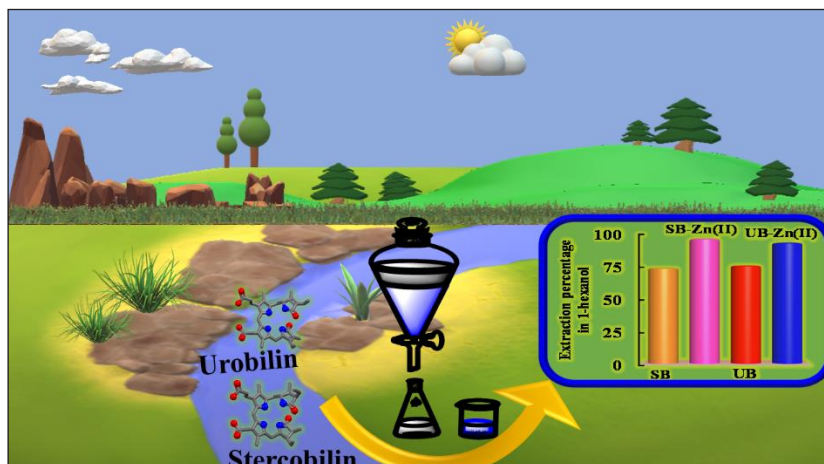

Fig 6: Graphical presentation of extraction based fluorometric method for faecal pigments analysis (Ref : https://doi.org/10.1039/D1AY01539G)

more hydrophobic (nonpolar in nature), which facilitates the high extraction efficiency due to the increase in solubility of FP-Zn(II) complexes. As a result, 1-hexanol is an excellent solvent for extracting FPs and FP-Zn(II) complexes. Fluorescence emission of FP-Zn(II) complexes after extraction by 1-hexanol has easily been detected at concentrations down to picomolar and sub picomolar concentrations. 1-hexanol has significantly less extraction affinity towards humic acid, which minimizes the interference of DOM's background fluorescence with FPs.

4. Conclusions

In summary, we have investigated the detailed photophysical studies of FPs and its zinc complex in the aqueous medium. The present study provides a deeper understanding of the photophysics and aggregation behaviour of FPs and FP-Zn(II) complexes in the aqueous media. This molecular-level understanding prompted us to develop fluorescence-based analytical methods for highly sensitive detection of FPs. This work also further opens enough scope for a fluorescence-based method (extraction as well as non-extraction based) for FP analysis.

Acknowledgement

References:

1. Rose, C.; Parker, A.; Jefferson, B.; Cartmell, E., The Characterization of Feces and Urine: A Review of the Literature to Inform Advanced Treatment Technology. *Crit Rev Environ Sci Technol*, *45* (17), 1827-1879 (2015).

2. Sato, H.; Hirose, T.; Kimura, T.; Moriyama, Y.; Nakashima, Y., Analysis of Malodorous Volatile Substances of Human Waste: Feces and Urine. *Journal of Health Science*, *47*, 8-19 *(*2001).

3. Kumar, V.; Gill, K. D., Qualitative Test for Bile Pigments and Urobilinogen in Urine. In *Basic Concepts in Clinical Biochemistry: A Practical Guide*, Kumar, V.; Gill, K. D., Eds. Springer Singapore: Singapore,; pp 123-127 (2018).

4. Bixler, J. N.; Cone, M. T.; Hokr, B. H.; Mason, J. D.; Figueroa, E.; Fry, E. S.; Yakovlev, V. V.; Scully, M. O., Ultrasensitive detection of waste products in water using fluorescence emission cavity-enhanced spectroscopy. *Proceedings of the National Academy of Sciences of the United States of America*, *111* (20), 7208-11 (2014).

5. Robertson, L. D.; Roper, D., 11 - Laboratory Methods Used in the Investigation of the Haemolytic Anaemias. In *Dacie and Lewis Practical Haematology (Twelfth Edition)*, Bain, B. J.; Bates, I.; Laffan, M. A., Eds. Elsevier.; pp 214-227 (2017).

6. Al-Shura, A. N., 5 - Hemoglobin. In *Advanced Hematology in Integrated Cardiovascular Chinese Medicine*, Al-Shura, A. N., Ed. Academic Press.; pp 27-32 (2020).

7. Orten, J. M., Metabolism of hemoglobin and bile pigments. *Annals of clinical laboratory science*, *1* (2), 113-24 (1971).

8. Bala, M.; Sharma, A.; Sharma, G., Assessment of heavy metals in faecal pellets of blue rock pigeon from rural and industrial environment in India. *Environmental Science and Pollution Research*, *27* (35), 43646-43655 (2020).

9. Jones-Lepp, T. L., Chemical markers of human waste contamination: Analysis of urobilin and pharmaceuticals in source waters. *Journal of Environmental Monitoring*, *8* (4), 472-478 (2006).

10. Organization, W. H., Drinking water fact sheet., *https://www.who.int/news-room/fact-sheets /detail/drinking-water.* (2018).

11. Rudolph, H. L.; Sekera, E. R.; Wood, T. D., Stable (18) O-labeling method for stercobilin and other bilins for metabolomics. *Rapid communications in mass spectrometry : RCM*, *30* (13), 1469-1474 (2016).

12. Waso, M.; Ndlovu, T.; Dobrowsky, P. H.; Khan, S.; Khan, W., Presence of microbial and chemical source tracking markers in roof-harvested rainwater and catchment systems for the detection of fecal contamination. *Environmental Science and Pollution Research*, *23* (17), 16987-17001 (2016).

13. Prakash, S.; Mishra, A. K., Stercobilin and Urobilin in Aqueous Media: Existence of Specific H-Aggregates and Nonspecific Higher Aggregates at Different Concentrations. *J Phys Chem A*, *124* (48), 10053-10065 *(*2020).

14. Verma, P.; Pal, H., Intriguing H-Aggregate and H-Dimer Formation of Coumarin-481 Dye in Aqueous Solution As Evidenced from Photophysical Studies. *The Journal of Physical Chemistry A*, *116* (18), 4473-4484 (2012).

15. Prakash, S.; Panigrahi, S. K.; Dorner, R. P.; Wagner, M.; Schmidt, W.; Mishra, A. K., Understanding the photophysics of stercobilin-Zn(II) and urobilin-Zn(II) complexes towards faecal pigment analysis. *Chemosphere*, *265*, 129189 (2021).

16. Prakash, S.; Banu, S.; Mishra, A. K., The Structure and Stability of Faecal Pigment-Zinc(II) Complexes. *Journal of Molecular Structure*, 130440 *(*2021).

17. Weissberg, A.; Dagan, S., Interpretation of ESI(+)-MS-MS spectra—Towards the identification of "unknowns". *International Journal of Mass Spectrometry* **2011,** *299* (2), 158-168.

18. Prakash, S.; Mishra, A. K., Photophysics of faecal pigments stercobilin and urobilin in aliphatic alcohols: introduction of a sensitive method for their detection using solvent phase extraction and fluorometry. *Analytical Methods* *(*2021).

19. Hong, Y.; Lam, J. W. Y.; Tang, B. Z., Aggregation-induced emission: phenomenon, mechanism and applications. *Chemical communications*, (29), 4332-4353 (2009).

20. Yan, W.; Long, G.; Yang, X.; Chen, Y., Synthesis and aggregation-induced fluorescence emission properties of boron-containing derivatives that respond to viscous alcohols. *New Journal of Chemistry*, *38* (12), 6088-6094 *(*2014).

21. Vyšniauskas, A.; Ding, D.; Qurashi, M.; Boczarow, I.; Balaz, M.; Anderson, H. L.; Kuimova, M. K., Tuning the Sensitivity of Fluorescent Porphyrin Dimers to Viscosity and Temperature. *Chemistry – A European Journal*, *23* (46), 11001-11010 (2017).

Prof. Ashok Kumar Mishra *completed his PhD from IIT Kanpur in 1985. After a stint in Sambalpur University as a faculty member, and in Gunma University (Japan) as a Monbusho Fellow, he joined Indian Institute of Technology Madras in 1992. He was a JSPS Visiting Scientist in Gunma University, Japan during 2002-2003. He has around 220 research papers/monographs/reviews. Currently, he works as an Institute Chair Professor in the Department of Chemistry of IIT Madras.*

Dr. Swayam Prakash *completed his master from NIT Rourkela and PhD from IIT Madras in 2021. Currently he works as postdoctoral fellow at IIT Bombay. His research interest is understanding the photophysics of faecal pigments and the development of fluorescence based analytical methods towards increase their detection of sensitivity.*

An Overview of Fluorophores for Sub-cellular Imaging

Tarushyam Mukherjee and Sriram Kanvah*

Department of Chemistry, Indian Institute of Technology Gandhinagar Palaj Gandhinagar 382355
Email: sriram@iitgn.ac.in

Abstract

Development of novel fluorophores to analyse the mysteries of microscopic cellular world has gained tremendous interest. Often, the organelles rapidly change and reorganize within the cellular compartments in response to the physiological requirements and internal environment. There are well-established fluorescent protein markers designed specifically to image such cellular changes and organelles. However, visualization with small organic molecules brings in great versatility. The incorporation of suitable substituents not only enables specific targeting of organelles but also enables detection of biological analytes and physiological processes, if any. In this report we briefly summarize the design strategies involved and some of our recent results in this research domain.

Introduction

The cell is the unit of life, and its various compartments play a crucial role in significantly influencing its overall activity. An eukaryotic cell can be sub-sectioned in three parts; a. plasma membrane, b. cytoplasm, c. nucleus (Figure 1). The plasma membrane, a semipermeable membrane, is composed of lipid bilayer with phospholipids, cholesterol, integral, peripheral membrane proteins, and other small signalling molecules.[1-3] The cytoplasm, on the other hand, holds a broad class of various membrane-bound (mitochondria, Golgi complex, endoplasmic reticulum, lysosome and others) and unbound organelles (centriole, ribosomes). Each organelle

Figure 1 Typical compartments of a eukaryotic cell

possesses a unique role to regulate the overall metabolic homeostasis of the cell and maintain their dynamics and retain specific connections with one another to keep the cell working, which otherwise leads to detrimental physiological consequences.[4]

Cell Imaging and Significance of Fluorescence Labelling

To evaluate the intracellular dynamics and the general cellular physiology, fluorescent cellular probes have emerged in the past few years, as can be understood by the recent research reports for the period between 1980-2020 (Figure 2).

Several imaging modalities such as radioactive trace elements based (PET imaging) [5-7] and a large family of fluorescent markers have been developed by scientists around the globe to tag specific regions of interest in a cell. The history of fluorescent molecules dated back to 1845 with the discovery of naturally occurring fluorescent small molecule quinine. Since then the fluorescent tagging methods have become a popular technique amongst biologists and chemists to probe cellular processes with the award of Nobel Prizes in 2008 for the discovery of GFP and[8] development of super-resolution
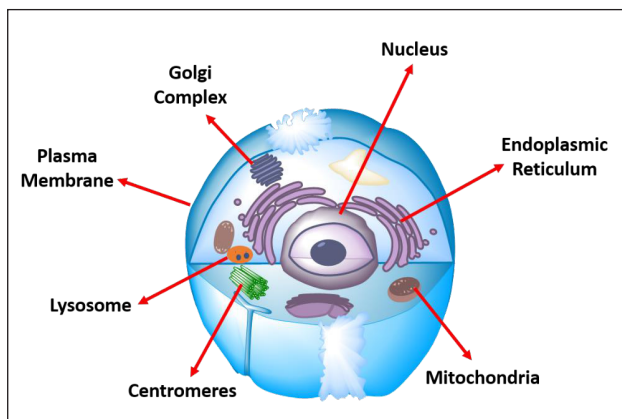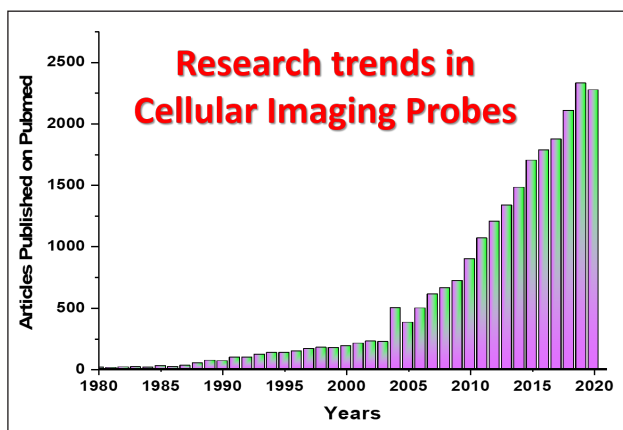
Figure 2 Recent research trends in Cellular Imaging Probes (a summary of the number of articles published in Pubmed from 1980-2020)

fluorescence microscopy in 2014 [9, 10].

Classification of Fluorophores

The fluorescent tagging methodologies for cellular imaging can be broadly classified as a). intrinsic fluorophores (genetically modified fluorescent proteins or naturally known fluorophores) and b). extrinsic (use of non-

biological origin compounds) fluorophores. The genetically modified fluorescent marker for the tagging of organelles had limitations such as limited colour chemistry, tedious process of tagging, alteration of native protein's functionality, heterogeneous expression profile depending on the cell types, and weaker photostability.[11] The extrinsic fluorophores like organic fluorescent molecules provided extra leverage based on their flexibility to achieve superior photostability and broader colour range. Also, these fluorophores enabled the detection and monitoring of biologically relevant analytes in the cellular milieu[12] and contributed to the development of a, extensive library of fluorescent molecules. Figure-3 highlights the use of some fluorescent probes emitting at different wavelengths. The molecular architecture design aims are based on improved photo stability, enhanced brightness and different emission spectral profiles. Representative fluorophores such as as cyanine dyes, fluorescein, BODIPY, styrylpyridinium dyes, naphthalene, coumarin ,
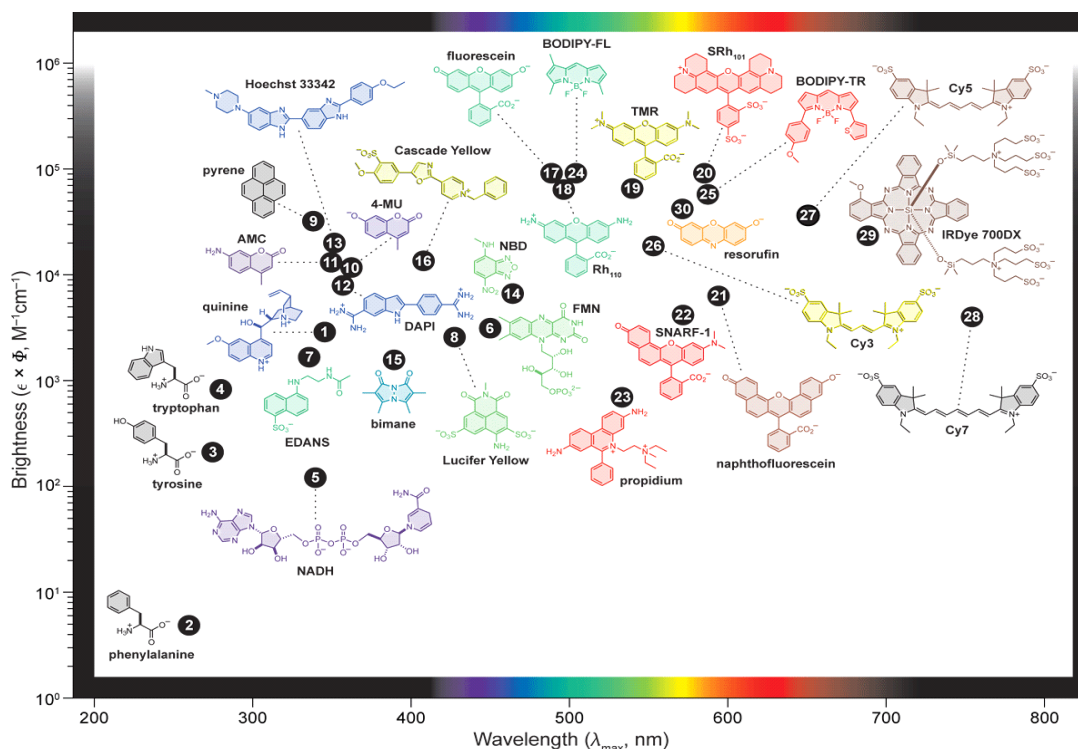

Figure 3 Plot for brightness and wavelength of various fluorophores (Adapted with permission from ref[13] Copyright (2008) American Chemical Society

fluorescent aminoacid derivatives are shown in Figure 3[13]. These multivariant derivatives are extensively used in several applications, notably organelle imaging, nucleic acid binding studies, protein receptor tagging, developing fluorescent bio-conjugates, metal ion sensing, molecular switches, analyte sensors, etc. Recent efforts have been concentrated towards developing newer fluorophores to far-red wavelength with enhanced target specificity. The red-emitting fluorophores have a significant impact on cellular imaging because of their deep tissue penetration and avoid cellular autofluorescence[14-16]. In addition, lower phototoxicity to the cells because of the longer wavelength makes these probes amenable for longer-duration live cell imaging[17].

Cell Organelle Imaging

Cellular organelles are specialized lipid membrane-bound compartments that play specific functions to maintain cellular homeostasis.

To visualize these specialized compartments, extrinsic fluorophores have been used extensively during the last decade[18]. Organic fluorophores, amongst this wide variety, were proven to be an important chemical biology tools for the imaging organelles. The synthetic feasibility and tunability of spectral properties make them one of the most desirable groups of fluorescent organelle probes. The fluorescent probes are mainly conjugated with various organelle recognition moieties to target the regions under the crowded cellular environment. In the following sections, we briefly describe the designing strategy, the available probes, and the applications of the fluorescent organelle probes for different compartments of cells with particular attention to the plasma membrane and mitochondrial probes.

Cellular Membrane Probes

The mammalian cell membrane is primarily composed of phospholipid bilayers, several lipids, proteins, and other small signalling
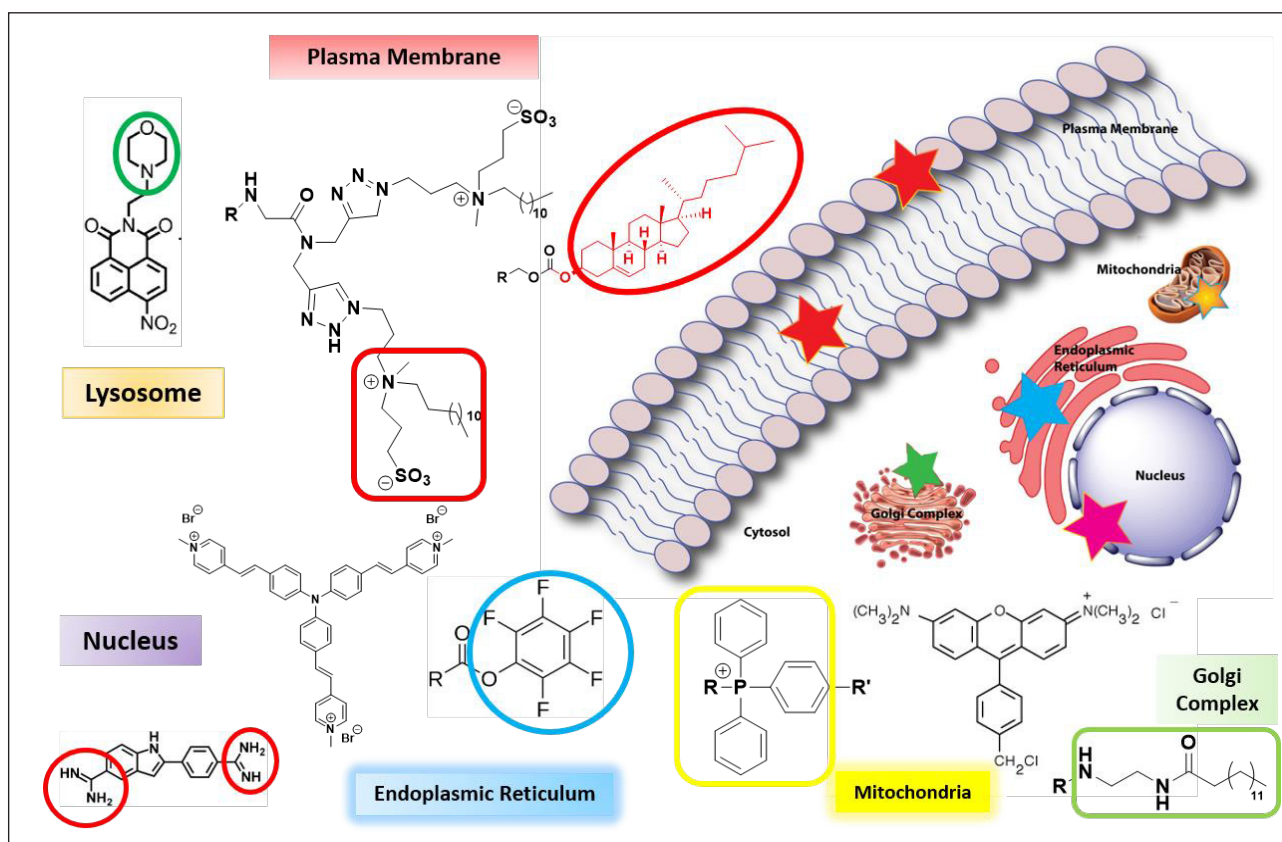

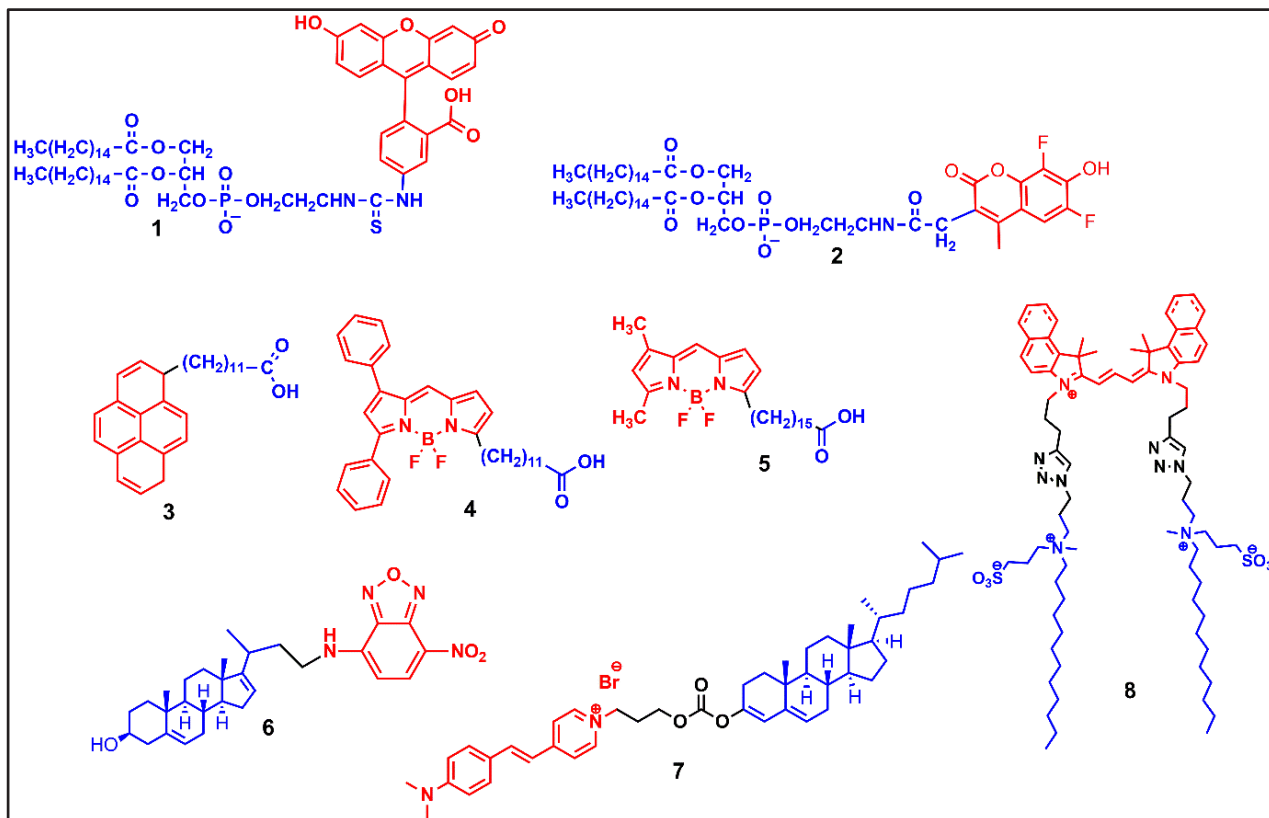*Figure 4 Summary of Fluorescent Organelle markers*

Figure 5 Some known Plasma membrane probes. In general, many of these probes have lipid or alkyl chains for efficient labelling.

molecules. Plasma membrane, apart from acting as a functional cell barrier, also plays a significant role in other cellular processes such as uptake of foreign materials, neuronal communication, muscle contraction, and cell trafficking[19]. The popular extrinsic cell membrane probes are majorly designed to target the cell membrane lipids (fatty acid and cholesterol analogues) and constitute three major approaches (Figure 5);

    a. fluorescent phospholipid analogues,

    b. fluorescent steroid (cholesterol) analogues

    c. fluorescent probes with longer alkyl chains

    A wide variety of fluorescent substrates that were used are BODIPY,[20] nitrobenzoxadiazole (NBD),[21, 22] pyrene, [23] carbocyanine probes, styrylpyridines,[24] dansyl,[25] cyanines[26]. Apart from investigating the general physiology of the cell, these probes are also used to study the membrane fusion, lipid-diffusion, lipid-protein interaction in microbial infection, characterization of lipid domains, long-term cell imaging, cellular uptake studies in cancer cells.[19, 27] In addition to the simples fluorescent labelling of the plasma membrane, the multi-faceted chemical dynamics of the plasma membrane also inspired the researchers to design newer probes for monitoring specific cellular processes. The class of fluorophores not only accumulate in the membrane for staining but also are responsive to precise monitoring of the specific biomolecule and their dynamics. The readout is recorded through fluorescence turn-on/off state changes or by ratiometric changes in channel intensity while imaging.

Mitochondrial Probes

    Mitochondrion, the membrane bound organelle is the hotspot of oxidative phosphorylation and is responsible for ATP
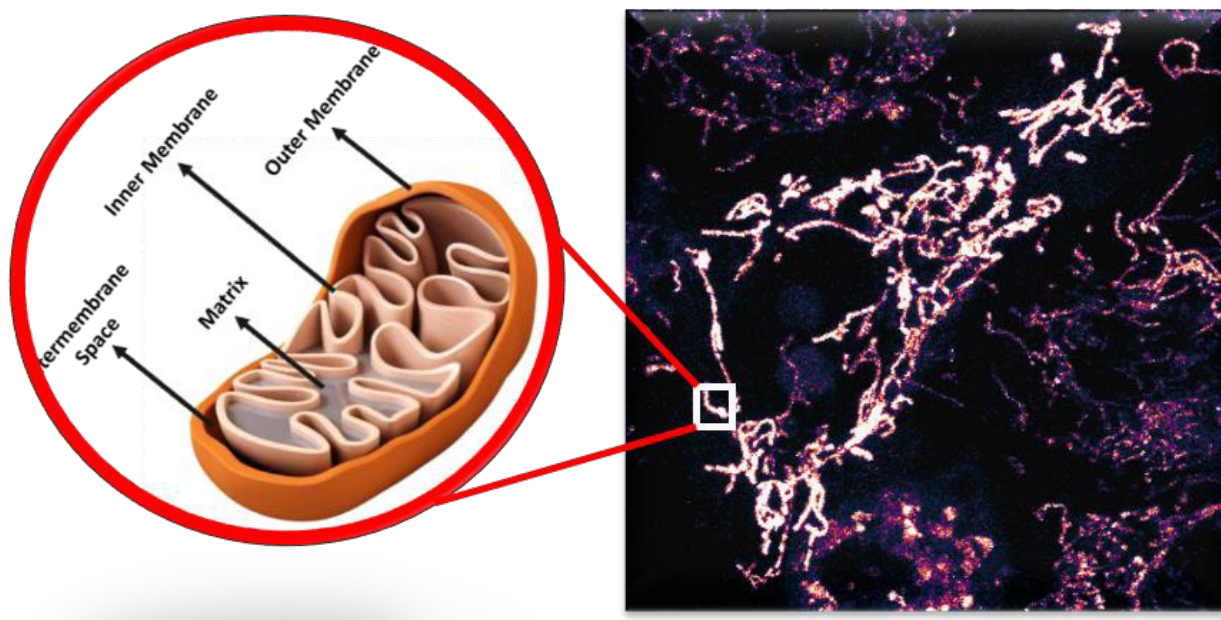
Figure 6 Mitochondrial morphology (Microscopic image and general physiology)

generation in cells. Apart from generating ATP, mitochondrion also plays a pivotal role in maintaining cellular ROS levels, controlling apoptosis, steroid biogenesis, intracellular Ca^{2+} balance, and many more. Therefore, visualizing mitochondria help us to monitor cellular abnormality and other physiological consequences. Traditionally the cationic organic fluorophores have been used for targeting mitochondria. The scientists exploited the main features of the phospholipid bilayer membrane electronegative potential of the mitochondrial inner membrane to achieve mitochondrial localization. The lipophilic nature of the molecular architecture gives the flexibility to target the phospholipid membrane layer of the mitochondrial outer membrane. The mitochondrial outer membrane mimics the plasma membrane in its phospholipid vs. protein ratio (1:1) and is rich in integral proteins. In contrast, the phospholipid to protein ratio is only 1:3 on the inner membrane[28]. Hence a cationic lipophilic molecule transit through the outer membrane based on the lipophilicity and gets entry to the mitochondrial matrix after it passes through the negative potential of the inner membrane.

The initial surge in investigating the mitochondrial membrane potential also keeps the proton motive force active to synthesize ATP involves some of the cationic dyes. Almost a century ago, the Lewis et al.'s demonstrated the specificity of cationic Janus green dye for mitochondrial imaging.[29] A few other vital probes like fuschin, crystal violet were used by histologists to stain mitochondria, followed by the development of Rhodamine 123 almost 60 years later..[30] Subsequently, a plethora of fluorescent molecules were reported in the last decade to image mitochondria. The basic architectures like pyridinium cation,[31, 32] triphenyl phosphonium moieties[33] were designed for achieving mitochondria-specific imaging.

Delocalized lipophilic cations (DLC) have been extensively utilized in targeting the mitochondria. In particular, triphenyl phosphonium (TPP) moiety handle covalently linked with organic fluorophores and drugs is well known to localize in mitochondria.[34, 35]
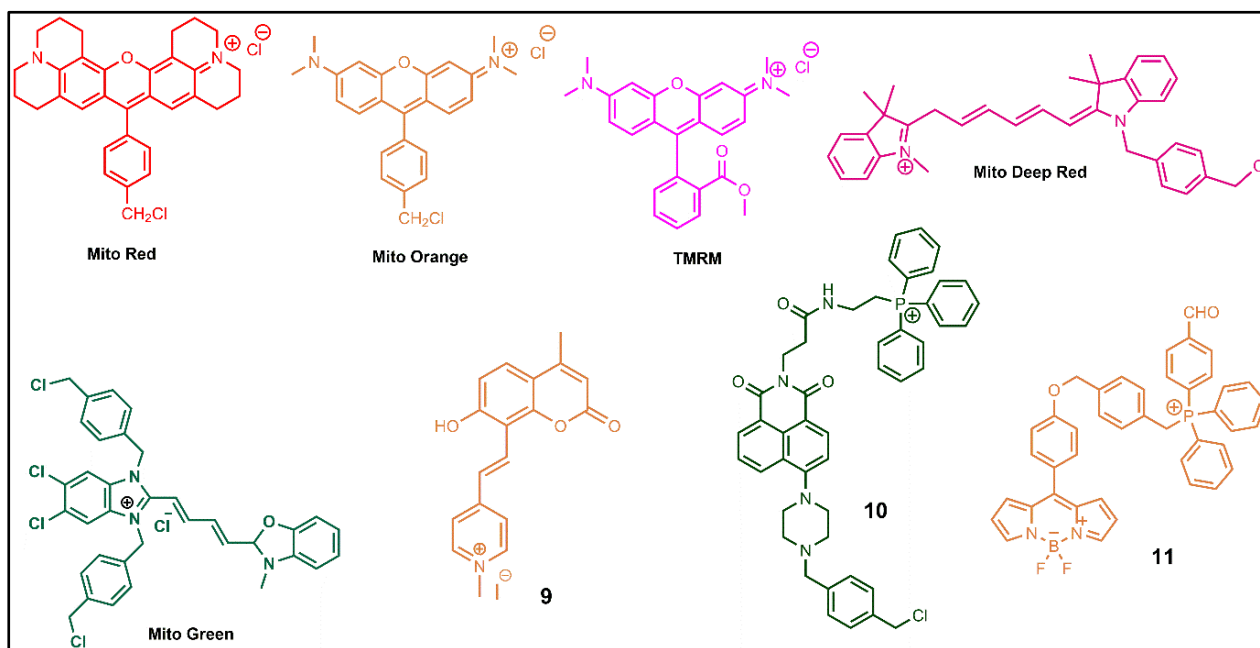
Figure 7 A few known Mitochondrial probes bearing cationic moieties

TPP conjugated molecules were also used to deliver antioxidants, nanoparticles, liposomes, and pharmacophores to the mitochondria of cells[36]. Together with the lipophilicity and cationic nature, the TPP conjugated molecules selectively target the mitochondria. The presence of the cationic charge on the molecular structure helps the delocalization of this charge through resonance stabilization, and since the charge is spread over a sizeable molecular area, it helps to form a greater ionic radius. Furthermore, with the help of the Nernst equation, we can predict the transport efficiency of delocalized lipophilic cationic molecular structures across the membranes of net electronegative potential. They tend to get accumulated within the cell cytoplasm because of electronegative potential of -60 mV plasma membrane. But after crossing the plasma membrane's barrier, in order to target cellular organelles, they accumulate more to the mitochondrial matrix due to the mitochondrial membrane potentials (~-180 mV) by ~1000 fold more binding efficiency than the other regions[37]. Despite their wide usage, the DLC conjugated molecules also showed a high toxicity level at the higher concentrations[38]. Their functionality of binding to the mitochondrial membrane and, altering ATP synthesizing activity or destabilization of the membrane potential made the research community look for new class of probes[30].

Cationic Pyridinium derivatives were also investigated for mitochondria specific imaging, and it possesses several advantages over traditional TPPs use as DLC. In a D-π-A system of the fluorophore, the presence of pyridinium enables robust optical properties with tunable emission ranges depending on the strength of the electron-donating groups. The emission in the red region is always desirable from an imaging perspective because of lower autofluorescence, lower cytotoxicity, and deep tissue penetration[38]. Apart from its role as an auxochrome, pyridinium probes also have an affinity for the electronegative potential of the mitochondrial inner membrane[39, 40].

Other Cell Compartmental Probes

Apart from the plasma membrane and mitochondria, other important cell organelles contribute significantly to the overall cellular function and morphology. The membrane-bound
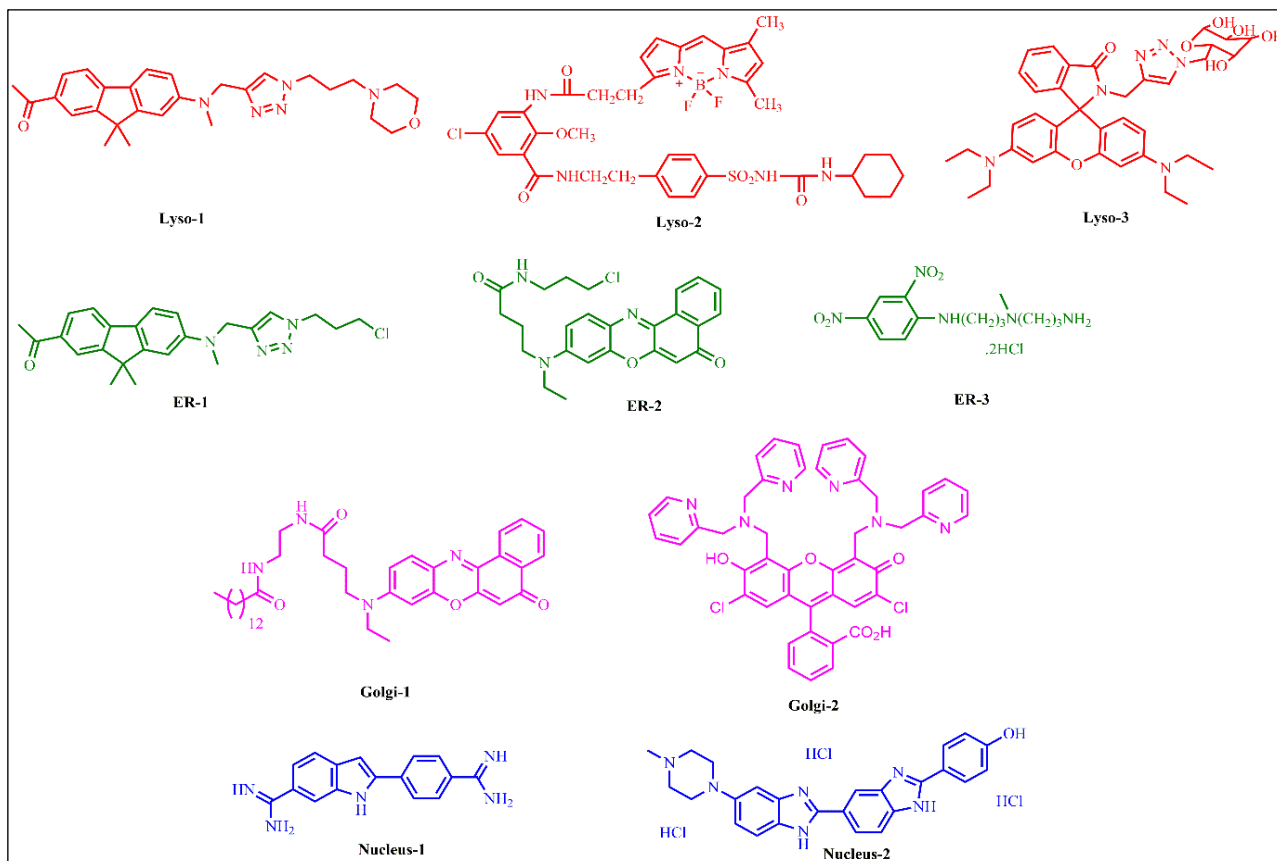
Figure 8 Structures of a few Organelle Probes

organelles such as lysosome, Golgi apparatus, endoplasmic reticulum, lipid droplets, and nucleus are majorly targeted by the organic fluorophores. A summary of chemical moieties responsible for directing a molecule's localization in a specific organelle has been described (Figure 4).

Lysosome specific probes

The lysosome is the main digestive compartment of the cell. It contains several hydrolysing enzymes, and the optimum pH inside the lysosome is under 6 because of the high proton concentration.[41, 42] Hence lysosomal imaging and sensing analytes inside this organelle gained research attraction in the last few years. One of the main approaches to target lysosome specifically by attaching chemical moieties a. that have slightly basic pKa values (such as morpholine, piperazine, etc.) and these

undergo protonation under the acidic vesicle as lysosome (Figure 4)[43]. This method of attaching weak bases to an already existing lipophilic unit helps the moieties to be specifically trapped in lysosomes and this phenomenon is typically known as 'lysosomotropic' effect. Therefore, the protonated probes get fixed inside the membrane-bound organelle and cannot escape the organelle. A series of lysosomal probes emitting at different emission spectral ranges have been reported by conjugating these probes with a weak basic moiety (Figure 8). Several biological analytes such as Zn^{2+},[44] thiols[45] and H_2O_2 [46] have also been measured by using these probes. However, a few lysosomal probes show 'alkanizing effect', limiting their use for prolonged incubation live-cell imaging[38]. Therefore, an upsurge in the development of lysosomal probes that can label lysosomes without the pH dependence is grabbing the community's attention.

ER & Golgi specific probes

The endoplasmic reticulum and Golgi apparatus are primarily involved in the sorting of lipid and proteins. Hence, attaching a longer fatty acid chain of various kinds (e.g., sphingolipids) helps the probe better localize at those sites[47-49]. Reports suggests use of pentafluorophenyl pendant and chloride ions direct the probes for targeting the ER.[50] Some of the widely used ER and Golgi markers are shown in Figure 8.

Nuclear probes

The nucleus, the storage compartment of genetic materials, plays a significant role in controlling gene expression and maintaining cellular integrity. The primary content of DNA (deoxyribonucleic acid), RNA (ribonucleic acid), and histone proteins are targeted for developing nuclear dyes. Some of the famous DNA binding dyes are DAPI and Hoechst.[51, 52] While these are being used significantly in the commercial market, but they suffer from the requirement of excitation in the UV region. [38] Hence there is a steep increase in the emergence of new nucleus targeting DNA binders of red emitting probes. One of the popular RNA binders is SYTO-RNA select[53] which is also commercially available for nuclear staining of red emitting group but suffers from photostability issues.

Summarized results from our recent research

Considering the overall importance of the work, we have recentlyexplored the designs to visualize the cellular organelles and to analyze the mysteries of the microscopic cellular world. Often, the organelles rapidly change and reorganize within the cellular compartments in response to the physiological requirements and internal environment. There is well-established fluorescent protein markers explicitly designed for this purpose. However, visualization with small organic molecules brings in great versatility. The incorporation of suitable substituents enables the specific targeting of organelles and the detection of biological analytes. In our research study, we opted to tailor the traditional D-π-A stilbene scaffold or use established markers to visualize sub-cellular organelles such as the mitochondria, lipid droplets, nucleolus, and the plasma membrane. We attempted to study tracking of the live-cell mitochondrial dynamics, mapping mitochondrial viscosity, development of stress-responsive probes for mitochondrial imaging, and imaging of lipid droplets. Summarized results from our recent works are shown below.

Imaging mitochondria and Plasma membrane in live cells using Solvatochromic styrylpyridines

We used two designs to achieve the desired target of sub-cellular localization. i). Small organic fluorophores bearing donor and acceptor groups exhibiting solvatochromic behaviour and their bioconjugates and ii). Conjugating known organic fluorophores with biologically relevant substrates. In the first approach, we designed and synthesized three styrene derivatives (**1-3**) and a cholesterol conjugate (**4**) [Fig-9]. Styrene has neutral pyridine, styrenes 2 and 3 have pyridinium moiety and styrene **4** has a cholesterol tether. The fluorophores bearing a donor (dimethylamino group) and an acceptor (pyridine or pyridinium) show moderate to strong solvatochromic emission attributed to intramolecular charge transfer. Examination of these compounds in cellular domain reveals interesting results[54]. Styrene-**1** is non-specific while styrenes **2** and **3** show strong mitochondrial localization. However, the lipid conjugated styrene **4** labels plasma membrane effectively and show minimum cytotoxicity in Live neuronal (N2a) and non-neuronal (HeLa) mammalian cell lines. Furthermore, we could successful track mitochondrial dynamics using Styrene -**3.** This strategy of using a D-π-A scaffold and relevant substitutions could be ideal in generating a variety of fluorophores targeting other subcellular compartments or study cellular processes such as viscosity or determine various analytes.
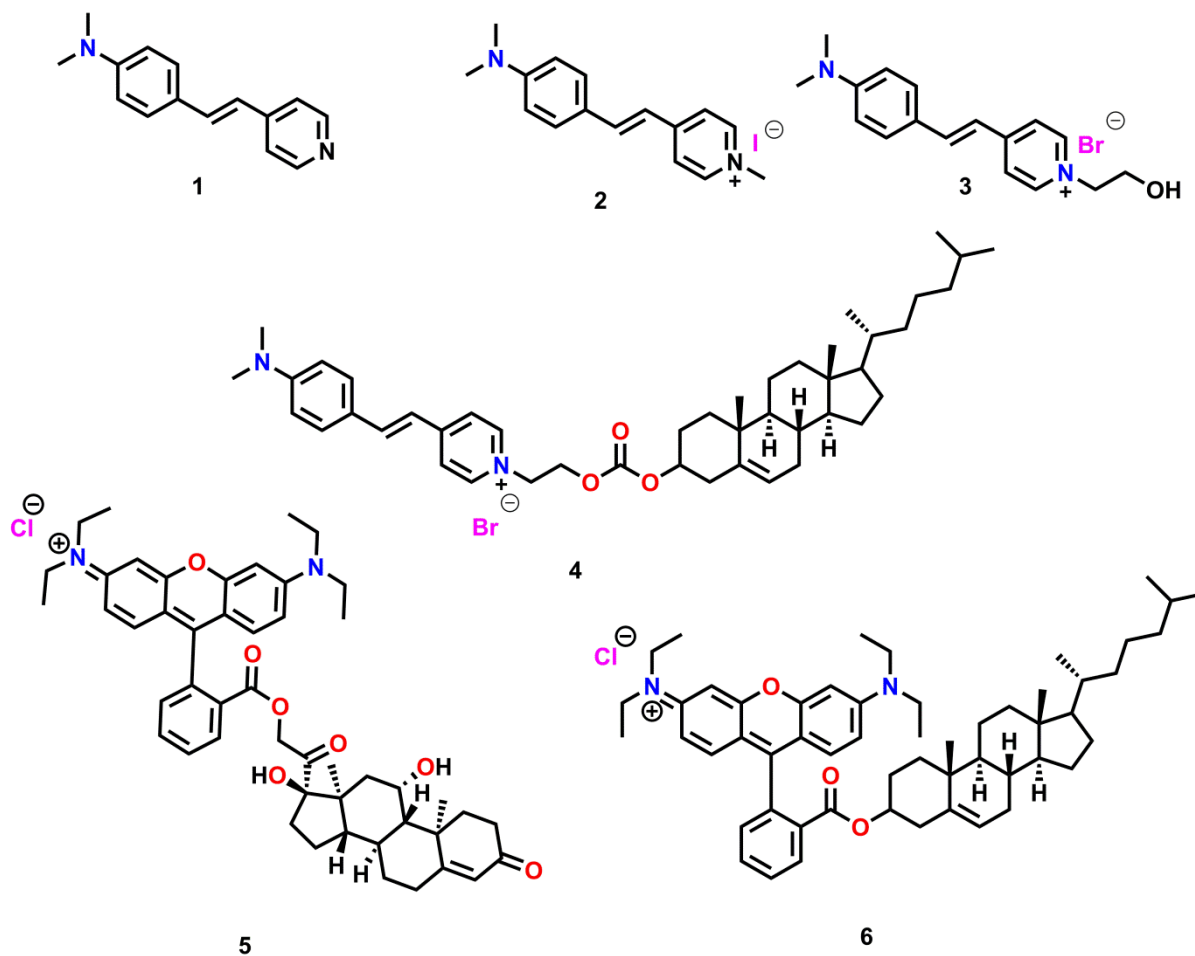
Fig 9: Structures of molecules synthesized for sub-cellular imaging in our research group.

Live-cell imaging of the nucleolus and mapping mitochondrial viscosity with a dual function fluorescent probe

Using Styrene scaffolds (**1-4**) we were successful in imaging the sub-cellular organelles. Our next goal was to deep prober to image the mitochondria as well study the mitochondria viscosity. For this, we designed styrene-**5** bearing a julolidine scaffold[55]. Styrene **5** is also characterized by a pyridinium group and a cyanovinyl spacer. The design is based on the 9-(2,2-Dicyanovinyl)julolidine (DCVJ) an excellent viscosity sensitive dye. One of the cyano groups in DCVJ dye was replaced by a prydinium moiety. The presence of strong donor and acceptor yields a solvatochromic behaviour with emission at 600 nm in the red region. The fluorescence microscopy studies with the styrene (**5**) reveal not only the imaging of mitochondria but also of the nucleolus. We further demonstrated tracking of mitochondria along with measurement of the mitochondrial viscosity in live cells.

Stress Responsive Rhodamine-Bioconjugates for Membrane Potential Independent Mitochondrial Imaging and Tracking.

With the success of sub-cellular localization and probing of physiological parameters such as viscosity, we ventured further to use known chromophores and tag it to biomolecules for visualization of
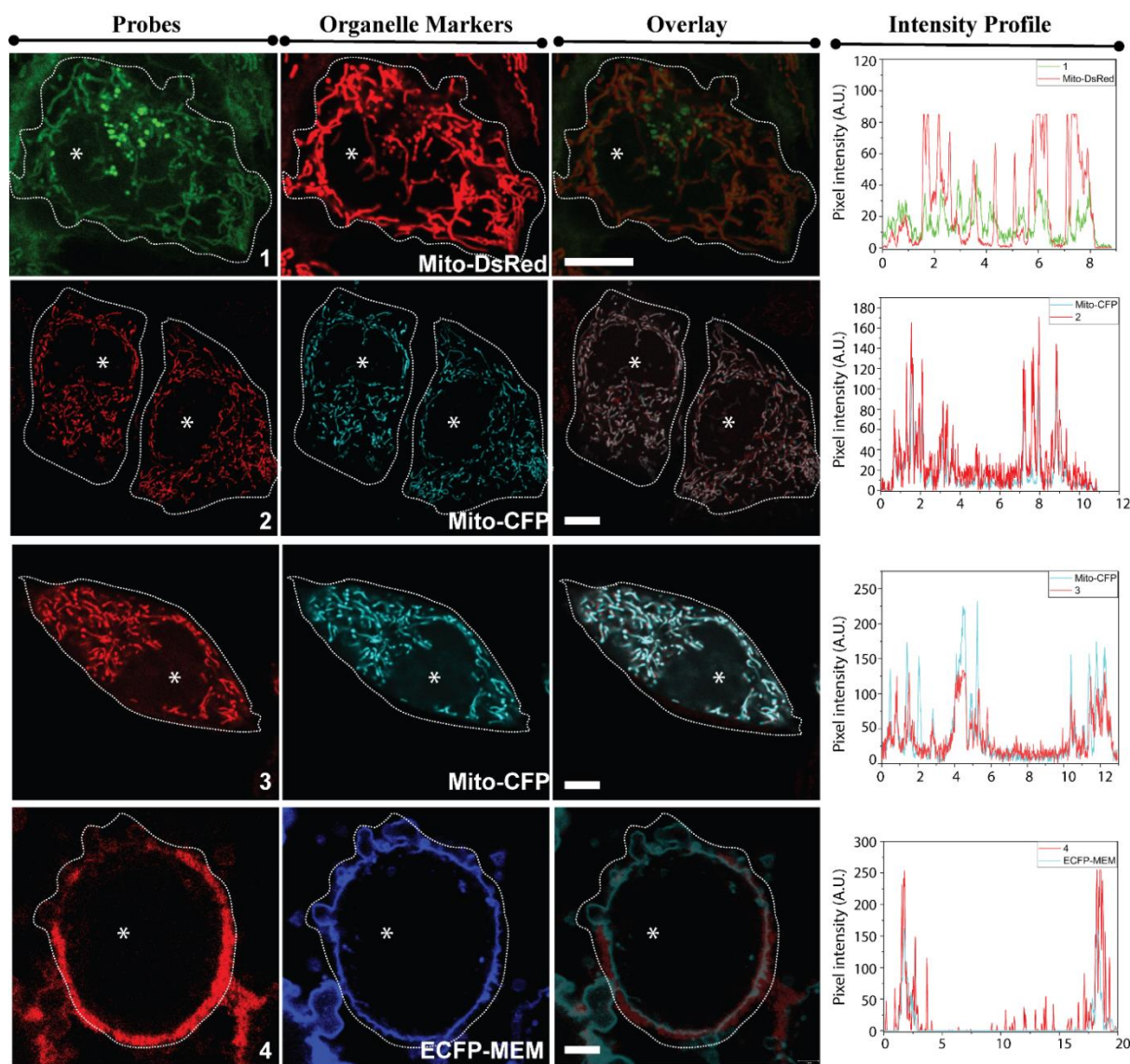
Figure 10 Labeling of subcellular compartments with styrenes in HeLa cells. Styrenes (1–4, extreme left panel; 1 µM of each styrene) were incubated with HeLa cells expressing fluorescent protein (FP)-tagged organelle-specific markers (second panel from left) and overlaid (third panel from left). Representative images of cells incubated with (A-C) Styrene 1 (E-G) Styrene 2 (I–K) Styrene 3, and (M-O) Styrene 4. (D, H, L and P) represent the intensity profile of line drawn in the ROI shown in inset images of respective styrenes (extreme right panel). Dotted yellow lines indicate the outline of transfected cells; white asterisks indicate nuclei. (scale bars, 10 µm)

sub-cellular organelles. We synthesised compounds 6 and 7 where in rhodamine B was modified with biomolecules such as cholesterol and cortisol. Both the probes showed excellent localization in the mitochondria with high brightness and enhanced SNR (signal-to-noise ratio) to the commercial MitoTracker Green probe. Importantly, the cortisol analogue was also utilized to study the stress response inside mitochondria[56]. We are currently looking at other similar sterol markers for understanding the cellular response and function.
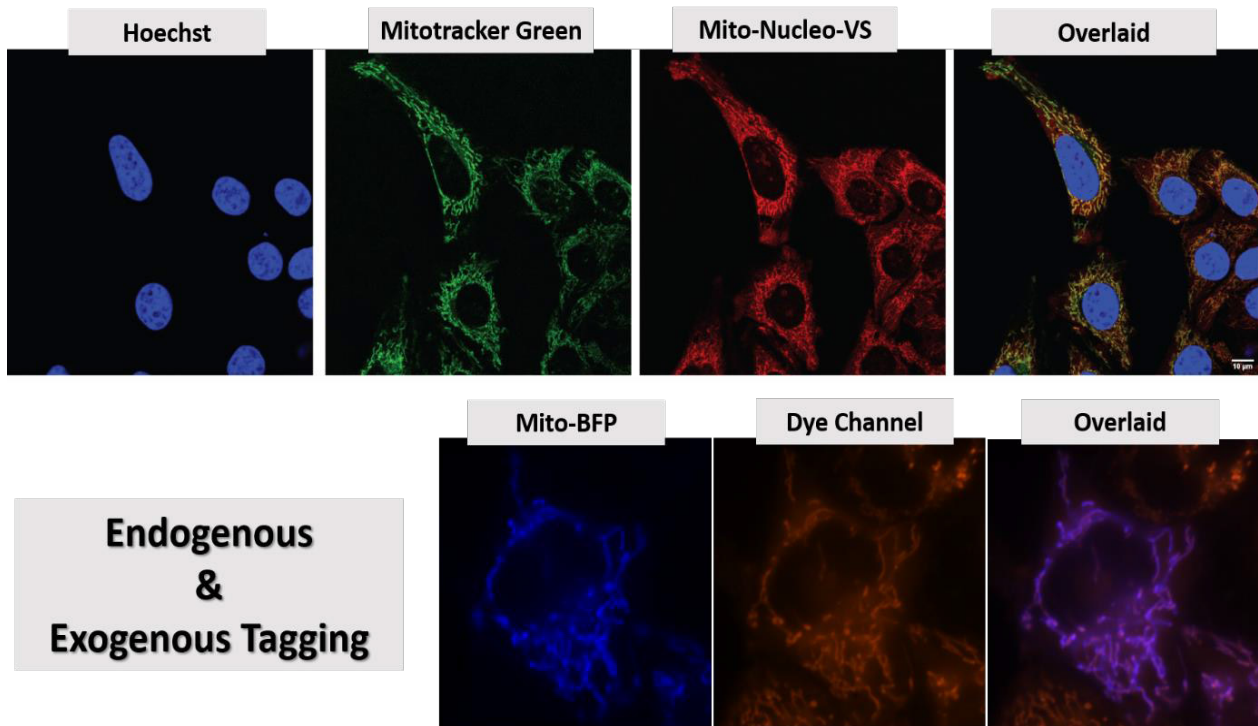
*Figure **11** Colocalization of the probe (Mito-Nucleo-VS) with exogenous (Mitotracker Green™) and endogenous (Mito-BFP plasmid). Scale factor: 10 μm. Hoechst is used to mark the nucleus of the cell.*
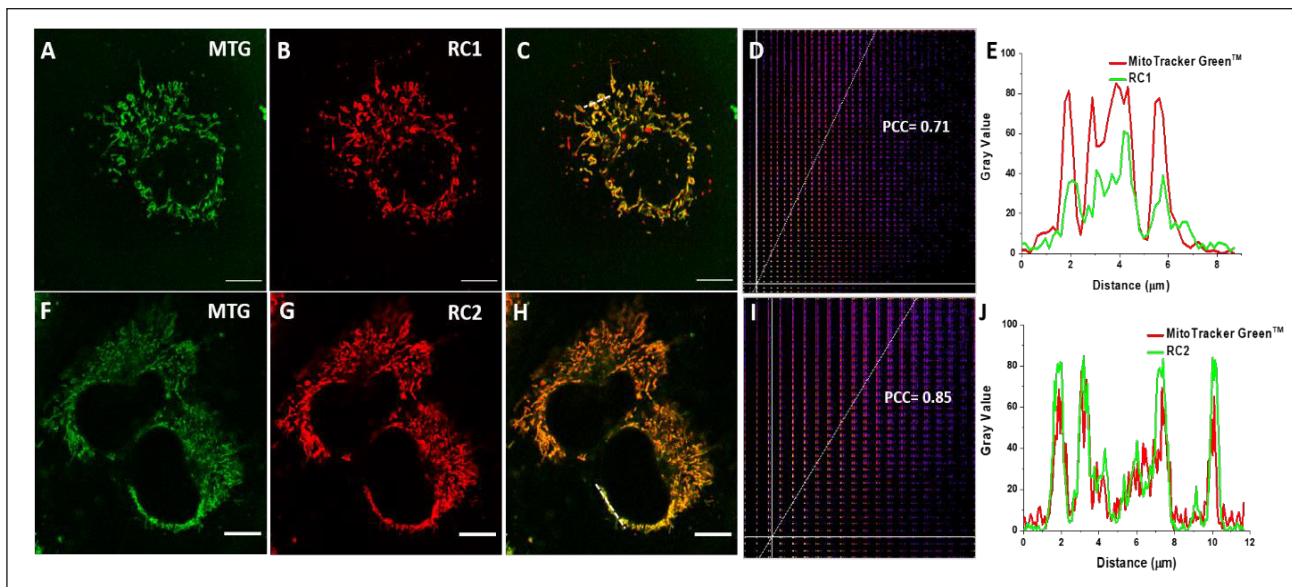
Figure 12 Colocalization of RC1 and RC2 with MitoTracker Green™ (MTG): (A) and (F) MTG, (B) RC1, and (G) RC2; (C) and (H) the corresponding overlaid channels; (D) and (I) the cytofluorograms of the respective colocalized images of the two different channels; and (E) and (J) the line profiles of the white lines drawn in the overlaid channels to describe the overlapping signal intensities of both the channels. RC1 & RC2 were excited by a 561 nm laser, emission channel: 570–630 nm; MitoTracker Green™ was excited by a 488 nm laser, emission channel: 500–550 nm. The signals were collected in a HyD detector in sequential imaging mode. Imaging was performed at 37 °C with 5% CO2 using a live cell apparatus module. The probe concentration used was 200 nM. Scale bar: 10 μm

Conclusions and Future Outlook

Although we were able to answer the initial questions of imaging, a lot of scope lies in translating our research from 'bench to bed side'.

A. Developing multi-photon excitable probes for deeper tissue penetration and mitigate the photo-toxicity problem in live samples

B. Testing of the probes with tissue specific sampling and real time distribution of probes in animal system by monitoring the animal in whole body imaging system.

C. Tweaking the side arm modifications of the probes to make the systems more sensitive in evaluating disease models both at cellular and tissue level

D. Analyse and investigate detailed cellular pathways by developing some of the organelle probes to protein specific targeting.

The research is currently ongoing in our laboratory

References

1. K. Simons, J.L. Sampaio, Membrane organization and lipid rafts, Cold Spring Harb Perspect Biol, 3 (2011) a004697.
2. T. Harayama, H. Riezman, Understanding the diversity of membrane lipid composition, Nat Rev Mol Cell Biol, 19 (2018) 281-296.
3. F.M. Goni, The basic structure and dynamics of cell membranes: an update of the Singer-Nicolson model, Biochim Biophys Acta, 1838 (2014) 1467-1476.
4. R. Inagi, The Implication of Organelle Cross Talk in AKI, Nephron, 144 (2020) 634-637.
5. T.S. Stutvoet, E.L. van der Veen, A. Kol, I.F. Antunes, E.F.J. de Vries, G.A.P. Hospers, E.G.E. de Vries, S. de Jong, M.N. Lub-de Hooge, Molecular Imaging of PD-L1 Expression and Dynamics with the Adnectin-Based PET Tracer (18) F-BMS-986192, J Nucl Med, 61 (2020) 1839-1844.
6. Y. Kurebayashi, P.L. Choyke, N. Sato, Imaging of cell-based therapy using (89)Zr-oxine ex vivo cell labeling for positron emission tomography, Nanotheranostics, 5 (2021) 27-35.
7. L. Wu, Y. Wang, M. Weber, L. Liu, A.C. Sedgwick, S.D. Bull, C. Huang, T.D. James, ESIPT-based ratiometric fluorescence probe for the intracellular imaging of peroxynitrite, Chemical Communications, 54 (2018) 9953-9956.
8. M. Chalfie, Y. Tu, G. Euskirchen, W.W. Ward, D.C. Prasher, Green fluorescent protein as a marker for gene expression, Science, 263 (1994) 802-805.
9. E. Betzig, R.J. Chichester, Single molecules observed by near-field scanning optical microscopy, Science, 262 (1993) 1422-1425.
10. S.W. Hell, Toward fluorescence nanoscopy, Nat Biotechnol, 21 (2003) 1347-1355.
11. E.C. Jensen, Use of fluorescent probes: their effect on cell biology and limitations, Anat Rec (Hoboken), 295 (2012) 2031-2036.
12. X. Tian, L.C. Murfin, L. Wu, S.E. Lewis, T.D. James, Fluorescent small organic probes for biosensing, Chem Sci, 12 (2021) 3406-3426.
13. L.D. Lavis, R.T. Raines, Bright ideas for chemical biology, ACS Chem Biol, 3 (2008) 142-155.
14. G. Hong, A.L. Antaris, H.J.N.b.e. Dai, Near-infrared fluorophores for biomedical imaging, 1 (2017) 1-22.
15. C. Xu, F.W. Wise, Recent Advances in Fiber Lasers for Nonlinear Microscopy, Nat Photonics, 7 (2013).
16. J. Cao, B. Zhu, K. Zheng, S. He, L. Meng, J. Song, H. Yang, Recent Progress in NIR-II Contrast Agent for Biological Imaging, Front Bioeng Biotechnol, 7 (2019) 487.
17. S. Wang, B. Li, F. Zhang, Molecular Fluorophores for Deep-Tissue Bioimaging, ACS Cent Sci, 6 (2020) 1302-1316.
18. J.V. Jun, D.M. Chenoweth, E.J. Petersson, Rational design of small molecule fluorescent probes for biological applications, Org Biomol Chem, 18 (2020) 5747-5763.
19. D. Lingwood, K. Simons, Lipid rafts as a membrane-organizing principle, Science, 327 (2010) 46-50.
20. J.W. Borst, N.V. Visser, O. Kouptsova, A.J. Visser, Oxidation of unsaturated phospholipids in membrane bilayer mixtures is accompanied by membrane fluidity changes, Biochim Biophys Acta, 1487 (2000) 61-73.
21. P. Ostasov, J. Sykora, J. Brejchova, A. Olzynska, M. Hof, P. Svoboda, FLIM studies of 22- and 25-NBD-cholesterol in living HEK293 cells: plasma membrane change induced by cholesterol depletion, Chem Phys Lipids, 167-168 (2013) 62-69.
22. C.A. Marquezin, A.S. Ito, E.S. de Souza, Organization and dynamics of NBD-labeled lipids in lipid bilayer analyzed by FRET using the small membrane fluorescent probe AHBA as donor, Biochim Biophys Acta Biomembr, 1861 (2019) 182995.
23. C. Almeida, A. De Wreede, A. Lamazière, J.J.P.o. Ayala-Sanmartin, Cholesterol-pyrene as a probe for cholesterol distribution on ordered and disordered membranes: Determination of spectral wavelengths, 13 (2018) e0201373.
24. T. Mukherjee, M. Aravintha Siva, K. Bajaj, V. Soppina, S. Kanvah, Imaging mitochondria and plasma membrane in live cells using solvatochromic styrylpyridines, J Photochem Photobiol B, 203 (2020) 111732.
25. J.H. Pincus, S.I. Chung, N.M. Chace, M. Gross, Dansyl cadaverine: a fluorescent probe and marker in cell membrane studies, Arch Biochem Biophys, 169 (1975) 724-730.
26. M. Collot, P. Ashokkumar, H. Anton, E. Boutant, O. Faklaris, T. Galli, Y. Mely, L. Danglot, A.S. Klymchenko, MemBright: A Family of Fluorescent Membrane Probes for Advanced Cellular Imaging and Neuroscience, Cell Chem Biol, 26 (2019) 600-614 e607.
27. C. Liu, X. Gao, J. Yuan, R.J.T.T.i.A.C. Zhang, Advances in the development of fluorescence probes for cell plasma membrane imaging, (2020) 116092.
28. S. Samanta, Y. He, A. Sharma, J. Kim, W. Pan, Z. Yang, J. Li, W. Yan, L. Liu, J. Qu, J.S. Kim, Fluorescent Probes for

Nanoscopic Imaging of Mitochondria, Chem, 5 (2019) 1697-1726.

29. M.R. Lewis, W.H. Lewis, Mitochondria (and other cytoplasmic structures) in tissue cultures, 17 (1915) 339-401.

30. L.F. Yousif, K.M. Stewart, S.O. Kelley, Targeting mitochondria with organelle-specific compounds: strategies and applications, Chembiochem, 10 (2009) 1939-1950.

31. A.C. Shaikh, M.E. Varma, R.D. Mule, S. Banerjee, P.P. Kulkarni, N.T.J.T.J.o.o.c. Patil, Ionic pyridinium–oxazole dyads: design, synthesis, and application in mitochondrial imaging, 84 (2019) 1766-1777.

32. P. Ning, W. Wang, M. Chen, Y. Feng, X.J.C.C.L. Meng, Recent advances in mitochondria-and lysosomes-targeted small-molecule two-photon fluorescent probes, 28 (2017) 1943-1951.

33. J. Zielonka, J. Joseph, A. Sikora, M. Hardy, O. Ouari, J. Vasquez-Vivar, G. Cheng, M. Lopez, B.J.C.r. Kalyanaraman, Mitochondria-targeted triphenylphosphonium-based compounds: syntheses, mechanisms of action, and therapeutic and diagnostic applications, 117 (2017) 10043-10120.

34. W. Xu, Z. Zeng, J.-H. Jiang, Y.-T. Chang, L. Yuan, Discerning the Chemistry in Individual Organelles with Small-Molecule Fluorescent Probes, 55 (2016) 13658-13699.

35. S. Huang, R. Han, Q. Zhuang, L. Du, H. Jia, Y. Liu, Y. Liu, New photostable naphthalimide-based fluorescent probe for mitochondrial imaging and tracking, Biosens Bioelectron, 71 (2015) 313-321.

36. J. Zielonka, J. Joseph, A. Sikora, M. Hardy, O. Ouari, J. Vasquez-Vivar, G. Cheng, M. Lopez, B. Kalyanaraman, Mitochondria-Targeted Triphenylphosphonium-Based Compounds: Syntheses, Mechanisms of Action, and Therapeutic and Diagnostic Applications, Chem Rev, 117 (2017) 10043-10120.

37. L.F. Yousif, K.M. Stewart, S.O. Kelley, Targeting Mitochondria with Organelle-Specific Compounds: Strategies and Applications, 10 (2009) 1939-1950.

38. H. Zhu, J. Fan, J. Du, X. Peng, Fluorescent Probes for Sensing and Imaging within Specific Cellular Organelles, Acc Chem Res, 49 (2016) 2115-2126.

39. X. Zhong, Q. Yang, Y. Chen, Y. Jiang, B. Wang, J. Shen, A mitochondria-targeted fluorescent probe based on coumarin–pyridine derivatives for hypochlorite imaging in living cells and zebrafish, Journal of Materials Chemistry B, 7 (2019) 7332-7337.

40. Z. Wang, Y. Gu, J. Liu, X. Cheng, J.Z. Sun, A. Qin, B.Z. Tang, A novel pyridinium modified tetraphenylethene: AIE-activity, mechanochromism, DNA detection and mitochondrial imaging, Journal of Materials Chemistry B, 6 (2018) 1279-1285.

41. J.A. Mindell, Lysosomal acidification mechanisms, Annu Rev Physiol, 74 (2012) 69-86.

42. J.R. Casey, S. Grinstein, J. Orlowski, Sensors and regulators of intracellular pH, Nat Rev Mol Cell Biol, 11 (2010) 50-61.

43. N.E. Choi, J.Y. Lee, E.C. Park, J.H. Lee, J. Lee, Recent Advances in Organelle-Targeted Fluorescent Probes, Molecules, 26 (2021).

44. H. Zhu, J. Fan, S. Zhang, J. Cao, K. Song, D. Ge, H. Dong, J. Wang, X. Peng, Ratiometric fluorescence imaging of lysosomal Zn(2+) release under oxidative stress in neural stem cells, Biomater Sci, 2 (2014) 89-97.

45. J. Fan, Z. Han, Y. Kang, X. Peng, A Two-Photon Fluorescent Probe for Lysosomal Thiols in Live Cells and Tissues, Sci Rep, 6 (2016) 19562.

46. S.I. Reja, M. Gupta, N. Gupta, V. Bhalla, P. Ohri, G. Kaur, M. Kumar, A lysosome targetable fluorescent probe for endogenous imaging of hydrogen peroxide in living cells, Chem Commun (Camb), 53 (2017) 3701-3704.

47. M.C. Lee, S. Hamamoto, R. Schekman, Ceramide biosynthesis is required for the formation of the oligomeric H+-ATPase Pma1p in the yeast endoplasmic reticulum, J Biol Chem, 277 (2002) 22395-22401.

48. E.M. Nolan, J.W. Ryu, J. Jaworski, R.P. Feazell, M. Sheng, S.J. Lippard, Zinspy sensors with enhanced dynamic range for imaging neuronal cell zinc uptake and mobilization, J Am Chem Soc, 128 (2006) 15517-15528.

49. D.I. Danylchuk, P.H. Jouard, A.S. Klymchenko, Targeted Solvatochromic Fluorescent Probes for Imaging Lipid Order in Organelles under Oxidative and Mechanical Stress, J Am Chem Soc, 143 (2021) 912-924.

50. H. Zhang, J. Fan, H. Dong, S. Zhang, W. Xu, J. Wang, P. Gao, X. Peng, Fluorene-derived two-photon fluorescent probes for specific and simultaneous bioimaging of endoplasmic reticulum and lysosomes: group-effect and localization, J Mater Chem B, 1 (2013) 5450-5455.

51. B. Chazotte, Labeling nuclear DNA using DAPI, Cold Spring Harb Protoc, 2011 (2011) pdb prot5556.

52. B. Chazotte, Labeling nuclear DNA with hoechst 33342, Cold Spring Harb Protoc, 2011 (2011) pdb prot5557.

53. B. Zhou, W. Liu, H. Zhang, J. Wu, S. Liu, H. Xu, P. Wang, Imaging of nucleolar RNA in living cells using a highly photostable deep-red fluorescent probe, Biosens Bioelectron, 68 (2015) 189-196.

54. T. Mukherjee, M.A. Siva, K. Bajaj, V. Soppina, S. Kanvah, Imaging mitochondria and plasma membrane in live cells using solvatochromic styrylpyridines, Journal of Photochemistry and Photobiology B: Biology, 203 (2020) 111732.

55. T. Mukherjee, V. Soppina, R. Ludovic, Y. Mély, A.S. Klymchenko, M. Collot, S. Kanvah, Live-cell imaging of the nucleolus and mapping mitochondrial viscosity with a dual function fluorescent probe, Organic & Biomolecular Chemistry, 19 (2021) 3389-3395.

56. T. Mukherjee, R. Regar, V. Soppina, S. Kanvah, Stress-responsive rhodamine bioconjugates for membrane-potential-independent mitochondrial live-cell imaging and tracking, Organic & Biomolecular Chemistry, (2021).

	Sriram Kanvah *obtained his PhD in Chemistry from Indian Institute of Technology Bombay, Mumbai. He was a post-doctoral fellow at Georgia Institute of Technology Atlanta and worked as research-intellectual property analyst at General Electric Company Bangalore. Thereafter he joined IIT-Gandhinagar, Discipline of Chemistry in Dec 2009. His research interests lay in the synthesis and development of photoresponsive systems from organic electronic and biological imaging and chemosensing applications. Apart from research, Sriram shows keen interest in science promotion activities in schools and undergraduate colleges*
	Tarushyam Mukherjee *obtained his PhD from Indian Institute of Technology in the Chemical Biology research domain involving fluorescent organic molecules and their cellular imaging investigations. His research interest circles around the investigation of biological systems and unfolding the mysteries of the tiny cellular world using various physical and chemical tools.*

An Insight into Tailoring Sensors and Catalytic Systems Through Radiation Processing Methodologies

Nilanjal Misra[a], Swarnima Rawat[a,b], Narender K. Goel[a], Shubhangi A. Shelkar[a] and *Virendra Kumar[a,b]

[a]*Radiation Technology Development Division, Bhabha Atomic Research Centre, Mumbai-400085*
[b]*Homi Bhabha National Institute, Anushaktinagar, Mumbai-400094*
E-mail: vkumar@barc.gov.in

Abstract

Nanomaterials and enzyme based catalytic systems which offer superior performance, robustness, reusability and extended shelf lives are of vital importance for a range of environmental, industrial and healthcare applications. Radiation technology comes in handy as a versatile and low carbon footprint tool for designing such catalytic systems. Herein, we discuss the role of high energy ionizing radiation (gamma rays, electron beams, plasma) in synthesizing noble metal nanoparticles (Au, Ag, Pd) based catalytic systems and surface functionalized polymeric templates for immobilizing biologically and commercially relevant enzymes such as Uricase, Horseradish Peroxidase, Laccase, etc. The article compiles some of our recent work in designing multiple nanomaterials and immobilized enzyme based catalytic systems and their demonstrated efficiency in initiating crucial reactions involved in pollutant degradation, organic precursor production, reduction of toxic metal ion, etc., with a special emphasis on environmental remediation and societal applications

Keywords: Nanoparticles, Immobilized enzymes, Catalysts, Radiation grafting, environmental application

1. Introduction

Radiation technologies based on ionizing radiation (gamma rays, electron beams, plasma) offer a versatile tool for applications such as nanomaterials synthesis, polymer modification and materials processing. Applications of these materials are manifold and cover a wide range of fields, in industry, healthcare, environment, catalysis, sensors, agriculture etc. The added advantage of employing radiation technology over conventional material processing methods is that it is a low carbon footprint, environment friendly, high throughput and most often than not, a solvent free process that does not necessitate the use of harsh reaction conditions [1,2].
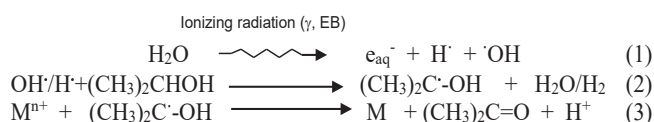
Metal nanoparticles, such as those of Au, Ag, Pd, Cu, etc., are well known for their catalytic prowess and are capable of initiating a gamut of important reactions [3]. However, their efficacy depends on different parameters such as the extent of purity, stability in solution phase, surface morphology, shape, size, etc.; all of which can be easily taken care of by adopting a bottom-up radiolytic synthesis approach. Additionally, radiation functionalized polymeric surfaces can also be used as templates to immobilize these nanoparticles and develop robust, reusable catalytic systems with longer shelf-life that can be easily separated from the final product post completion of the reactions. Similarly, the surface functionalized polymeric templates have been employed to immobilize enzymes, another class of highly efficient, but expensive biocatalysts. Immobilization of enzymes to these polymeric templates ensures reusability, improved temperature stability, broader pH operability and extended shelf life [4]. This article strives to recapitulate some of our recent advances made in the design and fabrication of radiation facilitated multiple nanomaterials and immobilized enzyme based catalytic systems for environmental and healthcare applications.

2. Radiation processing of materials

2.1. Radiolytic synthesis of metal nanoparticles

Radiolytic synthesis of metal nanoparticles is one of the important applications of ionizing radiation (Gamma, EB), which does not require any external chemical reducing agents. When an aqueous precursor noble metal ion solution, such as those of Au(III), Ag(I), Pd(II), etc., is irradiated under N_2 atmosphere in presence of a suitable stabilizing/capping agent (e.g., Polyvinyl pyrollidone, polyvinylalcohol, etc.) and Isopropyl alcohol, radiolysis of water takes place. Consequently, reactive radiolytic species, viz. e_{aq}^-, $H^.$, $^.OH$ are generated (Eq.1). $H^.$ and $OH^.$ react with Isopropyl alcohol present in the reaction medium to produce Isopropyl radical $((CH_3)_2C^.\text{-}OH)$ (Eq. 2), which is reducing in nature. These reducing species (e_{aq}^- and $(CH_3)_2C^.\text{-}OH$) are responsible for reduction of the metal ion to metal in zero valent state (Eq. 3).

$$H_2O \xrightarrow{\text{Ionizing radiation } (\gamma,\ EB)} e_{aq}^- + H^. + {}^.OH \qquad (1)$$
$$OH^./H^. + (CH_3)_2CHOH \longrightarrow (CH_3)_2C^.\text{-}OH + H_2O/H_2 \qquad (2)$$
$$M^{n+} + (CH_3)_2C^.\text{-}OH \longrightarrow M + (CH_3)_2C{=}O + H^+ \qquad (3)$$

The metal atoms (M) formed undergo further coalescence leading to formation of metal nanoparticles in presence of a capping/stabilizing agent. Polymers such as Poly(n-vinyl-2-pyrrolidone) (PVP) containing functional groups like >C=O and >N-, help in anchoring metal nanoparticles on their surface as well as stabilize the nanoparticles [5]. Figure 1 illustrates the overall process of formation of stable nanoclusters.

2.2. Radiation processing of polymers

Depending on the applications, four different radiation processes are employed for processing of polymers: i) Radiation grafting ii) Radiation crosslinking, iii) Radiation curing and iv) Radiation degradation. Radiation crosslinking and radiation degradation lead to bulk modification of polymers, whereas radiation
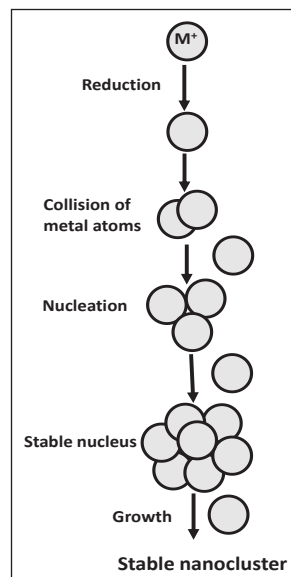

Figure 1: Schematic of overall process for formation of stable nanoclusters.

grafting and radiation curing processes are used for surface modification of polymers. These four processes have found widespread application in a range of fields, from industry, environment, healthcare to agriculture. In this review, we will restrict to some of the important applications of radiation grafting process in the field of catalyst design.

2.2.1. Radiation grafting process

Radiation grafting is a polymer modification process, wherein polymer chains of desired monomers are grown and covalently bonded onto an existing polymer backbone using ionizing radiation as a source of initiation. The advantages of this method over conventional surface functionalization techniques include room temperature processing conditions, better control over reaction parameters and free of toxic chemical initiators [6]. Figure 2 presents the schematic of a radiation grafting process. There are two different approaches generally adopted for radiation grafting

(i) **Simultaneous irradiation grafting:** In this method, the polymer substrate and monomer solution are simultaneously irradiated with ionizing radiation. The radicals generated

on the polymer backbone lead to graft copolymerization reaction, whereas, the radicals generated in the bulk monomer solution predominantly undergo homo-polymerization reaction.

(ii) **Post-irradiation grafting**: Here, the polymer backbone is first exposed to ionizing radiation to generate free radicals on it, and subsequently, brought in contact with the monomer solution to initiate the graft copolymerization reaction. The advantage of this method is the lower probability of homopolymer formation.

Radiation grafting is characterized by the extent of grafting, which is ascertained by grafting yield (G.Y.) measurement, determined gravimetrically using relation (1)

G.Y (%) = [(Weight after grafting - Initial weight)/Initial weight] x100 (1)

3. Radiation assisted synthesis of sensors and catalytic systems

With an aim to develop a range of sensors and catalytic systems, our group had initiated work on design, synthesis and development of metal nanoparticles and enzyme-based systems for environmental and healthcare applications.

3.1. Radiolytically synthesized metal nanoparticles: Sensor applications

3.1.1. Au based optical LSPR sensors

Radiolytically synthesized noble metal nanoparticles, such as those of Au and Ag, are unique in their ability to exhibit Localized Surface Plasmon Resonance (LSPR) bands. These bands are highly sensitive to the local environment and, therefore, serve as an ideal indicator for the presence of any external analytes in the vicinity [7-10]. Based on this concept, Poly(n-vinyl-2-pyrrolidone) stabilized Au nanoparticles (PVP-Au-NPs)-based sensors have been developed via gamma radiation assisted synthesis route for detection of Hg^{2+} ions and H_2O_2 in aqueous media.

The interaction of gamma radiolytically synthesized PVP-Au-NPs with Hg^{2+} ions have been observed to result in a decrease in intensity of Au LSPR band, with the relationship linear within a Hg^{2+} concentration range of 0-100nM [7]. TEM analysis also revealed that the interaction of PVP-Au-NPs with Hg^{2+} ions result in an overall increase in the average hydrodynamic size of the particles. For instance, 100nM Hg^{2+} induces a rapid change in the morphology of the PVP-Au-NPs from spherical to larger and irregular sized particles with broader size distribution compared to the control PVP-Au-NPs, which was also reflected as a change in its LSPR band characteristics (Figure 3). UV-Vis spectroscopy analysis revealed that in absence of Hg^{2+} ions, PVP-Au-NPs solution yielded a single, narrow peak at ~527nm, indicative of uniform sized spherical nanoparticles. On the other hand, addition of Hg^{2+} ions resulted in a decrease in the LSPR band intensity of the peak at 527nm. Moreover, for Hg^{2+} ion concentrations of 60nM and beyond, a prominent second broad peak appeared at ~740nm, suggesting agglomeration of Au-NPs, also validated by the appearance of larger particles in the TEM analysis (figure 3). This LSPR based PVP-Au-NPs optical sensor system was found to be selective for Hg^{2+} and independent of interference from other metal ions such as Ca^{2+}, Cu^{2+}, Cd^{2+} and Fe^{2+} up to a concentration of 500nM [7].
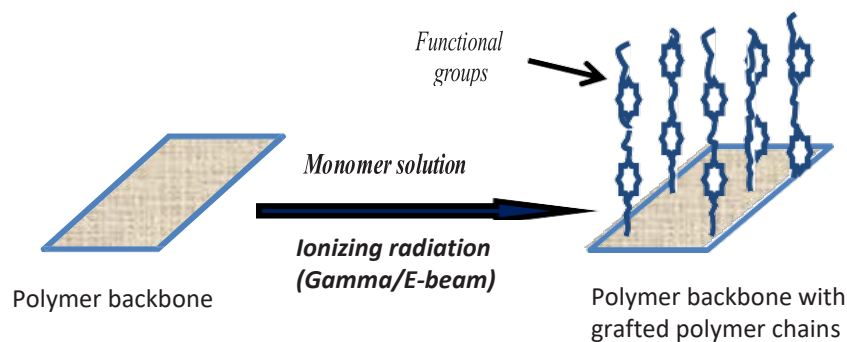

Figure 2: Schematic of radiation grafting process.

Functional groups

Monomer solution

Ionizing radiation (Gamma/E-beam)

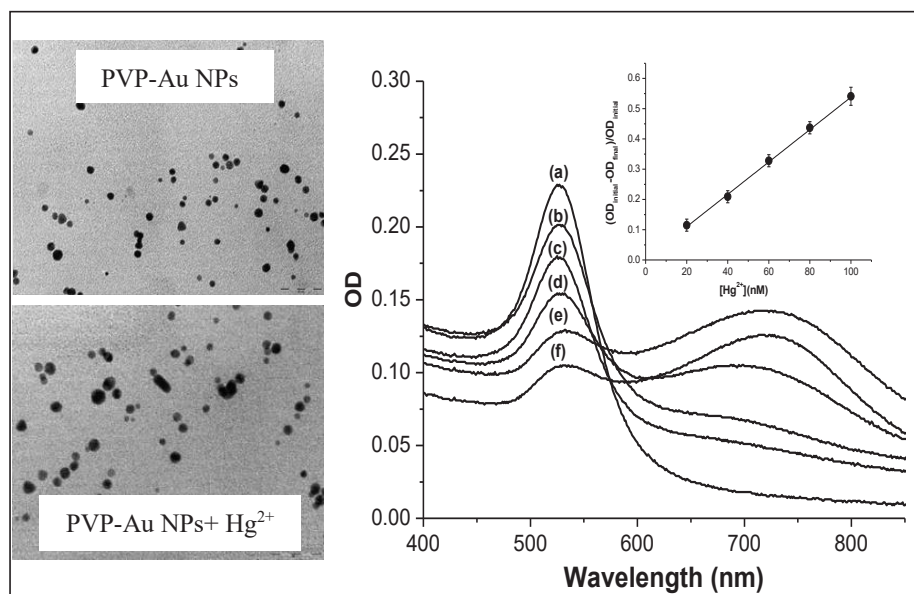Polymer backbone

Polymer backbone with grafted polymer chains

Figure 3: TEM images of PVP-Au NPs before and after interaction with Hg²⁺ ions, and the corresponding change in LSPR bands of PVP-Au NPs (Inset: Linear response in relative LSPR band intensity with Hg²⁺ ions concentration)

On the contrary, interaction of the product generated from H_2O_2 initiated oxidation of o-PDA results in an enhancement in the LSPR peak PVP-Au-NPs at 527 nm. The response was found to be linear in the H_2O_2 concentration range of 2.5×10^{-6} mol.dm⁻³ to 2.0×10^{-4} mol.dm⁻³ and 1.0×10^{-7} mol.dm⁻³ to 3.0×10^{-6} mol.dm⁻³ in two separate sets of experimental parameters, with a detection limit 1.0×10^{-7} mol.dm⁻³ [8].

3.1.2. Ag based LSPR sensors

On similar lines, we have exploited the LSPR properties of gamma radiolytically synthesized Ag nanoparticles. Poly(methacrylic acid) stabilized Ag nanoparticles (PMA-Ag-NPs) synthesized by gamma radiation were investigated for the spectrophotometric estimation of dopamine [9]. Dopamine belongs to a class of catecholamine neurotransmitters whose estimation is important owing to their involvement in diseases such as Parkinson's and schizophrenia. The PMA-Ag-NPs system showed the response of spectral change towards Dopamine concentration to be linear in the concentration range 5.0×10^{-7} mol.dm⁻³-1.6×10^{-5} mol.dm⁻³ in aqueous solution. Another point of note is that that ascorbic acid, which is present in millimolar concentration along with Dopamine (nanomolar to micromolar) in biological fluid, does not interfere in the estimation process even up to concentrations as high as 1.0×10^{-4} mol.dm⁻³, thereby highlighting the reasonable selectivity and robustness of the method [9].

Uric Acid estimation in blood is very important, as it is associated with diseases such as Hyperuricemia whose symptoms include gout, obesity, diabetes, high cholesterol, high blood pressure, leukemia, renal impairment and cardiovascular complications. Gamma radiolytically synthesized PVP stabilized Ag nanoparticles (PVP-Ag-NPs) have been employed for the detection of uric acid in biological samples [10]. The working principle is based on the oxidation of silver nanoparticles by hydrogen peroxide, which is generated in-situ during enzymatic degradation of uric acid in presence of enzyme uricase. This leads to the linear decrease in the LSPR band intensity of PVP-Ag-NPs at 410 nm with increase in the concentration of uric acid (figure 4). The linear range of detection of uric acid by this method was found to be 0 to 5.0×10^{-5} mol.dm⁻³ with minimum detection limit of 5.0×10^{-6} mol.dm⁻³. An interesting observation in the estimation process was that the sensing capability of the system was strongly dependent on the molecular weight of PVP being used as the capping agent. Low molecular weight PVP (40kDa) with shorter chains was found to render the Ag LSPR band more sensitive towards peroxide induced oxidation compared to higher molecular weight (160kDa and 360kDa) PVP capping agents. This is another example of how radiation mediated nano-synthesis processes allow us to finetune the stability and LSPR
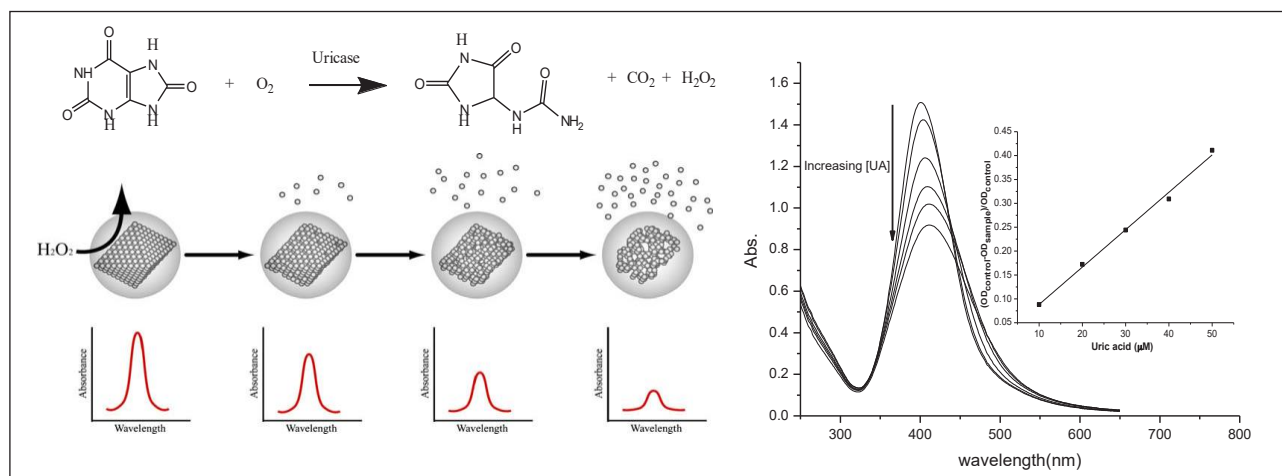
Figure 4: Working principle of PVP-Ag-NPs based Uric acid sensor, and LSPR band intensity as a function of Uric Acid concentration in presence of enzyme Uricase (Inset: Linear response in relative LSPR band intensity with Uric Acid concentration)

characteristics as per the target application.

3.2. Radiolytically synthesized metal nanoparticles: catalytic applications

3.2.1. Au nanoparticles (solution phase) based catalytic system

Au nanoparticles are also well known for their reducing properties. Chemically tailored Au nanoparticles had been previously tested for the catalytic reduction of *p*-nitrophenol to *p*-aminophenol (PAP). This reaction has high industrial relevance since PAP is a building block compound and is an important intermediate, produced in the syntheses of various chemicals, including dyes, pharmaceuticals (e.g., paracetamol), and anticorrosive lubricants. Working on this principle, we have radiolytically synthesized a poly (2,3-Epoxypropylmethacrylate) stabilize Au nanoparticles (PEPMA-Au-NPs) system and demonstrated its catalytic efficiency towards reduction of *p*-nitrophenol (PNP) to *p*-aminophenol (PAP) in presence of $NaBH_4$ [11]. The Turnover Frequency (TOF) for 10 μM catalyst concentration was determined to be 10.8 h^{-1}, which is comparable to the catalytic efficiency, reported earlier in the literature, for similar Au based catalytic systems. Moreover, the developed system was observed to be stable even after six months when stored at 4^0C, which

further enhances its practical utility.

3.2.2. Pd nanoparticles immobilized catalytic reactor (Pd-NICaR) system

The primary drawbacks of using nanoparticles-based catalysts in the solution phase are, reusability, shelf life and the issue of separation from the final product. To mitigate this problem, immobilization of nanoparticles onto a suitable substrate has been adopted as a viable solution, where surface functionalized polymeric matrices, containing anchoring groups such as epoxy, carboxylate, etc., are specifically tailored via radiation grafting/plasma-based processes to anchor radiolytically generated metal nanoparticles. Using this approach, we have developed a facile, reusable and robust Pd nanoparticles immobilized catalytic reactor (Pd-NICaR) system to initiate the catalytic reduction of Cr(VI), a highly toxic and widely prevalent water pollutant, to its less toxic Cr(III) form [2]. A room temperature, RF powered plasma grafting process was employed to functionalize a Polyethylene-Polypropylene (PE-PP) non-woven matrix with epoxy group containing monomer EPMA. The EPMA functionalized PE-PP (EPMA-*f*-PE-PP) substrate was subsequently used as a support matrix for in situ generation and immobilization of Pd NPs via gamma radiolytic route. The fabrication of Pd-NICaR system and
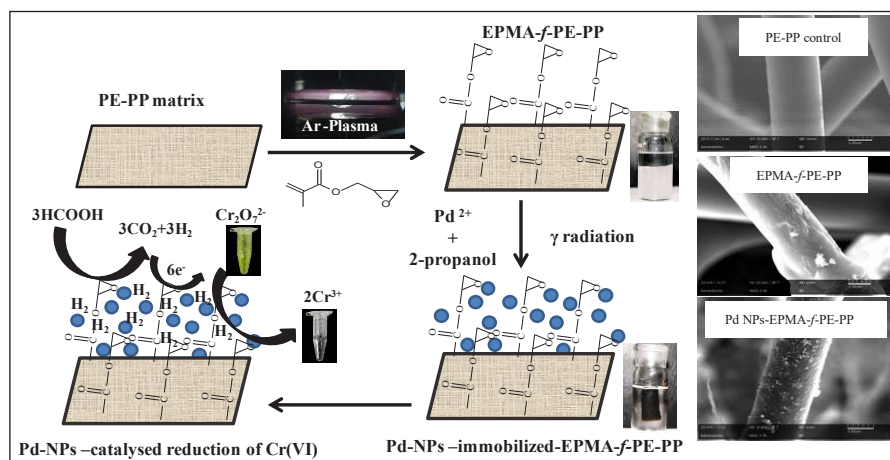
Figure 5: Schematic of fabrication of Pd-NICaR system and catalytic reduction of Cr(VI). SEM micrographs of control polymer PE-PP, EPMA-f-PE-PP and Pd NPs immobilized EPMA-f-PE-PP

catalytic reduction of Cr(VI) is presented in figure 5. Changes were also evident in the surface morphology of the sample at various stages of the functionalization process. Untreated non-woven PE-PP sample exhibited a highly porous and net like fibrous morphology. Transition in the surface morphology of the untreated PE-PP fibers from a smooth to increasingly rough form, with distinctly visible conformal layers of poly(EPMA) on the PE-PP fibers, was observed subsequent to functionalization. The width of the fiber also increased marginally post functionalization. Immobilization of Pd NPs led to further increase in surface roughness of the EPMA-f-PE-PP fibers (figure 5).
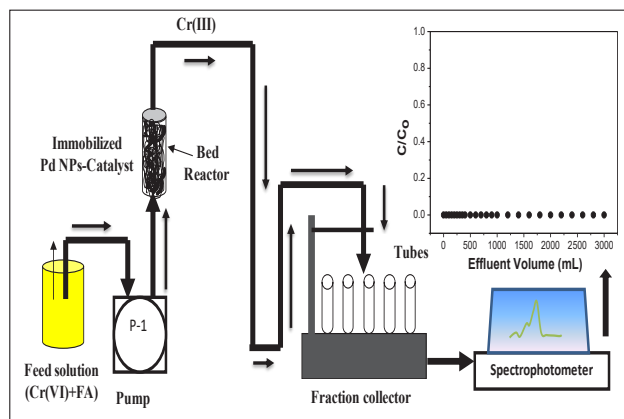

Figure 6: Schematic of remediation of Cr(VI) using Pd-NICaR packed fixed bed column reactor in continuous flow mode.

The catalytic efficacy of Pd-NICaR towards Cr(VI) reduction, in presence of formic acid (FA) as a reductant was demonstrated with the system showing excellent reusability (~20 cycles) and storage stability (>30 days) without substantial loss of catalytic activity. Practical applicability of the robust catalytic system towards Cr(VI) toxicity mitigation was established in continuous flow mode using a fixed-bed column reactor (figure 6).

3.2.3. Cu nanoparticles immobilized catalytic reactor (Cu-NICaR) system

Similarly, Copper Nanoparticles immobilized Catalytic Reactor (Cu-NICaR) system has been fabricated by immobilizing Copper Nanoparticles (Cu NPs) onto a radiation grafted EPMA-g-PE-PP non-woven matrix. The system was observed to exhibit excellent catalytic activity towards reduction of *p*-nitrophenol (PNP) to *p*-aminophenol (PAP) in presence of $NaBH_4$. Compared to solution phase catalytic systems used for PNP reduction, Cu-NICaR system afforded reusability, easy product separation and good shelf life owing to the catalyst being immobilized to a polymer matrix. The catalytic activity was demonstrated in batch process (12 cycles over 30 days) as well as in fixed bed column reactor modes, wherein a 1g packed bed reactor operated at 800 ml.h^{-1} could completely reduce more than 5000 ml of 1.0 mM PNP without appearance of any breakthrough point [12].

3.3. Radiation grafted polymer templates for enzyme immobilization: reusable bio-catalysts

Enzymes are bio-catalysts bearing some remarkable properties (high activity, selectivity and specificity) that facilitate their performing the most complex chemical processes under the

most benign experimental and environmental conditions. The use of soluble free enzymes is however limited due to issues pertaining to their cost, reusability, stability, sensitivity to various denaturants and applications in continuous reactors. To overcome these limitations, the use of immobilized enzymes has now taken precedence over free enzymes. Immobilization not only affords enhanced stability, activity, specificity, selectivity, reduced inhibition, but also enhances the thermal stability of the enzyme, broadens the pH range of enzyme activity and enables recovery of product with greater purity. At the same time, separation and reusability of the enzyme becomes feasible, which is extremely essential when using expensive or scarcely produced enzymes. In a nutshell, immobilization generates continuous economic operations, automation and high investment/capacity ratio [13]. Recently, we have developed a number of radiation functionalized polymer based immobilized enzyme systems and investigated their utility in facilitating environmentally and industrially relevant reactions.

3.3.1. Uricase immobilization: Uric acid biosensor

We have designed a functional polymer support for covalent immobilization of enzyme uricase, which was further utilized in a single enzyme-silver nanoparticle based optical biosensor system for estimation of uric acid [1]. A carboxylic acid functionalized polymer support was fabricated via gamma radiation grafting of polyacrylic acid (PAA) on to non-woven polypropylene (PP) matrix. Uricase was immobilized on to the PAA-g-PP support via covalent amide linkage using coupling agents, namely N-hydroxysuccinimide (NHS) and 1-ethyl-3-(3-(dimethylamino)propyl)carbodiimide (EDC) (figure 7). The catalytic activity of uricase was investigated spectrophotometrically using uric acid as a substrate. The uricase-immobilized-PAA-g-PP samples could be repeatedly used for ~20 cycles over a period of 30 days. The uricase immobilized samples were successfully used in conjunction with the radiolytically synthesized Ag-NPs as a LSPR-optical biosensor for estimation of uric acid [1,10].

3.3.2. Horseradish peroxidase (HRP) immobilization: Dye degradation

Peroxidase is a class of enzyme widely distributed in microbes, plants and animals. It is an oxidoreductase enzyme, which, in the presence of hydrogen peroxide, oxidizes a wide range of phenolic compounds, such as guaiacol, catechol, pyrogallol, etc. This class
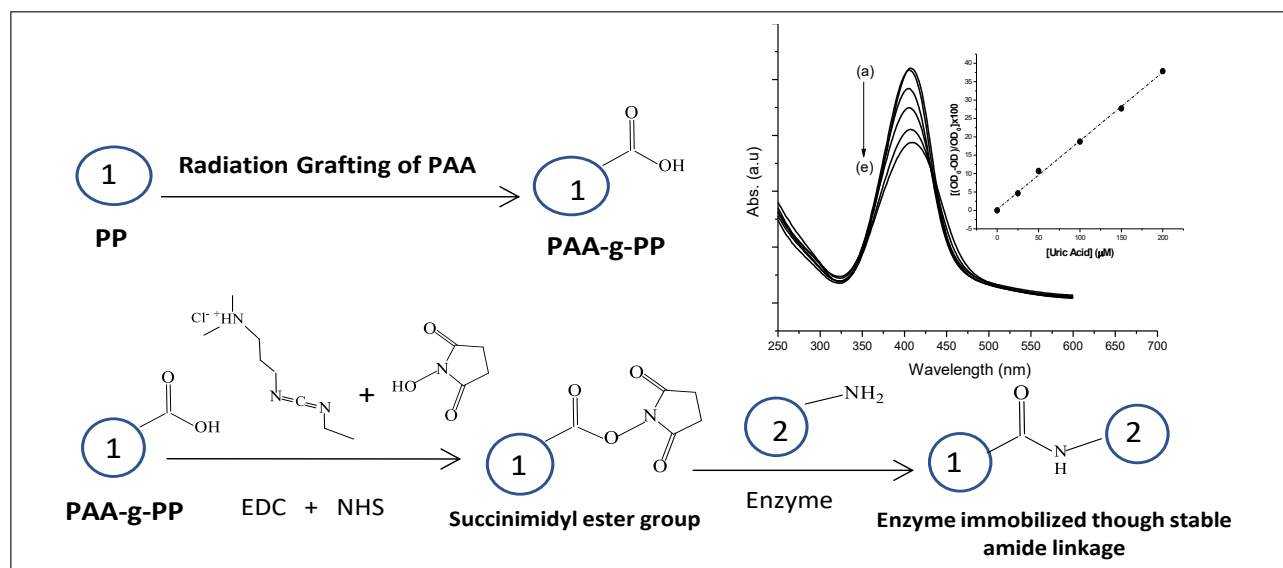

Figure 7: PAA grafting and immobilization of uricase (enzyme) on to PAA-g-PP using EDC and NHS coupling agents. (Inset: Uric acid estimation by Ag-NP based optical sensor using immobilized uricase enzyme)

of enzymes, therefore, has potential industrial and environmental relevance, particularly in fields such as dye decolorization, wastewater treatment, removal of peroxides from foodstuff, etc. With a view to design an immobilized HRP based dye decolorization catalytic system, epoxy functionalized Polypropylene (PP) films were fabricated via mutual irradiation grafting of EPMA using ⁶⁰Co-gamma radiation source [6]. Enzyme HRP was covalently immobilized using a single step-room temperature coupling reaction of amine group of enzyme with the epoxy group of grafted poly(EPMA) chains (figure 8). The activity of the immobilized enzyme was assayed using a substrate 2,2'-azino-bis(3-ethylthiazoline-6-sulfonate) (ABTS). The practical applicability of immobilized HRP in the catalytic degradation of textile dyes was investigated using Basic Red 29 (BR29) as a model dye. The immobilized enzyme system was found to cause ~90% degradation of BR29 over a period of 20 days and was reusable for five cycles without substantial loss in activity.

3.3.3. Laccase immobilization

Laccases are another class of interesting enzymes which, owing to their very broad substrate specificity with respect to the electron donor, can be used for treatment of effluents from pulp mills or from other industries containing chlorolignins or phenolic compounds. The enzymes render phenolic compounds less toxic
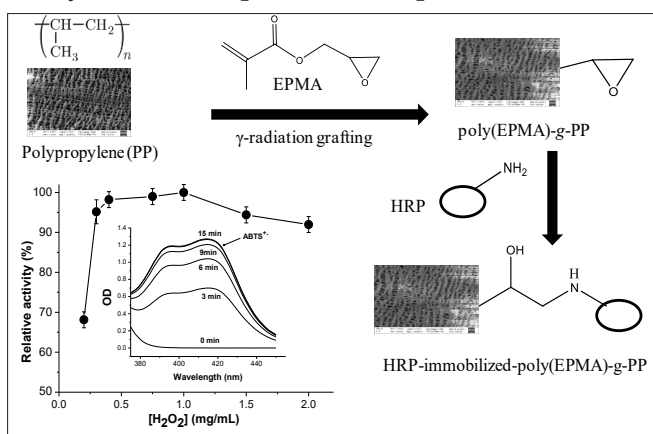

Figure 8. EPMA grafting and immobilization of HRP on to PEPMA-g-PP film. Inset: Enzymatic activity estimation and effect of [H₂O₂].

via degradation or polymerization reactions and/or cross-coupling of pollutant phenols with naturally occurring phenols. To support Laccase, we synthesized epoxy functionalized polyethersulfone (PES) beads via interpenetrating polymer network formation with poly(EPMA) using ⁶⁰Co-gamma radiation source [14]. The Poly(EPMA)-functionalized-PES [poly(EPMA)-*f*-PES] beads were fabricated using phase inversion route, followed by a single, amine group facilitated laccase immobilization step. The immobilized laccase was successfully employed to degrade a widely used textile dye Acid Red 1 (AR1) in aqueous solution. Room temperature incubation of the laccase immobilized poly(EPMA)-*f*-PES beads with AR1 dye (~10ppm) resulted in ~88% degradation of the dye over a period of 15 days and could be repeated for three cycles (figure 9).

3.3.4. Catalase immobilization

Radiation technology can also be effectively used for Cellulose valorization by converting cellulose waste into useful, surface tailored functional templates for enzyme immobilization. This was achieved through gamma radiation induced mutual irradiation grafting of monomer Glycidyl methacrylate (GMA) onto Cotton cellulose matrix [15]. These epoxy functionalized poly(GMA)-g-Cellulose substrates were subsequently tested for immobilization of an industrially relevant enzyme Catalase, which is responsible for catalyzing the oxidation degradation of H_2O_2 and is thus an useful reagent in the detection of trace levels of peroxide impurities. This immobilized system was observed to be reusable for over five cycles with activity comparable to that of free catalase under identical reaction conditions.

4. Conclusions

Radiation technology has proved its worth as an excellent tool for materials processing and has helped design new and advanced nano-catalytic systems and functional polymeric supports for fabrication of NPs and enzyme immobilized robust catalytic systems for a broad spectrum
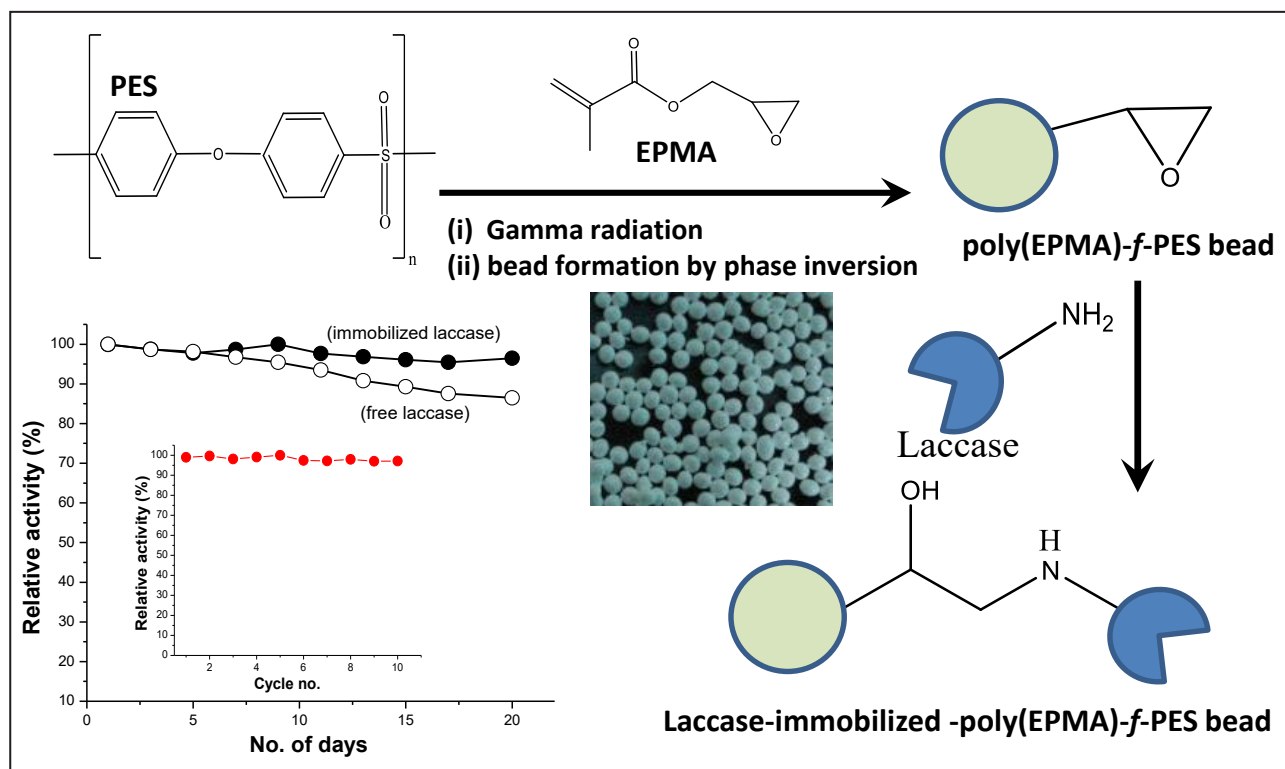
Figure 9: Schematic of fabrication of poly(EPMA)-f-PES beads and immobilization of laccase on to poly(EPMA)-f-PES beads. Inset: Storage stability and recyclability of laccase immobilized poly(EPMA)-f-PES.

of environmental and healthcare applications. Improved operational, storage and thermal stabilities along with reusability of immobilized catalytic systems makes them efficient catalysts for economic viability and potential large-scale applications. The future of radiation technology, therefore, lies in its continued application for designing attractive new materials that help solve some of our most pertinent environmental and societal problems.

Acknowledgements

References

1. Kumar V., Misra N., Paul J., Dhanawade B. R., Varshney L., Uricase-immobilization on radiation grafted polymer support for detection of uric acid using Ag-nanoparticle based optical biosensor, Polymer, 2014, 55, 2652-60.

2. Misra N., Kumar V., Rawat S., Goel N. K., Shelkar S. A., Jagannath, Singhal R. K., Varshney L., Mitigation of Cr(VI) toxicity using Pd-nanoparticles immobilized catalytic reactor (Pd-NICaR) fabricated via plasma and gamma radiation, Env. Sci. Pol. Res., 2018, 25(16), 16101-10.

3. Crooks R. M., Zhao M., Sun L., Chechik V., Yeung L. K., Dendrimer-Encapsulated Metal Nanoparticles: Synthesis, Characterization, and Applications to Catalysis, Acc. Chem. Res., 2001, 34, 181–190.

4. Datta S., Christena L. R., Rajaram Y. R. S., Enzyme immobilization: an overview on techniques and support materials, Biotechnology, 2013, 3, 1–9.

5. Oster G., Immergut E. H., Ultraviolet and Infrared Spectral Studies of Polyvinylpyrrolidone. J. Am. Chem. Soc., 1954, 76(5), 1393-96.

6. Kumar V., Misra N., Goel N. K., Thakar R., Gupta J., Varshney L., A horseradish peroxidase immobilized radiation grafted polymer matrix: a biocatalytic system for dye waste water treatment, RSC Adv., 2016, 6, 2974-2981.

7. Misra N., Kumar V., Goel N. K., Varshney L., Radiation synthesized Poly(n-vinyl-2-pyrrolidone)-stabilized-Gold nanoparticles as LSPR based optical sensor for Mercury ions estimation, J. Nanopar. Res., 2015, 17, 1-9.

8. Misra N., Biswal J., Gupta A., Sainis J. K., Sabharwal S., Gamma radiation induced synthesis of gold nanoparticles in aqueous polyvinyl pyrrolidone solution and its

application for hydrogen peroxide estimation, Rad. Phys. Chem., 2012, 81, 195-200.

9. Biswal J., Misra N., Borde L., Sabharwal S., Synthesis of silver nanoparticles in methacrylic acid solution by gamma radiolysis and their applications for estimation of Dopamine in low concentration, Radiat. Phys. Chem., 2013, 83, 67–73.

10. Misra N., Kumar V., Borde L., Varshney L., Localized surface plasmon resonance-optical sensors based on radiolytically synthesized silver nanoparticles for estimation of uric acid, Sensor. Actuat. B-Chem., 2013, 178, 371-78.

11. Misra N., Goel N. K., Varshney L., Kumar V., Gamma radiolytic synthesis of poly(2, 3-Epoxypropylmethacrylate)-stabilized-gold nanoparticles: an efficient catalyst for p-nitrophenol reduction, Adv. Mater. Proc., 2018, 3, 199-205.

12. Rawat S., Misra N., Kumar V., Shelkar S.A., Goel N.K., Singhal R.K., Varshney L., Radiation engineered copper nanoparticles immobilised catalytic reactor (Cu-NICaR) system, Adv. Mater. Lett., 2018, 9, 684-691.

13. Khan A. A., Alzohairy M. A., Recent Advances and Applications of Immobilized Enzyme Technologies: A Review, Res. J. Biol. Sci., 2010, 5, 565-75.

14. Misra N., Kumar V., Goel N. K., Varshney L., Laccase immobilization on epoxy functionalized Polyethersulfone beads and their application for degradation of acid dye, Polymer, 2014, 55, 6017–6024.

15. Misra N., Goel N. K., Shelkar S. A., Varshney L., Kumar V., Catalase immobilized-radiation grafted functional cellulose matrix: A novel biocatalytic system, J. Mol. Catal. B Enzym., 2016, 133, 172-178.

Dr. Nilanjal Misra is a Scientific Officer in the Radiation Technology Development Division, Bhabha Atomic Research Centre. After completing his M.Sc. in Chemistry from IIT Delhi, he joined the 53rd Batch of BARC Training School in 2009. He received his PhD from Homi Bhabha National Institute, Mumbai in 2015 and was a recipient of the prestigious Rutherford-Marie Curie Postdoctoral Fellowship at Daresbury Laboratory, ASTEC, United Kingdom (2018-2020). His research interests are focused on plasma/ radiation processing of polymeric materials and thin films deposition using PECVD and HPCVD techniques.

Ms. Swarnima Rawat is working as a Scientific Officer in the Advanced Material Section, Radiation Technology Development Division, Bhabha Atomic Research Centre. She completed her graduation and post-graduation in Chemistry from Hindu college, University of Delhi. She did her training with the 10th batch of IGCAR training school (2015-2016) and is the Homi Bhabha Awardee for her batch. Her research field involves radiation and plasma processing of materials to fabricate adsorbents, catalytic systems, sensors, indicators etc. for various environmental applications.

Dr. N. K. Goel, Scientific officer, obtained his M.Sc. in Organic Chemistry from M. D. U University, Rohtak, Haryana, India. He joined the Radiation Technology Development Division of Bhabha Atomic Research Centre, Mumbai after successful completion of one-year Orientation Course for Engineering Graduates and Science (OCES) and obtained his Ph.D. Degree from Homi Bhabha National Institute, Mumbai in 2014. His area of specialization is surface modification of polymers using high energy radiation (Gamma and EB) for Environmental, Industrial and Healthcare applications. He has number of National and International publications, book chapters, invited talk to his credit.

Ms. Shubhangi A. Shelkar, scientific Assistant-D, obtained her B.Sc. in Chemistry from North Maharashtra University, Jalgaon, Maharashtra. She joined RTDD, BARC in 2016 after successful completion of CAT-I trainee 2014-2016 batch. She has been working in the field of radiation processing of materials including nanomaterials and polymers for different societal applications.

Dr. Virendra Kumar, Head, Advanced Material Section, Radiation Technology Development Division, BARC & Assoc. Prof. HBNI, Mumbai, joined BARC after completion of one-year Orientation Course for Engineering Graduates and Science (OCES) of 42nd batch. He obtained his Master's degree from IIT Roorkee and PhD degrees from Mumbai University, respectively. He completed his Post-doctoral research (2007-2009) from ENSCP, Université Pierre et Marie Curie, Paris, France. He is the recipient of several awards including DAE-S&TEA-2016, DAE-GAA-2016, IANCAS-Dr. T. Dutta Memorial Award-2016 and ISRAPS-Dr. P. K. Bhattacharyya MemorialAward-2006. His research activities include Radiation and plasma processed polymers and nanomaterials for wastewater remediation, sensors & catalytic systems, antifouling & super-hydrophobic surfaces, smart hydrogels, etc. He has over 200 publications, including international journal, book chapter, reviews, conferences, and technical reports in his credit.

Gas-phase Molecular Clusters: Unique Nano-Reactors for Condensed Phase Research

Pramod Sharma*, Soumitra Das

Chemistry Division, Bhabha Atomic Research Centre, Mumbai-400085, India
*E-mail: pramod@barc.gov.in

Abstract

Distinctive physical and chemical properties exhibited by molecular clusters have been exploited extensively for understanding several complex chemical, atmospheric and biological processes, at molecular level. Present article highlights some of these studies, which have been carried out under laboratory conditions, using molecular clusters as model nano-reactors.

1. Introduction

In a chemical reaction, interaction between atoms/molecules often involves creation and/or breaking of bonds resulting in formation of distinct molecules. On the contrary, under specific experimental conditions, these atoms and molecules may aggregate together under influence of weak Van der Waals interactions, resulting in formation of clusters. These clusters represent a unique class of material, which exhibit dual nature of bonding - comprising of strong intramolecular bonds as well as weak intermolecular interactions. Though the intermolecular interactions are much weaker than intramolecular bonds, they moderately perturb cluster properties, as compared to properties of isolated atoms and molecules of which they are composed. The extent of variation in properties of clusters is directly related to strength of intermolecular interactions. These weakly bound aggregates, range in size from dimer to congregate of thousands of atoms and molecules and exhibit unique properties quite different from their monomer constituent [1]. Some of the characteristic features exhibited by clusters, which make them an interesting system for scientific studies are listed below:

- Clusters exhibit size dependent variation in chemical, optical, catalytic, electrical and magnetic properties. Such cluster size dependent variation in properties has been ascribed to surface effect, which arises due presence of nearly all atoms/molecules on or near the surface of cluster (i.e. large surface to volume ratio). Thus, cluster properties can be significantly manipulated by slight variation in number of constituent atoms/molecules within the cluster.

- Intrinsic properties of cluster are different from their corresponding gaseous and bulk phase analogue. Also they exhibit distinct cluster specific chemical and physical properties, which depend on nature of cluster constituents and cluster size

- Clusters are considered ideal medium for understanding complex molecular processes ensuing in complex environment at molecular level, due to their inherent properties like finite size, bulk-like density and their secluded existence in gas-phase unperturbed by external factors.

- Also, clusters possess large number of internal degree of freedom and closely spaced energy levels, which make them an efficient heat bath, as they can dissipate energy and cool down in vacuum by evaporation of their constituents from the surface.

These characteristic features have promoted the topic of cluster science as a frontline area of research, spanning over a wide field ranging from physics, chemistry, materials science, biology and astronomy. In these studies,

clusters are often utilized as nano-laboratories for understanding various chemical, physical and biological phenomena at molecular level, where weak intermolecular interactions are considered to play decisive role [2]. For example, clusters have been utilized to obtain insight about influence of solvent at molecular level, which is of relevance in various chemical processes. Also, clusters are considered as ideal medium for basic understanding of different processes like energy dissipation, interaction between biomolecules, influence of intermolecular interactions on structure and stability of biomolecules, catalysis, photochemistry etc. Clusters have also been doped with different molecules for understanding mechanism of chemical reaction and for carrying out spectroscopic studies at a temperature of few kelvins to sub kelvin range. Generally large helium clusters offer super fluid environment for studying chemical reactions, determining structure and spectroscopic properties of chemical/biological species, embedded within the helium cluster [3]. In this article, we will highlight some of the studies where clusters have been used as model nanoreactors for understanding different processes, relevant to catalysis, atmospheric & interstellar chemistry, and biology, after briefly describing methods of cluster generation and characterization.

2.1 Generation and characterization of clusters

Gas-phase clusters of atoms and molecules are prepared by supersonic expansion of gases and liquids having high vapour pressure, through a narrow nozzle into vacuum. During the process, adiabatic cooling arising from transformation of thermal energy of gas into kinetic energy of supersonic jet, lowers the translational, rotational and vibrational temperature of the gaseous species to a few kelvins. Collisions within the expanding gaseous mixture transform the random motion of the gas into directed flow. Lower temperature coupled with unidirectional flow of gaseous molecules and frequent collisions during the expansion process leads to generation of clusters in the supersonic jet. In the initial phase

of cluster nucleation and growth, three body collisions play a vital role, as the process of cluster formation is exoergic in nature and the third body is required for removal of excess energy from the system in the form of kinetic energy. This method of cluster generation is generally employed for carrying out studies on pure molecular clusters or mixed clusters of molecular species having significant vapour pressure. While for generation of clusters of refractory materials i.e. metals and ceramics, laser vapourization method coupled with supersonic expansion source is employed. Using this method cluster of virtually any element and their compound can be generated. In this method, the refractory material in form of pellet or rod is ablated with a focused pulse of a laser beam, which results in generation of plasma at the target surface with temperature $\sim 10^4$ K. The laser generated plasma is supersonically cooled using monoatomic inert gases, resulting in formation of clusters of refractory materials (Fig. 1) using a Smalley type cluster source [4]. Size of cluster generated by supersonic expansion
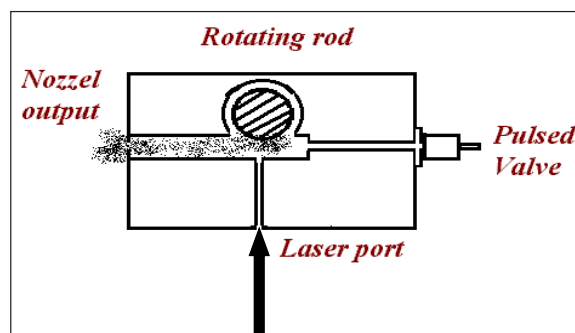

Figure 1: Smalley type source for generation of cluster of refractory materials by laser ablation

span over a broad range and exhibit log-normal distribution, and is usually characterized by average cluster size. The average cluster size depends on the inert gas pressure, temperature of the stagnation chamber, diameter of the nozzle and the bond constant of the clustering molecules. Generally, "Hagena parameter" is widely used to determine the average size of cluster under given set of experimental conditions [5].

For generation of embedded heterogeneous clusters, where an atom or molecule is externally

attached/ adsorbed on the host cluster surface, pick-up technique is generally used. In this method, the initial clusters (the host clusters) generated via supersonic expansion are interacted perpendicularly by a beam of foreign atom/molecule/cluster, at a certain distance downstream from the nozzle. Collision between the supersonically generated clusters and the externally directed atoms/molecules results in the formation of heterogeneous clusters. The extent of doping of the cluster surface or number of captured molecules on the cluster surface depends on the pressure of the pick-up source. By adjusting the pressure of the pick-up source, one can optimize the conditions, so that only few molecules are adsorbed on the surface of the clusters. This method is widely used for preparation of metal-doped molecular clusters. As reactions on clusters have analogies with reaction which transpire on bulk surfaces, such types of cluster are widely used for understanding processes occurring on bulk surfaces.

These gas-phase clusters are fundamental tools for understanding energy dynamics, effect of solvation, photochemistry of clusters, and for understanding intermolecular interactions and its influence on structure. Such studies are vital for understanding the weak attractive forces that bind different molecules within the cluster. Different techniques have been used to characterize various features of clusters ranging from understanding their shape and stability, size distribution, reactivity and other processes. Some of the techniques which are widely used are time-of-flight mass spectrometry, ion-mobility, laser based techniques - resonance enhanced multiphoton ionization, laser-induced fluorescence (LIF), fluorescence/resonant-ion depletion by infrared (FDIR/RIDIR) spectroscopy [6], zero kinetic energy (ZEKE) photo-electron spectroscopy, etc., to name a few. Utilization of these methods for understanding different processes, which are of relevance to catalysis, atmospheric and interstellar chemistry and biological studies are listed below.

2.2. Molecular clusters as model nanoreactors in heterogeneous catalytic chemistry

Over the last decade, single-atom catalysts (SAC's) have emerged as a new class of heterogeneous catalysts. These SAC's, have attracted considerable interest due to their higher efficiency, activity and selectivity as compared to traditionally utilized catalysts, besides aiding in effective utilization of precious metals. For these catalysts, conventional methods are of limited help in characterizing and understanding their catalytic mechanisms, which is essential for development of superior catalysts [7]. As the nature of active sites, coordination environment and electronic structure, are important factors which affect the overall properties of the catalysts. Here, clusters have emerged as an effective medium for fundamental understanding of catalytic activity at molecular level. Besides, clusters have also been employed for screening catalytic activity of different homogeneous and heterogeneous catalyst. A typical example is oxidation of CO into CO_2, which is an important prototypical reaction in heterogeneous catalysis and has been extensively investigated in the gas phase for understanding the underlying catalytic mechanism. For example, isolated single Pt atom on iron oxide support (Pt_1/FeO_x), exhibits excellent catalytic activity for CO oxidation [8]. Consequently, for molecular-level understanding of SAC process, studies have been carried in gas-phase on metal doped heteronuclear metal oxide clusters (HMCOS). In these studies, the metal ions or metal incorporated HMCOS were generated by laser ablation of the mixed-metal disks compressed with different metal powders, in the presence of O_2 seeded in the He carrier gas. The molar ratios of different metals and the percentages of O_2 used in the He carrier gas was varied, depending on the nature of the different HMOCs. Subsequently, the cluster ions of interest were mass-selected using a quadrupole mass filter and were transferred into a linear ion trap (LIT) reactor, where they were confined and thermalized by collisions

with a pulse of He gas [9]. Afterwards, these thermalized clusters are interacted with a pulse of CO, O_2, or a mixture of CO and O_2 under thermal collision conditions. The cluster ions ejected from the LIT are later characterized by a reflectron time-of-flight mass spectrometer (RTOF-MS). Structure of these cluster ions generated has also been characterized by collision induced dissociation and photoelectron spectroscopy. Using above method, studies have been carried out on single Au/Pt atom doped heteronuclear metal oxide clusters. In these studies, only few Au_1 or Pt_1 doped gas-phase systems were found to be catalytically active for CO oxidation (Au/Al_3O_{3-5}, Pt/Al_3O_{5-7}), while some systems were found to exclusively adsorb CO. A concept of electronegativity-ladder effect was proposed to explain enhanced reactivity of these noble metal doped HMOCs. Further, these findings have been extended for designing of noble metal-free HMOCs for catalytic CO oxidation by O_2 [9].

Another important catalytic reaction which has been investigated is metal ion mediated cyclization of acetylene. In these studies, acetylene clusters containing transition metal atomic ions i.e. $M^+(C_2H_2)_n$, are employed as nano-reactors to assess catalytic activity of metal ions towards acetylene polymerization in the gas phase. This catalytic reaction is of relevance in industrial and interstellar chemistry, for understanding formation/origin of large polycyclic aromatic hydrocarbons [10]. In one such study the kinetics of successive reactions of acetylene (C_2H_2) initiated on vanadium and iron atomic cations have been investigated under thermal conditions using the variable-ion source and temperature-adjustable selected-ion flow tube apparatus [11]. Based on these studies it was proposed that cyclization of acetylene mediated via Fe^+ involves successive addition of three acetylene molecules, yielding $Fe^+(C_2H_2)_3$, followed by addition of a fourth acetylene molecule. Addition of fourth acetylene molecule initiates cyclotrimerization, yielding $Fe^+(C_2H_2) + C_6H_6$ (benzene) or $Fe^+(C_6H_6)$ + C_2H_2. In contrast, the reaction of V^+ with C_2H_2

yielded cluster fragment ions arising from successive associations i.e. $V^+(C_2H_2)_n$ (n=1-12) and from loss of H_2 ($V^+C_2(C_2H_2)_m$ (m=1-12)).

In another study, nitridation of tantalum has been investigated in gas-phase [12]. Tantalum nitride is an attractive material, having several applications in field of microelectronics, thin film resistors, as a vermilion pigment (free from toxic heavy metals) and as a photo-catalyst. Investigation involved reaction of ammonia with size-selected tantalum clusters. Based on these studies it was concluded that tantalum clusters (Ta_n^+) undergoes successive nitridation by ammonia molecules accompanied by dehydrogenation. The nitridation reaction continues until the tantalum atoms within the cluster attain +5 oxidation state, thus exclusively producing tantalum(v) nitride over a wide range of cluster size. On the contrary in bulk phase, tantalum forms nitrides in either +5 or +3 oxidation state.

Besides, clusters have also been utilized to screen catalytic activity of different metal ions towards various catalytic processes. Certain transition metal ions stimulate C−C, C−H, O-H and O−O bond activation in gas-phase reactions, leading to generation of higher hydrocarbons and value added products. For example, insertion reaction initiated by Ti^+ ions with methanol in gas-phase leads to generation of TiO^+, $TiOH^+$, $Ti(CH_2O)^+$, and $Ti(CH_3O)^+$ primary product ions. Based on laser ablation−molecular beam studies, elimination of hydrogen molecule has been suggested to be a dominant process for ion−molecule reactions of Ti^+ with methanol clusters, resulting in generation of fragment ions $Ti^+(CH_3OH)_{n-1}CH_2O$. Likewise, interaction of Ti^+ with methanol clusters has been reported to generate primary ions $TiO^+(CH_3OCH_3)(CH_3OH)_n$, suggesting catalytic conversion of methanol into dimethyl ether [13]. In one of our study, we have also investigated catalytic activity of laser ablated transition metals ions upon interaction with methanol clusters [14]. Figure 2 illustrates mass spectra obtained for gas-phase reaction
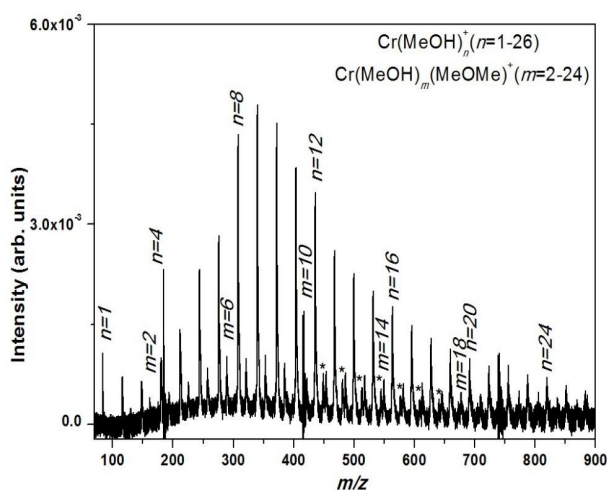
*Figure 2: Time-of-flight mass spectra obtained upon interaction of Cr^+ ions with methanol clusters. In addition to ion peaks corresponding to $Cr^+(MeOH)_n$ (n=1-26) and $Cr^+(MeOH)_m(MeOMe)$ (m=2-24) series, ion signal marked with * correspond to cluster fragment ions $Cr^+(MeOH)_q(H_2O)$ (q=12-20).*

of Cr^+ ions with methanol clusters. In the mass spectrum two series of cluster ion signals are observed corresponding to $Cr^+(MeOH)_n$ (n=1-26) and $Cr^+(MeOH)_m(MeOMe)$ (m=2-24). Based on the mass spectrum it can be concluded that Cr^+ ions facilitates catalytic conversion of methanol to dimethyl ether for $Cr^+(MeOH)_n$ clusters with n ≥ 4, via following reaction –

$$Cr^+(MeOH)_n \ (n \geq 4) \rightarrow Cr^+(MeOH)_m(MeOMe) \ (m \geq 2)$$
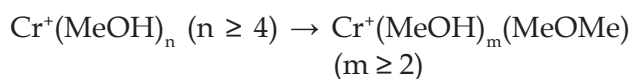
Similar studies involving interaction of metal ions with molecules and their clusters has led to extensive studies for understanding catalytic activity of metal ions, which are of significance in various chemical, biological and physical processes. Thus, gas-phase studies have significantly enriched our understanding about behaviour of transition metal ions in the bulk phase. Here, mass spectrometric studies of gas-phase ion−molecule reactions have significantly contributed in deriving qualitative and quantitative information about intrinsic physical and chemical properties of metal ions, while circumventing complexity of the bulk phase.

2.3. Molecular Cluster for mimicking atmospheric processes in laboratory

Role of clusters in influencing chemical processes in the atmosphere and interstellar space has been extensively investigated. In the rarefied environment, clusters offer suitable heterogeneous surface for adsorption of chemical species and facilitate their catalytic transformation, even at lower temperature. For example, it is well known that ice nanoparticles of polar stratospheric clouds (PSC's) play a key role in adsorption of pollutant molecules and their subsequent transformation into ozone depleting species, via chemical and photochemical processes.

In atmosphere, water forms molecular complexes with several atmospheric species like O_3, OCS, SO_2, SO_3, NO_2, NO, SH, ClO, NH_3, HNO_3, HCl, H_2SO_4, O_2, N_2, Ar, OH, HO_2, etc. in gas-phase via weak intermolecular interactions [15]. Thus, comprehending effect of water on photochemistry of various atmospheric trace gases is of relevance for earth's atmosphere and outer space environment. Though the concentration of these complexes in the atmosphere is miniscule they have a profound effect on the chemistry of the atmosphere. For example, photolysis of ozone-water complex ($O_3.H_2O$) leads to generation of OH radical in the atmosphere, at energies much lower than the bond dissociation limit of pure O_3. This red shift has been ascribed to enhancement in spin-forbidden dissociation of O_3 assisted by H_2O. Besides proximity of H_2O also minimizes collisional deactivation of O species produced upon photolysis of O_3. It is estimated that only 0.001% of ozone in the atmosphere might be complexed with water along the marine boundary layer, though they contribute to ~ 15% of OH produced in the atmosphere [15].

Such atmospheric processes have been mimicked at laboratory scale, by generating large water clusters (ice nanoparticles) doped with different chemical species and understanding their photochemical behaviour. Also, water clusters have been widely utilized for understanding different processes occurring in aqueous phase,

at aqueous-air interface and in gas-phase, for understanding nucleation and growth of aerosols. In studies, carried out on water clusters doped with acids (HCl, H_2CO_3, HNO_3, H_2SO_4) on surface, it was found that hydrolysis of these acids was suppressed at water-air interface, unlike in bulk phase where acid hydrolysis is a spontaneous process.

Using water clusters, studies have also been carried out to investigate photochemistry of halocarbon molecules and their clusters, deposited on ice nanoparticles. In one such study photodissociation of CFC-12 (CF_2Cl_2) clusters was investigated. Pure clusters of $(CF_2Cl_2)_n$ yielded predominantly Cl fragments at 193 nm. On the other hand, for CF_2Cl_2 molecules adsorbed on the water clusters no Cl fragments were observed, arising from photodissociation of CF_2Cl_2. This has been ascribed to surface orientation of CFC-12 on water surface via halogen bond or implantation of CF_2Cl_2 molecule within the cluster. Also, enhancement in dissociative electron attachment to CFC-12 in the gas phase by several orders of magnitude on ice surface has been reported for electrons with near-zero kinetic energy. This process has been considered as supplementary potential source of Cl radicals in the stratosphere [16]. Similarly photochemistry of $(CCl_4)_n$ clusters upon interaction with laser pulses of varying wavelength (spanning from IR to UV region) and intensity has also been carried out [17]. Photodecomposition of CCl_4 and its clusters is of relevance as it is a long-lived green-house gas having highest ozone depletion potential, among methyl halides. At all the laser wavelengths $(CCl_4)_n$ clusters undergoes excessive fragmentation. These neutral fragment ions are subsequently ionized by multiphoton absorption process (Figure 3). Depending on pulse duration at 266, $(CCl_4)_n$ clusters exhibit dominant ion signal corresponding to singly charged fragment ions i.e. Cl^+, CCl^+, CCl_2^+ and CCl_3^+ in the mass spectra. While for studies carried out at 266 nm using picosecond laser pulses minor ion signal corresponding to C_2Cl^+ and $C_2Cl_2^+$ were also
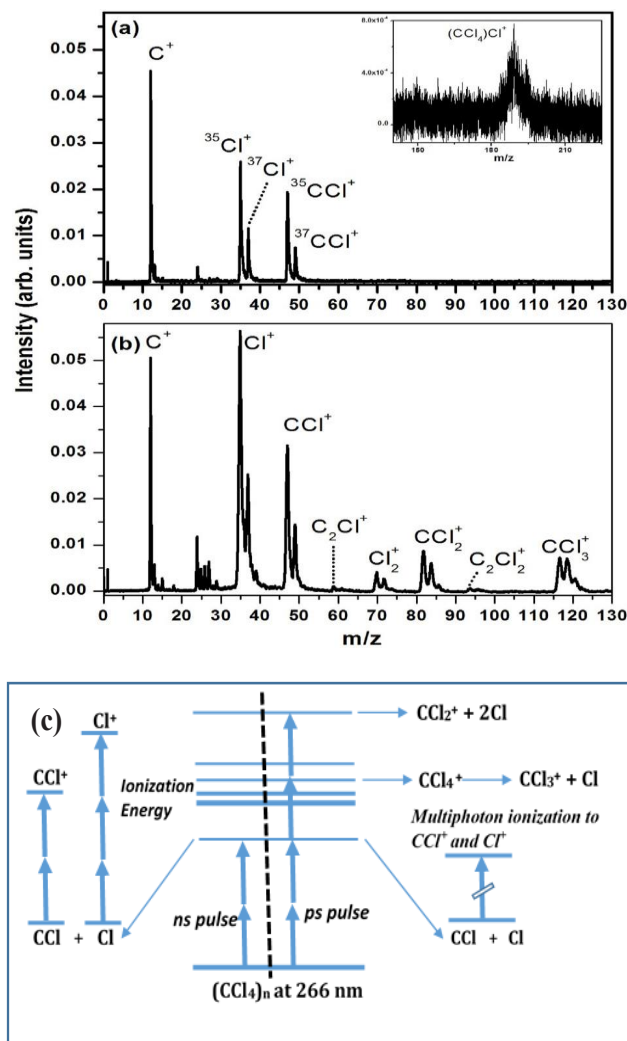

Figure 3: *Time-of-flight mass spectra of $(CCl_4)_n$ clusters upon interaction with 266 nm laser pulses of (a) 10 nanosecond pulse duration (Intensity ~ 10^9 W/cm^2) and (b) 35 picosecond pulse duration (Intesnity ~ 10^{11} W/cm^2).(c) Schematic of photodissocitaion/photoionization of $(CCl_4)_n$ clusters as a function of laser pulse duration [17].*

observed (Figure 3). Observation of these ions has been ascribed to intra-cluster radical chemistry resulting in generation of neutral precursors, which are subsequently multiphoton ionized. Present studies suggest that fate of atmospheric species also strongly depends on the characteristic of ionizing radiation.

Using clusters as a medium, origin, stability and lifetime of different organic molecules identified/detected in interstellar medium has also been investigated. One such compound

is pyruvic acid, which is proposed to have been synthesized on interstellar ices. It is an important molecule in prebiotic chemistry. To comprehend stability of pyruvic acid towards decomposition in the interstellar medium by slow electrons, electron attachment to homomolecular and hetero-molecular clusters of pyruvic acid has been investigated using mass spectrometry. Fragmentation pattern of pure and micro-hydrated pyruvic acid clusters was investigated as a function of electron energy. In these studies, degree of fragmentation has been found to decrease substantially upon clustering. Significantly lower fragmentation was observed for heteromolecular clusters of pyruvic acid and water, which was ascribed to non-dissociative attachment of electrons [18]. Thus, clusterization enhances stability of pyruvic acid. Above studies signify role of water clusters in mimicking and understanding different atmospheric and interstellar processes at laboratory scale.

2.4. Role of molecular clusters in understanding biological processes

Intermolecular interactions, primarily hydrogen bonds, play a crucial role in various biological and chemical processes. For example, complementary strands of DNA are held together by hydrogen bonds. Also, Hydrogen bonding plays a pivotal role in influencing ability of biomolecules to form and maintain particular three dimensional structures. Weakly bound intermolecular clusters are ideal candidates for understanding structure and stability of different biological molecule and for modelling various biological processes. As interaction of biomolecules with solvent is primarily responsible for their structure and activity, studies have been carried out on micro-hydrated biomolecular clusters, as around 70–80% by weight of the human body comprises water. As a primary constituent of body fluid, water plays a significant role in various biological processes taking place in a living organism. Hence, micro-hydrated clusters of biomolecules (or their simple molecular analogues) have been

investigated to understand influence of solvation on their structure, activity and radiation stability. In studies related to radiation therapy, these micro-hydrated biomolecular clusters have been subjected to low energy electrons and the resultant fragment ions have been analysed, for evaluating radiation stability of biomolecules and for identifying potential radiosensitizers. In radiation therapy, these low energy electrons are generated due to ionization of cellular components with high energy radiations. Based on these studies, it has been demonstrated that dissociative electrons attachment of biomolecules is suppressed to a significant extent upon hydration. Studies have also been carried out on nimorazole and their hydrated clusters, upon interaction with low energy electrons. In radiation therapy, nimorazole is used as radiosensitizer, as it mimics oxygen effect in hypoxic tumour cells. These cells are oxygen deficient due to their anaerobic environment. Based on the studies carried out on nimorazole clusters, it was concluded that upon hydration nimorazole efficiently forms parent radical anion via associative electrons attachment and the dissociative electron attachment channel is significantly suppressed [19]. Here the parent anion is stabilized via energy dissipation to the surrounding environment. Which is further substantiated by electron attachment experiments carried out on nimorazole doped water clusters of varying composition. As a result nimorazole is selectively cytotoxic to tumour cells, as nimorazole anions produced via associative electron attachment of low energy electrons is preferentially accumulation in the tumour cell.

Hydrated clusters of imidazole derivatives have also been investigated by spectroscopic techniques, to validate role of weakly polarized and unconventional H-bond donor i.e. C–H, in solvation and stabilization of H-bonded networks of water molecules. These weak hydrogen bonds involving C-H as a donor, influence structure and bioactivity of large number of biomolecules and natural products comprising activated C-H bonds. Similarly, equilibrium thermochemical measurements using ion mobility drift cell
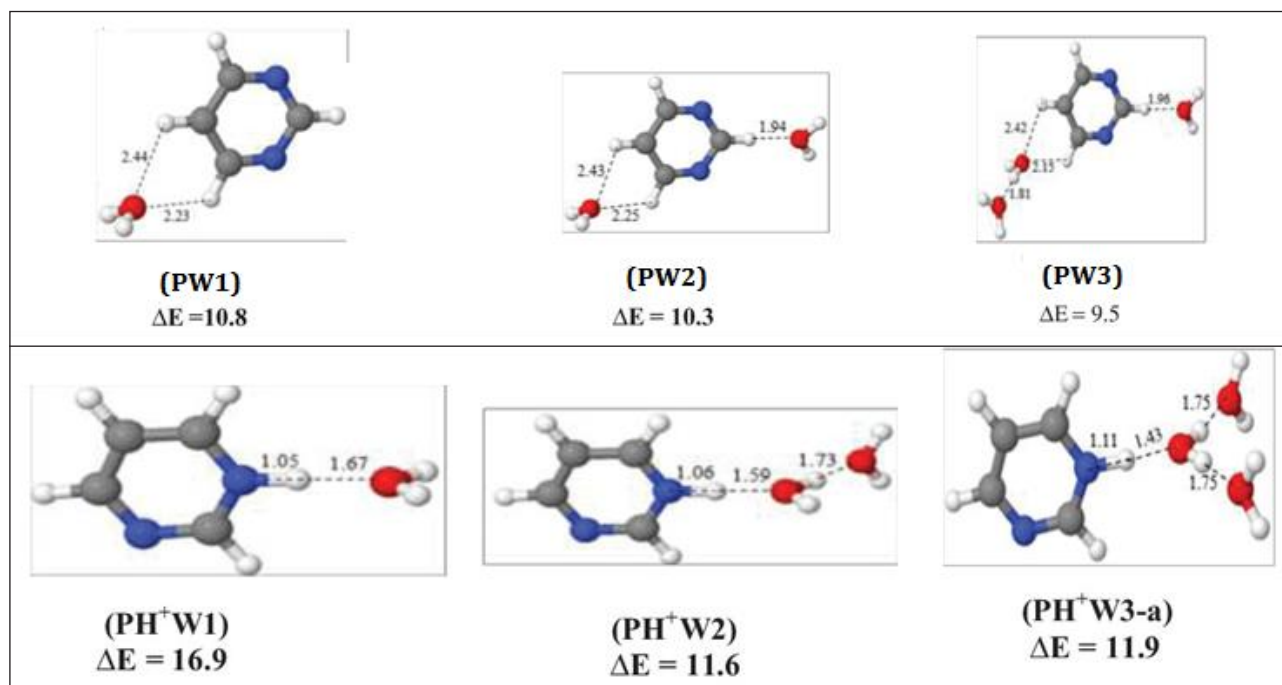
Figure 4: *Structures of (a) pyrimidine$^+$(H$_2$O)$_n$ (n=1-3) and (b) H$^+$pyrimidine(H$_2$O)$_m$ (m=1-3) clusters calculated by DFT at the M06-2x/6-311++G (d,p) level. ΔE represents binding energies, corrected for zero-point energies and basis-set super position errors [20].*

technique have also been carried out to quantify binding energies and associated entropy changes upon stepwise hydration of biologically significant ions. In one of our studies, binding energy of hydrated pyrimidine radical cation (11.0 kcal/mol) was found to be significantly lower than the binding energy of hydrated protonated pyrimidine cation (15.6 kcal/mol), which has been ascribed to formation of weak CH$^{\delta+}$··OH$_2$ hydrogen bond and stronger NH$^+$ ··OH$_2$ in the respective complexes. Moreover, hydrated pyrimidine radical cation clusters are suggested to form internally solvated structures, where the water molecules are bonded to the C$_4$N$_2$H$_4$$^{\bullet+}$ ion via weak CH$^{\delta+}$··OH$_2$ hydrogen bonds only. While the hydrated protonated pyrimidine clusters were suggested to form externally solvated structures, wherein the water molecules were also bonded to each other [20].

As simple molecular analogues of biomolecules are predominantly aromatic in nature, studies related to solvation of aromatic molecules, is also an important area of research in the field of cluster chemistry. Upon ionization, these solvated clusters predominantly generate protonated cluster fragment ions, arising from intracluster proton transfer processes, which transpires during dissociation/ionization of hydrogen bonded clusters. As proton transfer processes are of relevance to several biological processes, clusters provide a simple medium for understanding proton-transfer processes at molecular level. Mainly, several five and six membered aromatic compounds have been investigated using multiphoton ionization time-of-flight mass spectrometry. These aromatic compounds are key building blocks of proteins and nucleic acids i.e. pyrazine, pyrimidine, tetrahydrofuran, etc. [21]. Studies have also been carried out on clusters of tetrahydrofuran, which is considered as the simplest molecular analogue for the deoxyribose building block of DNA. These studies involve interaction of tetrahydrofuran (THF) clusters with intense laser pulses and electrons of varying kinetic energy. Figure 5 depicts time-of-flight mass spectrum obtained
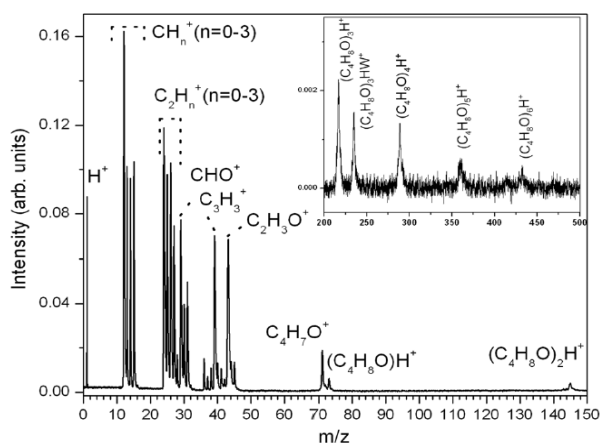
Figure 5: Time-of-flight mass spectrum of THF clusters irradiated with 355 nm laser pulse of intensity ~ 10^9 W/cm² [22].

upon interaction of tetrahydrofuran clusters with 355 nm laser pulses of intensity ~ 10^9 W/cm². In the mass spectrum, along with fragment ions, signal corresponding to protonated cluster ions of the type $(C_4H_8O)_nH^+$ (n = 2–6) and $(C_4H_8O)_3(H_2O)H^+$ are also observed in the mass spectrum. Though no ion signal corresponding to a water-associated THF cluster complex for monomer and dimer of THF were observed in the mass spectrum. Also, no $C_4H_8O^+$ molecular ion signal was observed in the mass spectrum [22]. In addition, electron solvation in THF clusters have been investigated using photoelectron imaging technique. Based on these studies, the vertical detachment energies of the solvated electron was found to increase from 1.96 to 2.71 eV, with increase in size of THF cluster size, suggesting stabilization of solvated electron in larger THF clusters. Such studies are of relevance in simulating radiation damage caused to the biomolecules upon interaction with ionizing radiations.

In summary, molecular clusters provide useful insight about various condensed phase phenomena, which are of relevance in basic and applied science. Fine alteration in cluster properties as a function of composition, shape and size, provides a convenient handle for mimicking bulk-phase environment in gas-phase. Besides, unique properties of cluster like finite size, bulk-like density in gas-phase, higher surface to volume ration, qualify clusters as ideal medium for simulating complex physical and chemical processes which transpire in bulk-phase, at molecular level.

Acknowledgement

References:

1. S. Das, P. M. Badani, P. Sharma and R. K. Vatsa. *Curr. Sci.*, 2011, **100**, 1008.
2. K. Müller-Dethlefs and P. Hobza. *Chem. Rev.*, 2000, **100**, 143.
3. M. Fárník, J. Fedor, J. Kočišek, J. Lengyel, E. Pluhařová, V. Poterya and A. Pysanenko. *Phys. Chem. Chem. Phys.*, 2021, **23**, 3195.
4. H. W. Kroto, J. R. Heath, S. C. O'Brien, R. F. Curl and R. E. Smalley. Nature, 1985, **318**, 162.
5. O. F. Hagena. *Z. Phys. D*, 1987, **4**, 291.
6. A. Bhattacherjee and S. Wategaonkar. *J. Phys. Chem. A*, 2017, **121**, 4283.
7. L. Li, X. Chang, X. Lin, Z.-J. Zhao and J. Gong. *Chem. Soc. Rev.*, 2020, **49**, 8156.
8. L. Liu and A. Corma. *Chem. Rev.*, 2018, **118**, 4981.
9. X.-N. Li, L.-N. Wang, L.-H. Mou and S.-G. He. *J. Phys. Chem. A*, 2019, **123**, 9257.
10. P. Sharma, I. Attah, P. Momoh and M. S. El-Shall. *Int. J. Mass Spectrom.*, 2011, **300**, 81.
11. D. C. McDonald II, B. C. Sweeny, A. A. Viggiano, S. G. Ard and N. S. Shuman. *J. Phys. Chem. A*, 2021, **125**, 9327.
12. M. Arakawa, K. Ando, S. Fujimoto, S. Mishra, G. Naresh Patwari and A. Terasaki. *Phys. Chem. Chem. Phys.*, 2018, **20**, 13974.
13. W. Lu and S. Yang. *J. Phys. Chem. A*, 2006, **110**, 13724.
14. P. Sharma, M. S, El-shall et al. (unpublished work) .
15. V. Vaida. *J. Chem. Phys.*, 2011, **135**, 020901.
16. V. Poterya, J. Kočišek, J. Lengyel, P. Svrčková, A. Pysanenko, D. Hollas, P. Slavíček and M. Fárník. *J. Phys. Chem. A*, 2014, **118**, 4740.
17. P. Sharma, S. Das and R. K. Vatsa. *Int. J. Mass Spectrom.*, 2020, **450**, 116291.
18. A. Pysanenko, K. Grygoryeva, J. Kočišek, R. Kumar T. P., J. Fedor, M. Ončák and M. Fárník. *Phys. Chem. Chem. Phys.*, 2021, **23**, 4317.
19. R. Meißner, J. Kočišek, L. Feketeová, J. Fedor, M. Fárník, P. Limão-Vieira, E. Illenberger and S. Denifl. *Nat. Commun.*, 2019, **10**, 2388.
20. A. M. Hamid, P. Sharma, M. S. El-Shall1, R. Hila, S. Elroby, S. G. Aziz and A. O. Alyoubi. J. Chem. Phys., 2013, **139**, 084304.
21. B. Zhang, Y. Cai, X. Mu, N. Lou and X. Wang. *J. Chem. Phys.*, 2002, **117**, 3701.
22. P. Sharma, S. Das and R. K. Vatsa. Rapid Commun. Mass Spectrom., 2015, **29**,45.

	Dr. Pramod Sharma joined Bhabha Atomic Research Centre in 2000. Since then he has been actively involved in the study of laser induced (single and multiphoton) gas-phase photochemical studies of organic, organometallic molecules and clusters, using time of flight mass spectrometry. He obtained his Ph.D. from University of Mumbai in 2008 under guidance of Dr. S. K. Kulshrestha. He did his post-doctoral work in Virginia Commonwealth University with Prof. M. Samy El- Shall. He is currently working on chemistry of molecular clusters, under influence of electric discharge and intense laser field.
	Dr. Soumitra Das passed M. Sc. from Jadavpur University in 2007 and joined Chemistry Division, BARC. Since then he has been involved in gas phase ionisation study of molecules and clusters. He obtained Ph.D. (Chemistry) in 2014 from Homi Bhabha National Institute under the guidance of Dr. R. K. Vatsa. He is currently involved in Coulomb explosion of different atomic and molecular clusters at low and moderate laser intensity conditions.

Quantum Chemical Modeling of Unprecedented Photothermal Effects Observed in Water-Filled Carbon Nanotubes

G. G. Kaarunya Dhevi,[1,2] and K. R. S. Chandrakumar*[2,3]

[1]*Food Technology Division, Bhabha Atomic Research Centre, Mumbai 400085, India*
[2]*Homi Bhabha National Institute, Mumbai, 400094, India*
[3]*Theoretical Chemistry Section, Bhabha Atomic Research Centre, Mumbai 400085, India*
* Email: krsc@barc.gov.in

Abstract

Carbon nanotubes can be ignited and reconstructed upon the exposure to light from a normal camera photo-flash. During this experiment, the temperature of the system is estimated to be more than 1500°C which causes unprecedented photothermal effects, leading to the generation of hydrogen molecules along with methane, CO_2, etc. In this work, we have made an attempt to model this phenomenon using electronic structure theory based methods by considering carbon nanocages and water molecules. Our results reveal that confining few water molecules only leads to the hydrogen bonded water cluster inside the nanocage. Increasing the number of water molecules results into opening of nanocage as well as destruction of carbon network structure. However, generation of hydrogen molecules is rather observed to be a difficult task which substantially relies on the concentration of water molecules present inside the nanocage.

1. Introduction:

Carbon nanotubes (CNTs) are tubular allotropes of carbon. Their structure consists of cylindrical walls of hexagonally arranged sp^2-hybridized carbon atoms akin to seamlessly rolled up cylinders of graphene sheets. Depending on the number of graphene layers (number of coaxial cylinders) in their structure, CNTs can be categorized into single-walled and multi-walled carbon nanotubes (SWCNTs and MWCNTs, respectively). Historically, MWCNTs were discovered in 1991 when Ijima reported the presence of nanotubes of pure carbon, then called "helical carbon microtubules", in the soot of arc-discharge fullerene reactor [1]. Characterization of these tubes using high resolution transmission electron microscopy (HRTEM) and electron diffraction revealed that they consist of at least two (often more) layers, measuring ~ 3-30 nm in outer diameter and ~ 1-100 μm in length. Later, Ijima reported the discovery of SWCNTs which were narrower (~1 nm in diameter) and made up of a single graphene layer [2]. Both SWCNTs and MWCNTs are high aspect ratio structures with length-to-diameter ratio usually above 1000. Thus, they can be considered as quasi one-dimensional nanomaterials. The bonding, structure and dimensionality of CNTs endow them with unique and superlative mechanical, thermal and electrical properties such as high tensile strength, superior thermal, and electrical conductivity.

In the year 2002, a surprising phenomenon of CNTs came into the light. It was discovered that SWCNTs can be ignited and they undergo reconstruction on exposure to a short pulse of visible electromagnetic radiation from a camera flash [3]. This process, termed as "flash-ignition" or "photo-ignition", has been explained in terms of photo-thermal effect where the absorbed photon energy is converted into heat through non-radiative dissipation or photochemical reactions which eventually disrupts carbon network structure. In general, this heat energy would be gradually lost to bulk and equilibrated. However, in the case of SWCNTs, the rigid carbon network and high axial thermal conductivity

cause the heat to be confined within individual nanostructures leading to the formation of local hot spots with high temperatures which is sufficient to initiate the oxidation of carbon (ignition). This reaction is further propagated by heat released from the ignition exothermic step. In 2006, Guo and co-workers investigated the possibility of harnessing the highly efficient photo-thermal effect in SWCNTs for the synthesis of methane [4]. SWCNTs were exposed to conventional camera flash and the released gases were analyzed using quadrupole mass spectrometer (QMS). Peaks obtained at atomic mass units of 15 and 16 corresponding to CH_3^+ and CH_4^+, respectively, clearly indicated the formation of methane. Adsorbed atmospheric hydrogen or atomized hydrogen from residual wetting water were designated as a possible H sources.

Later, Guo and co-workers raised an important question: What would happen if SWCNTS filled with water molecules, were subjected to photo-flash experiments? [5] Interestingly, the evolution of hydrogen rich gases was observed indicating that water-splitting is occurring with visible light sources. The total pressure of the glass chamber housing the system sharply increased to 12 Pa within ~ 1s of irradiation and stabilized around 0.01 - 0.1 Pa within minutes. As the reaction was carried out in ultra high vacuum ($< 10^{-7}$ Pa), the increase in pressure was solely due to gases generated during the reaction. Analysis of the released gases using ion gauge and QMS indicated that hydrogen accounted for ~ 80 mol % of the gases. Carbon oxides, methane, and trace amounts of ethane accounted for the remaining 20 mol %. SWCNTs act as carriers of nanowater as well as photo catalyst and the energy absorbed from the flash is effectively thermalized inside the nanostructure. It was postulated that local increase in temperature leads to the release of free C atoms creating a high pressure environment within the nanotubes. This causes the water molecules and other species present inside the nanotubes to be momentarily confined in the spatial nano-regime.

The combination of high temperature and high pressure under high confinement possibly lead to the reaction conditions favoring the splitting of water molecules. Hydrogen generation is an important problem in the forefront of green energy research. Therefore, it is of interest to understand the visible light flash induced generation of hydrogen from SWCNT-confined water reported in this paper.

The above-mentioned photo-flash based experiments are in general very fast and taking place within micro to milli seconds. It is therefore not feasible to experimentally explore the details of the chemical processes in such short period of time. In present work, we have made an attempt to investigate the possible chemical reactions taking place in water containing SWCNTs following a photo-flash using density functional theory approaches. We are specifically interested in the events following the creation of high-pressure local environment rather the actual photo-thermal transfer and liberation of C, H and O atoms. To this end, appropriate model systems have been considered as discussed shortly. An attempt has been made to find out the effect of confinement and the triggering factor leading to the formation of H_2.

2. Computational details:

All minimum energy structures have been obtained through calculations performed at the level of density functional theory employing the B3LYP exchange–correlation hybrid functional method as implemented in TURBOMOLE as well as ORCA 3.0 quantum chemical software [6,7]. The geometry optimizations have been performed using Ahlrich's def2-SVP basis sets to describe the C, H and O atoms. Final geometries have been optimized using def2-TZVP basis sets. All calculations have been performed without the imposition of symmetry constraints.

3. Results and Discussion:

Taking into account the experimental conditions as described in literature [3-5], the reactions inside water containing SWCNTs can

be thought to proceed in the following manner. Following photo-flash, liberation of C atoms from the nanostructure occurs due to local heat confinement and disruption of carbon network structure. The duration of this photo-thermal process and build-up as well as the recession of the photoacoustic wave is quite short. Transiently, the water molecules can be assumed to be highly confined inside the nanotube along with other species in close proximity and they do not have sufficient time to move away. As temperatures within the tubes at this point is also high, enormous pressures build up and water molecules can be thought to be under confinement inside a cage of atomic carbon species. Experimentally too, it is observed that there is a sharp increase in total pressure in glass chamber housing SWCNTs within of seconds of ignition [4]. This increase in total pressure could be indicative of an even higher increase in pressure inside the CNTs. In order to mimic the experimental conditions as described above, we have considered a model system consisting of fullerene molecules filled with water molecules inside the cages. The spherical periodic arrangement of carbon atoms in the fullerenes sufficiently replicate the nature of the high confinement as well as the transient atomic arrangement of liberated carbon atoms around water molecules following the flash. We have chosen C_{36} fullerene, which has an average diameter of ~ 5.7 Å to model the splitting of water inside SWCNT.

Let us begin with the discussion of pristine C_{36}. The minimum energy structure obtained for pristine C_{36} is given in Fig. 1. This structure can be described as an ellipsoid of fused pentagonal rings of carbon atoms with average C-C bond distance of ~ 1.43 Å. Equatorial diameter (D_{eq}) of this ellipsoid was ~ 5.9 Å and the polar diameter (D_{pol}) was ~ 5.2 Å. The results of systematic addition of water molecules into the pristine C_{36} cavity are presented as follows. On addition of one water molecule, no significant changes were observed in the shape, size and C-C bond lengths of the fullerene. The confined water molecule resided approximately at the

center of the cavity. Its geometrical parameters (O-H bond length = 0.95 Å; H-O-H bond angle = 104.3°) were comparable to that of free gas-phase water. When a second water molecule was added, the fullerene's dimensions was observed to increase (D_{eq} ~ 6.2 Å; D_{pol} ~ 5.5 Å; average C-C bond distance ~ 1.49 Å). Ionization of water into free hydronium and cage adsorbed hydroxyl ions (C---OH^- =1.48 Å) were also observed. These ions interacted with each other through inter-molecular hydrogen bonding having a length of 1.38 Å and bond angle of ~ 105°. These parameters deviate significantly from that of conventional O---H-O hydrogen bond which is addressed in a subsequent paragraph. Energy minimizations following the accommodation of three and four water molecules also resulted in water ionization and bulging of C_{36}. It must be mentioned here that the integrity of the fullerene cage remained intact in all the above cases and the interaction of confined water molecules with C_{36} is mostly observed through the adsorption of either water molecules or hydroxyl ions as depicted in the top 4 boxes of Fig. 1. The C---O bond distance in these adsorption events were in the range of 1.42-1.48 Å.

Addition of more than four water molecules triggered the bursting of the fullerene cage. We have investigated this phenomenon for confinement of five to ten water molecules. One trend common to these systems is that C-O, C=O or C-O-C type groups could be found at the carbon atoms lining the site of rupture. For example, two C-O-H and one C-O-C groups of average C-O bond lengths 1.36 and 1.46 Å, respectively existed at the rupture site of C_{36} + $5H_2O$ and equilibrium geometry of C_{36} + $6H_2O$ system contained two C=O groups of average bond length ~ 1.18 Å. These groups can be considered as oxidation products of the cage. This is even more true for the case of C_{36} + $8H_2O$ system where liberation of free carbon monoxide (bond length = 1.15 Å) was observed. Thus, it can be concluded that confinement of 4-5 water molecules initiates the ignition or oxidation of C_{36}. When ten water molecules were added to this cavity, the
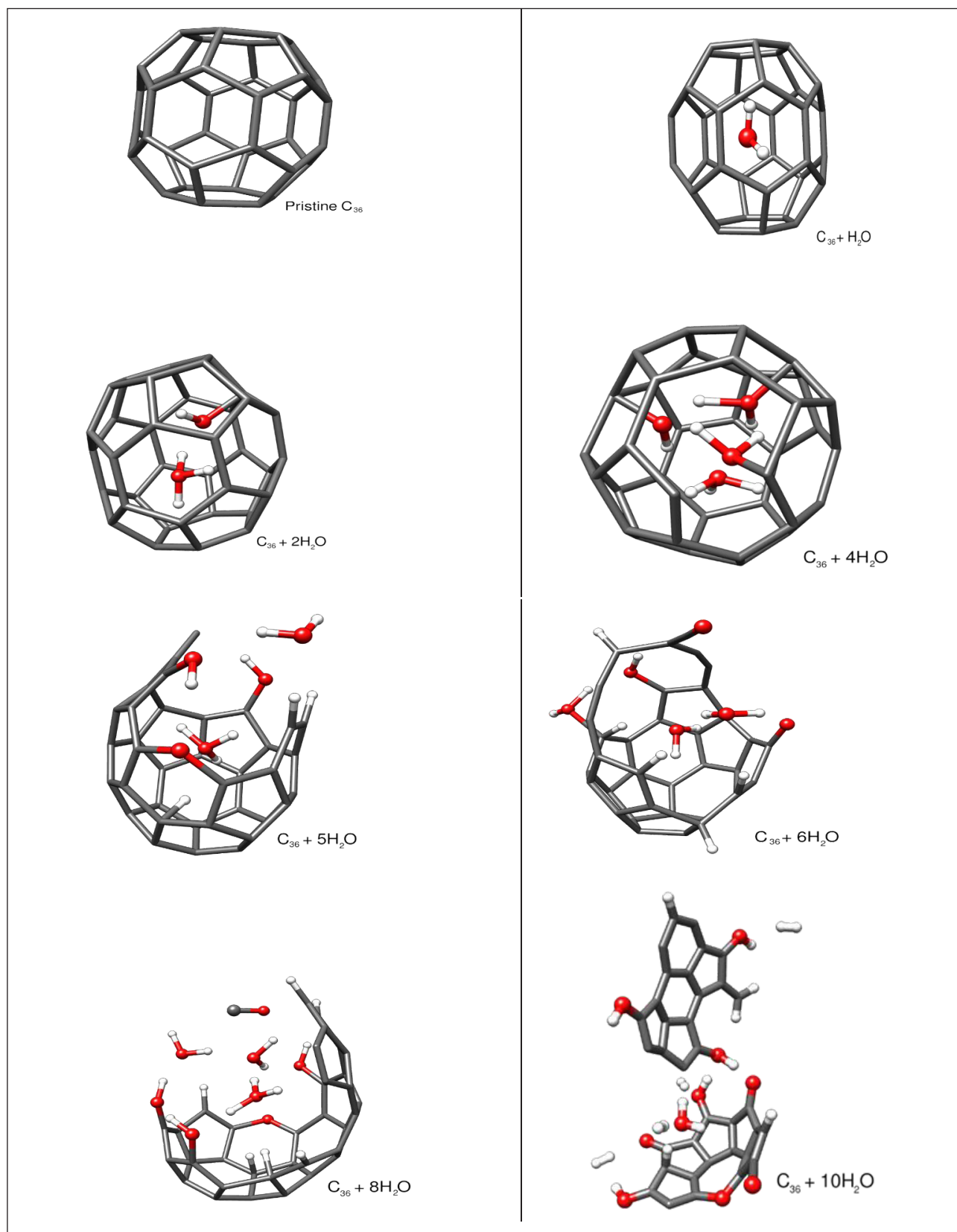
Figure 1: Minimum energy structures for confinement of water molecules inside C$_{36}$ fullerene cage

bursting of cage occurred in a manner resulting in fragmentation of C_{36} into two 18-carbon cup shaped halves. The carbon atoms bordering these fragments feature several C-OH and C=O groups in concurrence previous observations. Interestingly, in addition to ionization of water and cage oxidation reactions, formation of four hydrogen molecules could be observed indicating that splitting of water occurred. These results reveal that when a minimum number of 8-10 water molecules are confined within a carbon cavity of ~ 6 Å length, it is possible to generate molecular hydrogen through the water splitting process. Thus, our models based on the water molecules confined inside the fullerene cage, unambiguously predict the necessary condition for the liberation of H_2.

Let us now analyze certain aspects of the results obtained above. HRTEM images taken after flash-ignition of SWCNTs in air indicate the presence of reconstructed structures such as nano-horns [3]. At the same time, TEM as well as electron microscopy images of SWCNTs flashed at vacuum reveal that structural reconstruction occurs even in the absence of ignition [3,4]. CNTs oxidize at about 600 – 700°C, but bond-breakage and reconstruction require higher temperatures of 1500 – 2000 °C [8,9]. Therefore, the photo-thermal effect following flash must allow the local temperature within individual nanotubes to reach at least 1500 °C. The same criteria can be extended to water containing SWCNTs. Thermal degradation of water is an uphill process with a positive change in Gibbs free energy (ΔG ~ +237 kJ/mol) and requires temperatures greater than 2000 °C. Thus, the increasing order of feasibility of processes appears to be cage oxidation followed by cage rupturing and hydrogen generation. The results of our energy minimization studies on the model chosen to mimic the transient high pressure experimental conditions indicate that number of confined molecules is the key factor triggering these processes. Whereas oxidation of the cage is initiated upon the addition of 4-5 water molecules, fragmentation of C_{36} as well as formation of hydrogen occur when at least 8-10

water molecules are present.

4. Conclusions:

According to experimental data, ~ 80 mol% of the gases released during photo-flash of water filled SWCNTs was made of hydrogen. The second major contributor was carbon monoxide (~ 11 mol %) [5]. Using our model, we are able to observe the liberation of both four H_2 (in > 8 water molecule containing systems where water–splitting has been triggered) and one CO (in 4-8 water molecule containing systems where only cage oxidation occurs). The ratio of the number of H_2 to CO molecules also agrees well with the QMS data of composition of released gases. Thus it can be concluded that using a fullerene model to mimic the distribution of atomic carbon around SWCNT-confined water, many of the experimental results could be revisited in our computational investigation. Light has been shed on certain aspects of the chemistry of this reaction such as the effect of number of confined water molecules and functional groups involved in the oxidation of the cage. It must be mentioned here that structural parameters of confined water differed considerably from gas-phase water in most of the cases. It could also be observed that bond length and angles of hydrogen bond between hydronium and hydroxyl ions differed considerably from that of bulk water. Such deviations in the structure of water molecules confined inside carbon systems such graphite and CNTs have been previously reported in both experimental and theoretical studies [9-12]. Nanoconfined water has unusual structure and dynamics, different from that of the bulk water. SWCNTs undergo highly efficient photothermal effect under the photo flash. This is perhaps the reason for the occurrence of high barrier reaction such as splitting of water with low-energy input such as photographic flash inside SWCNTs.

References :

1. Iijima, S. Nature, **1991**, 354, 56–58.
2. Iijima, S. and Ichihashi, T. Nature,**1993**, 363, 603–605.
3. Ajayan, P.M., Terrones, M., De la Guardia, A., Huc, V., Grobert, N., Wei, B.Q., Lezec, H., Ramanath, G. and

Ebbesen, T.W., *Science,* **2002**, 296, 705.

4. Guo, D.Z., Xue, Z.Q., Chen, Q., Zhang, G.M., Zhang, Z.X. and Gu, Z.N., Journal of the American Chemical Society, **2006,** 128, 15102-15103.

5. Guo, D.Z., Zhang, G.M., Zhang, Z.X., Xue, Z.Q. and Gu, Z.N., *The Journal of Physical Chemistry B*, **2006**. *110*,1571-1575.

6. R. Ahlrichs, M. Ba¨r, M. Ha¨ser, H. Horn and C. Ko¨lmel, Chem. Phys. Lett., **1989**, 162, 165–169.

7. Nesse, F. The ORCA program system. WIREs Comput. Mol. Sci. **2012**, 2, 73−78.

8.   Tsang, S. C. et al., Nature, **1993**, 362, 520.

9.   Nikolaev, P. *et al., Chem. Phys.Lett., **1997,*** 266, 422 .

10. Feller, D., and Jordan, K. D. The Journal of Physical Chemistry A, 2000, 104, 9971-9975

11. Byl, O., Liu, J.C.,Wang, Y., Yim, W. Y., Johnson, K. J., and Yates, J. T. Jr. Journal of the American Chemical Society, **2006**, 128, 12090-12097.

12. Tripathy, M.K. and Chandrakumar, K. R. S. Phys.Chem. Chem.Phys., **2017**, 19, 19869.

## Acknowledgement

	Dr. Chandrakumar *has been working as a Scientific Officer since 2004 at Bhabha Atomic Research Centre, Mumbai, after completing his Ph.D. from National Chemical Laboratory, Pune. His research interests are in the areas of nanostructured materials, growth mechanism of carbon nanotubes & fullerenes, self-assembly process, and nanocatalysis for environmental applications, etc.* *His noteworthy contributions include the conceptual density functional theory based chemical reactivity descriptors, development of hydrogen storage materials and growth mechanism of carbon based nanostructured materials. He is also interested in science popularization and basic education programs.* *He is a recipient of the young scientist award from Indian Science Congress Association (2002), Indian National Science Academy (2005) and the Department of Atomic Energy (2007). He has also recently been awarded the Scientific & Technical Excellence Award (2015) from Department of Atomic Energy.*
	Ms. Kaarunya Dhevi *is working as Scientific Officer in Food Technology Division of Bhabha Atomic Research Center. She graduated from UM-DAE Center for Excellence in Basic Science in 2017 obtaining an Integrated Masters degree in Chemistry. She is working on the development of novel radiochromic dosimeters and their interactions with gamma radiation using radiation transport codes. She is currently doing her Ph. D. at Homi Bhabha National Institute and her thesis work focuses on the investigation of electronic structure and catalytic properties of enzyme models based nano-biohybrid functional materials using the recently developed QM/MM based quantum chemical methods.*
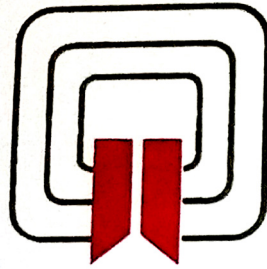
INDIAN SOCIETY FOR RADIATION AND PHOTOCHEMICAL SCIENCES

(Reg. No. 617/1985, GBBSD, Bombay; Trust No. F-10965)

Radiation & Photochemistry Division

Bhabha Atomic Research Centre, Mumbai - 400 085

Member Enrolment Form

1. Name in Block Letters:

2. Date of Birth:

3. Highest Academic Qualification:

4. Present Position:

5. Addresses:

Office	Residence
Telephone	Telephone
E-mail	E-mail

6. Address for Correspondence: Office / Residence

7. Category of Membership Applied for: Annual / Life /Corporate member

8. Remittance: DD in favour of 'ISRAPS' payable at MUMBAI
   For Bank Transfer:
   A/c No.10536133801, SBI, BARC Branch, IFSC SBIN0001268
   (e-mail the money transfer details along with the details requested above to
   israps.secretary@gmail.com and CC to jyotim@barc.gov.in)

Category	Fees	Admission fee	Total Amount
Annual	Rs 200/-	Rs 100/-	Rs 300/-
Life Member	Rs 1500/-	Rs 100/-	Rs 1600/-
Corporate Member	Rs 20000/-	Rs 1000/-	Rs 21000/-

9. Brief Resume of activities and research interests:

10. List of memberships of other professional bodies, if any:

11. List of prizes/awards/fellowships received, if any:

12. Number of Publications:

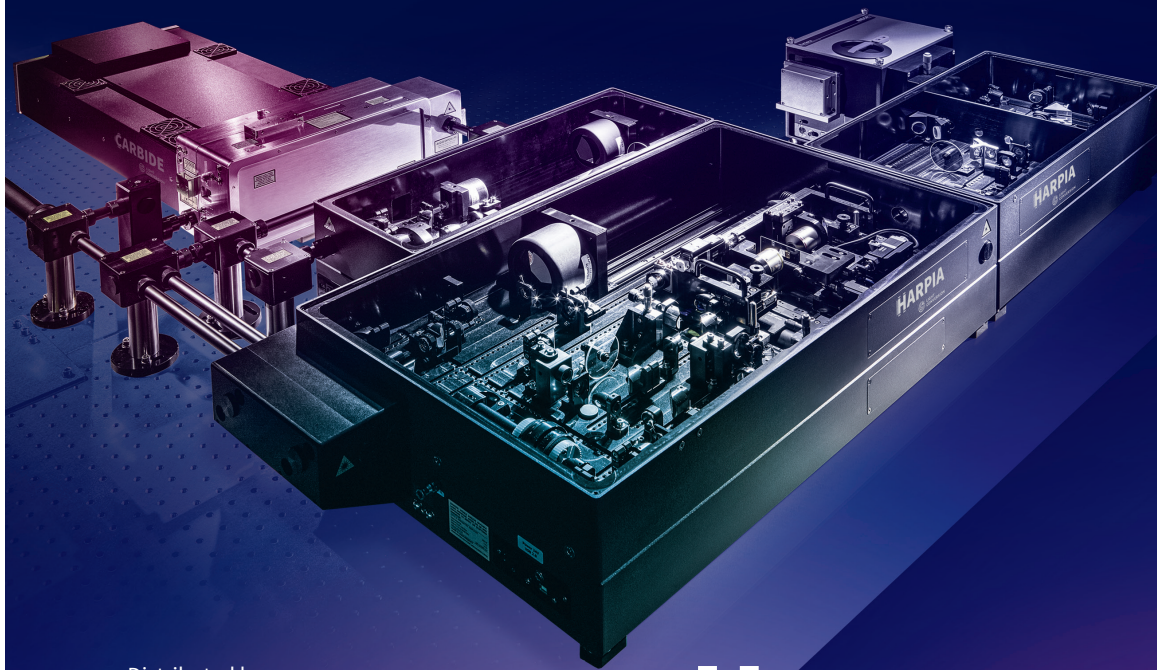I agree to abide by the constitution and bye-laws, and rules and regulations of the SOCIETY.

Place: Signature

Date:

ATOS   ATOSCOPE

HYPERSPECTRAL IMAGING DETECTORS CCD TUNABLE LASERS
SCMOS INFRARED UV MULTISPECTRAL COOLED
NITROGEN LITTROW CRYOSTATS ASTRONOMY
HELIUM LITTMAN/METCALF SOLAR CELL CONFOCAL
INSTRUMENTATION ANALYTICS
GAS UNCOOLED ICCD LIQUEFIERS
SCIENTIFIC PICO CRYOGENICS
QUANTUM XRAY VIS THERMICS
PULSED TERAHERTZ NDT DIODE
COMPRESSORS MICROFLUIDICS

Sona sCMOS
Large Format – 95% Quantum
Efficiency – Cooled to -45^{0}C

Kymera Multimodal Spectroscopy
Platform - Adaptive Focus – True Res
– Quad Grating Turret - µManager

Tunable Diode Lasers – Littrow & Littman
External & Vertical Cavity Surface Emitting
Tera Hertz & Quantum Cascade Lasers

Cooled & Uncooled IR cameras
Portable and fixed cameras

Solar cell QE measurement, photobiological
safety, light/display characterisation &
spectroradiometers

Hyperspectral Imaging cameras for field, lab
and airborne applications

Flow Cryostats for 3K and 77K
measurements with ultra-low
vibration system. Cryogen free
cryostats for 4K measurements.

Compact MRI and NMR
systems, 1m X 1m
Footprint, Preclinical and
clinical imaging.

ATOS Instruments Marketing Services   **ATOSCOPE Instruments Pvt. Ltd.**

www.atosindia.com   atos@atosindia.com